RICE UNIVERSITY

Molecularly-Targeted Gold-Based Nanoparticles for Cancer Imaging and Near-Infrared Photothermal Therapy

By

Emily Shannon Day

A THESIS SUBMITTED
IN PARTIAL FULFILLMENT OF THE
REQUIREMENTS FOR THE DEGREE

Doctor of Philosophy

APPROVED, THESIS COMMITTEE:

Jennifer West, Isabel C. Cameron
Professor, Chair, Bioengineering
Chair of Thesis Committee

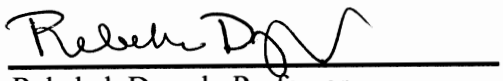

Rebekah Drezek, Professor,
Bioengineering

Jason Hafner, Associate Professor,
Physics & Astronomy

HOUSTON, TEXAS
MAY 2011

ABSTRACT

Molecularly-Targeted Gold-Based Nanoparticles for Cancer Imaging and Near-Infrared Photothermal Therapy

by

Emily Shannon Day

This thesis advances the use of nanoparticles as multifunctional agents for molecularly-targeted cancer imaging and photothermal therapy. Cancer mortality has remained relatively unchanged for several decades, indicating a significant need for improvements in care. Researchers are evaluating strategies incorporating nanoparticles as exogenous energy absorbers to deliver heat capable of inducing cell death selectively to tumors, sparing normal tissue. Molecular targeting of nanoparticles is predicted to improve photothermal therapy by enhancing tumor retention. This hypothesis is evaluated with two types of nanoparticles.

The nanoparticles utilized, silica-gold nanoshells and gold-gold sulfide nanoparticles, can convert light energy into heat to damage cancerous cells. For *in vivo* applications nanoparticles are usually coated with poly(ethylene glycol) (PEG) to increase blood circulation time. Here, heterobifunctional PEG links nanoparticles to targeting agents (antibodies and growth factors) to provide cell-specific binding. This approach is evaluated through a series of experiments.

In vitro, antibody-coated nanoparticles can bind breast carcinoma cells expressing the targeted receptor and act as contrast agents for multiphoton microscopy prior to inducing cell death via photoablation. Furthermore, antibody-coated nanoparticles can

bind tissue *ex vivo* at levels corresponding to receptor expression, suggesting they should bind their target even in the complex biological milieu. This is evaluated by comparing the accumulation of antibody-coated and PEG-coated nanoparticles in subcutaneous glioma tumors in mice. Contrary to expectations, antibody targeting did not yield more nanoparticles within tumors. Nevertheless, these studies established the sensitivity of glioma to photothermal therapy; mice treated with PEG-coated nanoshells experienced 57% complete tumor regression versus no regression in control mice. Subsequent experiments employed intracranial tumors to better mimic the clinical setting. These tumors are highly vascularized, so nanoparticles were addressed toward receptors abundantly expressed on tumor vessels using growth factors as a novel targeting strategy. Photothermal therapy with these vascular-targeted nanoparticles disrupted tumor vessels, leading to a 2.2-fold prolongation of median survival versus control mice.

This work confirms that nanoparticle surface coating can affect biodistribution and therapeutic efficacy. With continued optimization of molecular targeting strategies, imaging and photothermal therapy mediated by nanoshells and gold-gold sulfide nanoparticles may offer an effective alternative to conventional cancer management.

Dedication

To my parents, for always encouraging me.

Acknowledgements

To begin, thank you to Dr. West for providing an environment that has allowed me to develop as a scientist from a naïve undergraduate summer student to a knowledgeable researcher today. Your guidance and support are tremendously appreciated! Thank you as well to Dr. Drezek and Dr. Hafner for serving on my committee and for several helpful discussions over the years.

Thank you to the members of "Team Nano" who have taught me many things and shared much laughter with me throughout this journey: André Gobin, Amanda Lowery, Jennifer Garner, Andrew Coughlin, Laura Strong, Neha Kamat, Philip Wingert, Nicholas Riggall, Nicholas Chedid, Laura Tanenbaum, and Blake Stiles.

I am extremely grateful to the physicians and scientists at Texas Children's Hospital who collaborated with me on these projects: Linna Zhang, Susan Blaney, Patrick Thompson, M. Waleed Gaber, Janice Zawaski, Caterina Kaffes, Nabil Ahmed, and Xiao-Nan Li.

Thank you as well to the following people for training me to use various instruments, for providing me with technical support, and for sharing wisdom with me: John Slater, Lissett Bickford, Nastassja Lewinski, Jesse Farrell, Ramsey Kamar, Mark Pierce, April Smith, Jerome Saltarrelli, Germaine Agollah, Glenn Goodrich, William James, Anil Sood, and Ying Hu.

Thank you to all the members of the West Lab, past and present, for making graduate school such an enjoyable experience. Special thanks to Marcella Estrella for your hard work because the lab could not function without you! Thanks to Melissa McHale for critical reading of many manuscripts.

Finally, I would like to acknowledge financial support from the National Science Foundation Graduate Research Fellowship, the Howard Hughes Medical Institute Med Into Grad Program, the Alpha Lambda Delta Dorothy Anderson Graduate Fellowship, and the Rice University President's Graduate Fellowship.

TABLE OF CONTENTS

LIST OF FIGURES

LIST OF TABLES

Chapter 1: Introduction

Despite tremendous gains in our knowledge of fundamental cancer biology over the past several decades, similar improvements in clinical practice and patient survival have not been achieved. Current front-line approaches to cancer therapy have been in use for more than 70 years: chemotherapy was introduced by Goodman and colleagues in the 1940s to treat patients with lymphoma (Goodman *et al.* 1946); radiation therapy was used successfully in oncology as early as the 1890s (Kogelnik 1997); and, surgical resection of tumors can be traced to the writings of ancient Greeks and Egyptians (Pollock 2008). Although these medical techniques have been evolving and improving throughout history, there remains a significant need for advances in diagnosis and treatment. This need is evidenced by the fact that the lifetime risk of developing cancer for Americans born today is ~41% and, maintaining current standards of care, one in four Americans is expected to die from cancer (National Cancer Institute 2010). Furthermore, cancer is not confined to the United States; rather, it is a global disease with projected worldwide incidence of 15.5 million cases in 2020 (Mathers and Loncar 2006). Therefore, new tools must be developed in order to reduce the burden of cancer.

Working toward this goal of improved patient outcome, researchers have begun to develop nanoparticle-based platforms for detection and treatment of cancer. This thesis validates one form of therapy that incorporates nanoparticles as exogenous energy absorbers to provide high-resolution imaging of cancerous cells and to selectively deliver heat capable of inducing cell death to tumors. This technique offers several advantages over conventional therapeutic approaches, to be detailed later. In this chapter cancer biology and the challenges associated with diagnosis and treatment will be briefly

described, recent developments in nanotechnology for cancer management will be discussed, and previous progress in the literature that provided a foundation for this research using nanoparticles for thermal cancer therapy will be reviewed.

1.1 A Brief Introduction to Cancer Biology and Clinical Management

Cancer remains a clinical challenge today. To develop better tools for imaging and therapy, it is critical to understand the nature of the disease. Here, the hallmarks of cancer will be highlighted and current approaches to diagnosis and treatment will be discussed.

1.1.1 Cancer Biology

Tumorigenesis begins when a single cell acquires defects in the regulatory circuits that maintain homeostasis; this loss of balance between pro- and anti-growth signals confers growth advantages that lead to uncontrolled cell proliferation, resulting in formation of a tumor mass (Hanahan and Weinberg 2000). The process by which normal cells become malignant is marked by the accumulation of genetic alterations that induce either a gain-of-function in proto-oncogenes that regulate cell growth and division or a loss-of-function in tumor suppressor genes that ordinarily inhibit cell proliferation. Hanahan and Weinberg suggested that six alterations in cell physiology are characteristic of malignant cell behavior: self-sufficiency in growth signals, insensitivity to growth-inhibitory signals, evasion of apoptosis, limitless replicative potential, sustained angiogenesis, and the ability to invade tissue and metastasize (Hanahan and Weinberg 2000). More recently, Colotta *et al.* proposed that cancer-related inflammation is a seventh "hallmark of cancer" since inflammatory molecules can lead to genetic instability (Colotta *et al.* 2009). **Figure 1.1** depicts the seven hallmarks that contribute to cancer progression.

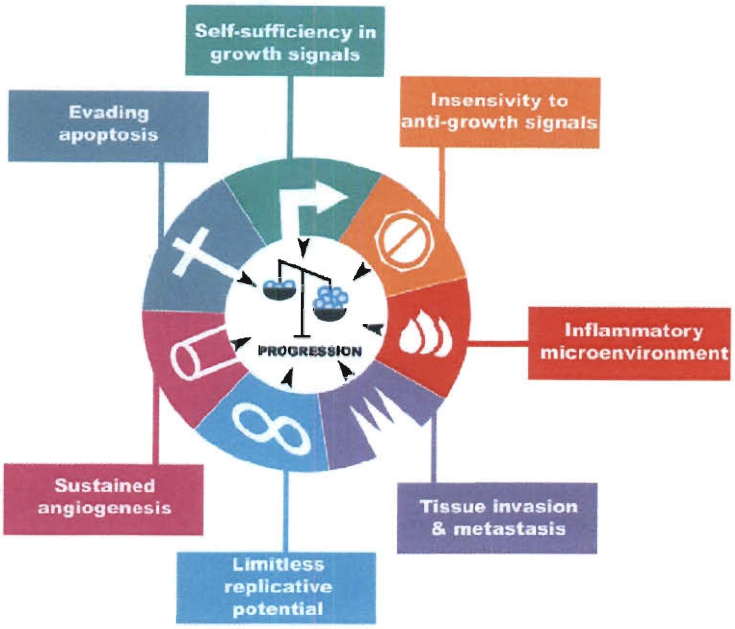

Figure 1.1: The hallmarks of cancer. The seven acquired capabilities of cancer cells that lead to tumor progression. Image from Colotta *et al.* 2009.

Because cancer cells require nutrients and oxygen to support continued growth of a tumor, vascularization is necessary for tumor growth beyond a diameter of 1-2 mm (Folkman 1971). To recruit development of new blood vessels, tumor cells excrete pro-angiogenic factors such as VEGF (vascular endothelial growth factor), which encourage migration and survival of endothelial cells, and MMPs (matrix metalloproteinases) that degrade components of the extracellular matrix (Rundhaug 2003). Due to the imbalance of pro- and anti-angiogenic factors, vascular networks in and around tumors form rapidly and are characterized by architectural defects such as increased vessel diameter, tortuosity, endothelial fenestrations, and excessive branching (Carmeliet and Jain 2000). In addition, tumor vessels lack functional pericytes (Benjamin *et al.* 1999) and exhibit inter-endothelial cell openings as large as 2 μm (Hashizume *et al.* 2000), resulting in vascular "leakiness." **Figure 1.2** emphasizes the architectural differences between

normal blood vessels and those found in and around tumors (Jain 2005). Later it will be discussed how these vascular differences between tumor and normal tissue are critical to successful use of nanoparticles in cancer management.

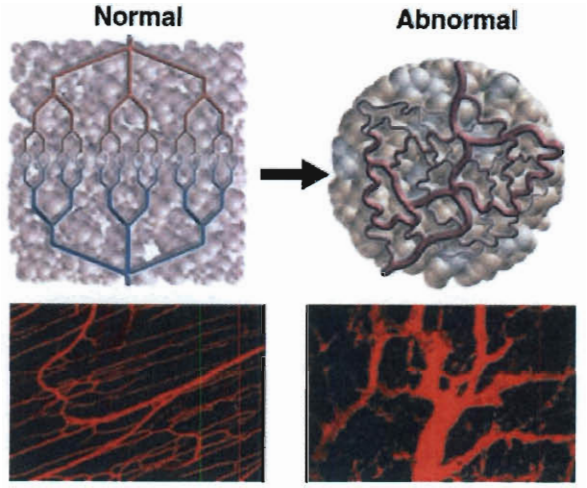

Figure 1.2: Comparison of vessel architecture in normal and tumor tissue. Top row: Schematic representation of vessel structure showing that normal tissue vasculature is ordered and hierarchical while abnormal tumor vasculature is disorderly. Bottom row: Two-photon microscopy images of blood vessels in skeletal muscle (left) and colon carcinoma (right) showing that tumor vessels have increased diameter and chaotic architecture compared to normal vessels. Adapted from Jain 2005.

Angiogenesis is an important factor not only for continued tumor growth but also for development of metastasis, the appearance of secondary tumors at sites distant from the original lesion (Fidler 1990). Most cancer-related deaths are caused by metastases that are resistant to conventional therapy. Treatment of metastases is increasingly complex because, as Fidler explained, when a tumor cell becomes metastatic it acquires several capabilities that allow it to escape its original site, survive circulation, and then flourish in a new environment (Fidler 1990). Not every cell that escapes the primary tumor will develop a secondary tumor, and research has shown that tumors metastasize preferentially to certain organs. Stephen Paget hypothesized in 1889 that this was because metastatic tumor cells have an affinity for the biological milieu of certain organs

(Paget 1889). This concept, known as the "seed and soil" hypothesis, suggests that metastases can form only when the tumor cell (the seed) and the organ microenvironment (the soil) are compatible. For this reason, successful elimination of metastases will require therapy targeted towards both cancerous cells and the factors present in tissue that enable their survival (Fidler 2003). In the next two sections, tools currently used to image and treat cancer will be discussed.

1.1.2 Imaging Techniques Used to Diagnose and Monitor Cancer

Medical imaging plays a crucial role in many aspects of cancer management throughout the entire duration of a patient's care. In addition to providing initial detection of disease, imaging techniques are used to guide biopsies, to assess the stage of disease, to formulate treatment plans, and to evaluate therapeutic response (Barentsz *et al.* 2006). The most common techniques used clinically today include X-ray radiography and computed tomography (CT), ultrasound (US), magnetic resonance imaging (MRI), and positron emission tomography (PET) (Barentsz *et al.* 2006; Frangioni 2008).

X-ray radiography and CT rely on the principle of directing a beam of X-rays at a film or detector placed on the opposite side of the patient; the level of attenuation of the beam as it passes through the patient is determined by the density of the tissue encountered so that within the gray-scale images produced more dense tissues such as bone or calcifications appear white. With conventional X-ray, all structures are projected in one plane, but with CT the X-ray tube and detector rotate around the patient to produce axial images that can be reconstructed into three-dimensional images. By employing multiple detectors, several axial slices of the patient may be imaged simultaneously, allowing entire body scans to be completed within minutes. CT is at present the most

commonly used tool for assessment of cancer (Barentsz *et al.* 2006). One limitation of X-ray and CT is that good contrast is achieved only if the tumor attenuates X-rays much differently than the surrounding tissue. As a result, these methods are best suited for lung and bone cancer, although they are also used in breast mammography since there is good delineation between fat, tumor, and calcifications (Barentsz *et al.* 2006). Another drawback of using X-rays is that they are a type of ionizing radiation, which has been linked to increased risk of cancers later in life (Ron 2003; Smith-Bindman *et al.* 2009). Consequently, the necessity for employing these techniques should be carefully considered when other non-ionizing radiation imaging methods might be appropriate as well.

Ultrasound is a less commonly used technique in which sound waves reflected by tissue provide information about the separation of tissue planes and their relative acoustic impedance. For example, fluid-filled structures do not return a signal and appear black, while calcium returns a clear signal and appears white. The advantages of US are that it provides good soft tissue contrast, is easily applied, and relays information in real time, enabling it to be used to guide biopsies. However, image quality is highly operator-dependant and many parts of the body are inaccessible since the sound waves are highly scattered at bone and air interfaces (Frangioni 2008). Thus, its utility is mainly limited to gynecologic, liver, and kidney tumors.

Magnetic resonance imaging is another non-ionizing radiation method of cancer imaging. In MRI, a patient is placed within a strong magnetic field that causes the hydrogen ions in their tissues to align. An applied radiofrequency pulse then causes some of the ions to change alignment by a variable angle; when the pulse is removed

these ions return to their original alignment. This change in magnetization induces a voltage that is detected by a receiver coil around the patient, and is then processed into an image. The relaxation behavior is different for each type of tissue, enabling high contrast. Images can also be weighted by either the T1 or T2 relaxation times, producing images that are either fat sensitive (T1) or water sensitive (T2). MRI is critical for evaluation of brain and musculoskeletal tumors, but otherwise its use is limited because it is a lengthy and expensive procedure (Barentsz *et al.* 2006).

PET is different from the other imaging modalities listed in that it provides functional rather than structural information. This is accomplished through the use of radiolabeled substances that emit positrons as they decay within the body. These positrons collide with nearby electrons, producing two 511 keV annihilation photons traveling in opposite directions from each other that are then detected by a scintillator material in a scanner. The coincidence detection data is used to form a three-dimensional image (Kelloff et al. 2005). Contrast in PET is provided by differences in uptake of the radiolabeled substance between tissues. The main substance used in cancer imaging is fluorodeoxyglucose (FDG), a glucose analog that can pass through cell membranes via glucose transporters. The cellular uptake of FDG into tumors is increased over that of normal cells (which primarily utilize oxidative phosphorylation for energy) because cancer cells exhibit an increased rate of glycolysis, a phenomenon known as the Warburg effect (Kelloff *et al.* 2005). Recently, PET has been combined with CT in integrated PET-CT scanners that provide both functional and anatomic information, yielding a more powerful imaging technique (Barentsz *et al.* 2006).

Each of the above techniques has inherent strengths and weaknesses, and medical imaging will continue to improve with advances in technology. In the future it is likely that more imaging modalities that acquire both functional and anatomical information will emerge. Much excitement exists around new developments in molecular imaging, which has been broadly defined as the "visualization and characterization of biologic processes at the cellular and molecular level *in vivo*" (Abdullah 2006). This technique uses contrast agents capable of targeting cells based on their molecular characteristics, and later it will be discussed how nanoparticles could play a key role in the future of molecular imaging. It is predicted that molecular imaging will someday be used to detect cellular alterations early in disease progression, to evaluate and adjust treatment in real time, and to speed the drug development cycle (Weissleder 2006). Ultimately, having access to both structural and functional information about tumors should improve patient prognosis.

1.1.3 Current Therapeutic Approaches to Cancer

Conventional cancer treatment options include surgery, radiation, and chemotherapy and these may be used either alone or in combination. No matter which modality is used, the key to success lies in maximizing damage to tumor tissue while minimizing damage to healthy tissue. Here each will be described in brief.

Surgery involves physical removal of the tumor mass, and it is the most effective treatment option for cases of localized disease when the entire tumor is capable of being resected. Often adjacent healthy tissue is removed to provide a surgical margin between the diseased and healthy tissue because any residual disease left behind increases the patient's risk of later recurrence or metastasis. Of course, surgical removal of tumors

carries all the same risks associated with any surgery: dangers of anesthesia, blood loss, and infection. The morbidity and risk of mortality associated with surgical resection is largely dependent on tumor location, the percentage of healthy tissue removed, and the amount of lost normal tissue that can be replaced by the body (McKinnell et al. 1998). For example, resection of a brain tumor is a higher-risk procedure than removal of a localized skin carcinoma due to the sensitivity of the organ involved. For this reason it is important to develop minimally invasive treatments for brain tumors, and this is one of the overall goals of this thesis.

Radiation therapy exposes malignant cells to ionizing radiation from an external or implanted source to induce DNA damage, causing cells to die during mitosis (McKinnell *et al.* 1998). Radiation therapy is a regional therapy, meaning that the radiation is focused onto a specific predetermined treatment area and cells outside the irradiated area will remain unharmed. The cellular target for radiation is DNA, which is damaged either directly or indirectly by production of free radicals (Alison and Sarraf 1997). The goal of treatment is to induce double-stranded DNA breaks. Since radiation exerts its effects on proliferating cells, it is capable of damaging not only cancer cells but also any rapidly dividing normal cell within the radiation field. Thus, the effect of radiation on normal tissues is a dose-limiting factor.

Chemotherapy is the use of drugs to treat or control cancer. These compounds are typically administered systemically and can either target all proliferative cells or be cell cycle phase-specific. Chemotherapeutics are particularly useful when attempting to cure patients with multifocal or metastatic disease. On the other hand, allowing these very toxic chemicals to circulate throughout the body has a significant effect on tissues with

rapid renewal, which is why patients receiving chemotherapy often experience nausea, fatigue, hair loss, and thrombocytopenia. With the development of targeted therapeutics some of these symptoms have been alleviated, but there is still much to be accomplished.

In summary, the three main treatment options for cancer include surgery, radiotherapy, and chemotherapy. Although these techniques have become the standard of care, they still cannot guarantee that every cancer patient will be cured. In addition they are limited by cost, invasiveness, morbidity, and toxicity. Therefore, it is imperative to develop therapeutics that will be both minimally invasive and highly effective. This is the goal of nanomedicine, and advances in nanotechnology for cancer management to date will be discussed in the next section.

1.2 Nanotechnology in Cancer Management

1.2.1 Advantages of Nanoparticles

The past decade has seen explosive growth in the number of innovative technologies that use nanoparticles to image and treat cancer. The advantage of using nanoparticles in medical applications begins with their small size and large surface area-to-volume ratio. First, since research continues to reveal that changes at the molecular level are critical to tumor development, logic dictates that the disease should be combated at this scale. Furthermore, the small size of nanoparticles (typically 10-200 nm) allows them to accumulate in tumors by exploiting the leaky vascular network. It was previously mentioned that tumors are characterized by poorly organized vasculature with large intercellular gaps; these gaps allow nanoparticles to extravasate into the tumor bed and once there, the nanoparticles are retained because the lymphatic drainage system of

tumors does not operate effectively. Matsumura and Maeda first described this ability of nanoparticles to enter and remain in tumor tissue and it became known as the "enhanced permeability and retention effect" (the EPR effect) (Matsumura and Maeda 1986). Nanoparticles are said to utilize passive targeting when they rely on their small dimensions and the EPR effect to achieve high intratumoral concentrations.

The second advantage of nanoparticles is their large surface area-to-volume ratio, which allows for labeling with a variety of moieties that can enhance image contrast, improve therapeutic payload, or promote tumor uptake. It has been suggested that the ideal "nanovector" will include multiple functionalities, allowing several tasks to be achieved with a single platform. As shown in **Figure 1.3**, ideal nanovectors consist of three parts: the core material, the therapeutic/imaging payload, and the biological surface modifiers (Ferrari 2005). The surface modifiers could include "stealth" molecules that hide nanoparticles from the body's scavenger systems or targeting moieties that promote nanoparticle accumulation within tumors. The most common stealthing agent is poly(ethylene glycol) (PEG), which provides a dynamic, hydrophilic cloud of chains that reduces opsonization by macrophages of the reticuloendothelial system (RES), thereby increasing nanoparticle circulation time (van Vlerken *et al.* 2007). As mentioned earlier, cancer is characterized by mutations in oncogenes; these mutations can lead to over-expression of receptors on the tumor cell surface. The goal of adding targeting moieties to nanoparticles is to increase tumor retention time by facilitating binding with these receptors. Potential targeting moieties could include antibodies, peptides, and aptamers, and each of these will be discussed in more detail in Chapter 3.

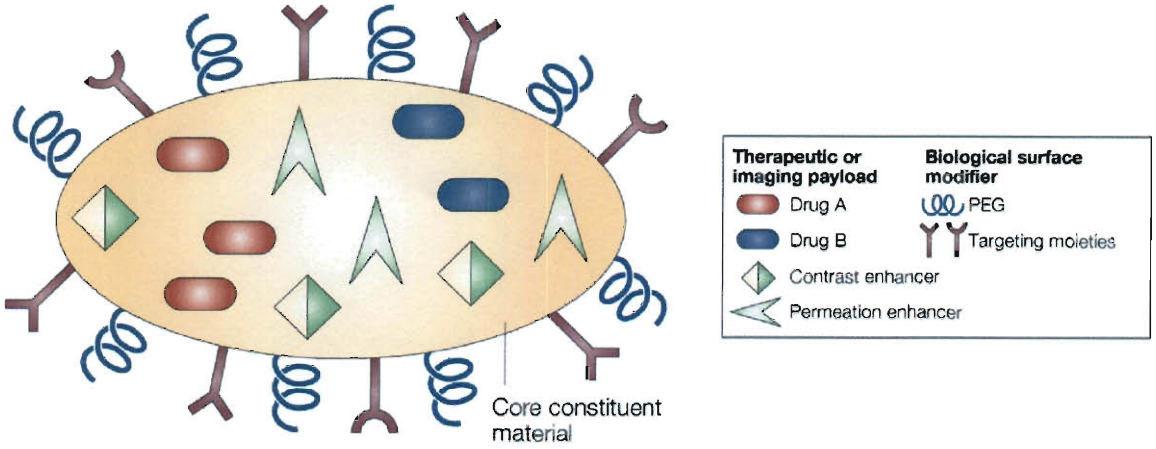

Figure 1.3: The ideal multifunctional nanoparticle. A multifunctional nanoparticle should be able to deliver therapeutic agents, amplify imaging signal with contrast enhancers, avoid biobarriers with permeation enhancers, prevent elimination from the circulation with PEG, and enhance tumor accumulation with targeting moieties. Image modified from Ferrari 2005.

Many nanoparticles are currently being studied for use in cancer imaging and therapy, and it would be impossible to provide a complete list here. However, in the next few sections some of the major advancements in cancer nanomedicine will be discussed. The use of nanoparticles as contrast agents will be introduced first, followed by the use of nanoparticles as drug delivery agents, and, lastly the use of nanoparticles as thermal therapeutics will be reviewed.

1.2.2 Nanoparticles as Contrast Agents

Nanoparticles' unique physicochemical properties, lack of overt toxicity, and ease of functionalization render them suitable as contrast agents. In addition, because they can be addressed to specific cellular targets, they offer potential for noninvasive molecular imaging and may be used to monitor changes in biological function such as enzyme activity, protein-protein interactions, or gene expression (Minchin and Martin 2010) in addition to providing anatomical tumor information. While a variety of nanoparticle

contrast agents are being developed, only quantum dots, gold-based nanoparticles, and iron-oxide nanoparticles will be discussed here.

Quantum dots (QDs) are core/shell crystalline semiconductors typically <10 nm diameter used with optical imaging modalities; some excellent reviews of QDs have been published (Michalet *et al.* 2005; Rhyner *et al.* 2006). These particles exhibit size-dependent emission that allows for tuning to the near-infrared region where imaging depth and signal-to-noise ratio are optimal. In addition, QDs exhibit molar extinction coefficients 10-50X that of organic dyes and they can be used in multiplexing. The most common quantum dot structure is a CdSe core with a ZnS shell, and it requires capping ligands to be soluble in aqueous solutions and appropriate for biological applications. Gao and colleagues recently developed QDs suitable for *in vivo* work by encapsulating them within a triblock copolymer and linking this amphiphilic polymer to tumor-targeting ligands (2004). These functionalized QDs could be imaged in tumor-bearing mice following either intravenous or subcutaneous delivery (Gao *et al.* 2004). While this was an exciting development, QDs' transition to clinical use is still limited by potential toxicity concerns, as there is some evidence that the particles leach Cd^{2+} and Se^{2-} ions (Michalet *et al.* 2005).

Gold-based nanoparticles are suitable contrast agents for a variety of imaging modalities, allowing oncologists to choose the imaging technique most appropriate for the tumor location. For example, optical coherence tomography (Cang *et al.* 2005; Gobin *et al.* 2007), photoacoustic tomography (Wang *et al.* 2004; Li *et al.* 2009; Song *et al.* 2009; Lu *et al.* 2010), and Raman spectroscopy (Zavaleta *et al.* ; Keren *et al.* 2008; Qian *et al.* 2008) have all been evaluated with gold-based nanoparticles as contrast agents.

Optical coherence tomography works similarly to ultrasound but utilizes reflections of light (rather than sound waves) through tissue to generate images. In photoacoustic tomography (PAT), tissue is irradiated with a short-pulsed laser and light absorption produces a rapid temperature rise and subsequent thermo-elastic expansion of the tissue. The pressure induced by this expansion prompts acoustic wave propagation, which is detected by an ultrasound transducer at the surface (Yuan and Jiang 2010). PAT is gaining popularity because it combines high contrast of optical imaging with high spatial resolution of ultrasound imaging. Finally, Raman spectroscopy is a technique that offers the potential to identify molecular species at the single-molecule level, and is dependent on the electromagnetic field enhancement that occurs with plasmonic nanostructures. Great strides have been made since the concept of surface enhanced Raman spectroscopy (SERS) first appeared (Jeanmaire and Van Duyne 1977), but technological advancements need to be made before this imaging modality will realize its full potential.

Since MRI is one of the most powerful techniques in cancer management, efforts have been made to enhance contrast with superparamagnetic iron-oxide nanoparticles (IONPs). In a landmark study, dextran-coated IONPs outperformed gadolinium (a clinical contrast agent) with respect to permanence of imaging enhancement and total areas with improved contrast, rendering the IONPs more suitable for postoperative imaging (Neuwelt *et al.* 2004). IONPs have also been radiolabeled to provide dual imaging capability with MRI and PET (Lee *et al.* 2008). As mentioned previously, nanoparticle formulations with multimodality possibilities will likely be critical players in the future of cancer nanomedicine. For this reason, Moore and colleagues have endowed dextran-coated IONPs with both imaging and therapy capabilities by conjugating the

nanoparticles to silencing RNA for image-guided gene therapy (Medarova *et al.* 2007). This development highlights the potential of nanoparticles to act as delivery vehicles, and in the next section more nanoparticle-based drug delivery schemes will be discussed.

1.2.3 Nanoparticles as Drug Delivery Agents

The goal of nanoparticle-mediated drug delivery is to reduce deleterious side effects and improve patient survival by increasing the relative proportion of drug delivered to the tumor versus the rest of the body. A variety of nanocarriers have been developed, including liposomes, polymeric nanoparticles, micelles, dendrimers, and more (Peer *et al.* 2007). Liposomes and polymer vesicles are the most commonly investigated agents, and they provide the benefit of allowing both covalent and non-covalent encapsulation of hydrophobic and hydrophilic drugs (Janib *et al.* 2010). The first clinically used nanoparticle was a PEGylated liposomal formulation of doxorubicin (Doxil^{TM}) and it has been indicated for use in Kaposi's sarcoma, breast cancer, and refractory ovarian cancer (Ferrari 2005). Compared to the free drug, liposomal doxorubicin has prolonged circulation and decreased toxicity (Batist *et al.* 2001). Since the introduction of Doxil^{TM}, two more non-PEGylated liposomal drugs (DaunoXome and Myoset) have been used clinically (Peer *et al.* 2007).

While drugs encapsulated inside or bound to nanoparticles have shown much promise in improving chemotherapy, there is still little or no control over the release profile. The future of drug delivery for cancer and other diseases will likely utilize "smart" nanomaterials that can release their therapeutic payload at the desired site upon triggering from biological cues or on-demand (Couvreur and Vauthier 2006). For example, since the tumor microenvironment is often acidic, liposomes and polymer

vesicles that release drugs at acidic pH have been developed (Ding *et al.* 2010; Yang *et al.* 2010). Similarly, enzymatic degradation of drug-polymer conjugates and liposomal carriers has been proposed since enzymes such as matrix metalloproteases (MMPs) are present at high levels in tumor tissue (Chau *et al.* 2006; Hatakeyama *et al.* 2007). While these first two approaches utilize biological cues to prompt drug release, the use of local hyperthermia for on-demand tumor-specific drug delivery has been proposed since 1978 (Yatvin *et al.* 1978). *In vivo* work showed that temperature-sensitive liposomes containing doxorubicin were significantly more effective at eliminating subcutaneous squamous cell carcinoma tumors in mice than free drug or non-temperature sensitive liposomes when release was initiated by the simple heating technique of placing the animal's leg in a warm water bath (Needham *et al.* 2000). More recently, nanoparticles capable of absorbing light and converting the energy into heat have been used as a more sophisticated source of heat generation. When modified with drugs and exposed to light, hollow-gold nanoshells (Braun *et al.* 2009; You *et al.* 2010), nanorods (Wei *et al.* 2008), and PLGA-gold half-shells (Park *et al.* 2009), have all demonstrated the ability to heat and subsequently release their therapeutic payloads. These systems offer the added benefit that hyperthermia has cytotoxic effects as well. In the next section, the use of nanoparticles for thermal therapy as a standalone treatment will be described.

1.2.4 Nanoparticles as Thermal Therapeutics

The benefits of hyperthermia in medicine have been known for some time: Hippocrates once stated, "Give me a fever, and I can cure any illness" (ca. 400BC). While hyperthermia has been used as adjuvant cancer treatment, it is not currently utilized as an independent treatment modality. Sources for heat generation, which induces cell death

through such mechanisms as protein denaturation and rupture of cellular membranes, include radiofrequency and microwaves, laser light, and ultrasound (Wust *et al.* 2002). Unfortunately, simple heating techniques fail to discern normal from diseased tissue, preventing the widespread use of this technology. To overcome this limitation, researchers are evaluating the use of nanoparticles as exogenous energy absorbers to provide specific delivery of heat selectively to tumors. Here, some of the successes achieved with nanoparticles will be highlighted. Parts of this section are derived from the co-authored review article: Day ES *et al.* "Nanoparticles for Thermal Cancer Therapy." Journal of Biomechanical Engineering (2009); 131 (7): 074001.

The three sources most commonly used to activate nanoparticle heating are radiofrequency waves, magnetic fields, and near-infrared light. With radiofrequency ablation (RFA), an electrode inserted into a tumor applies a radiofrequency current that induces agitation of ions within the tissue, leading to frictional heating (Curley 2001). The conductivity properties of gold nanoparticles (Cardinal *et al.* 2008; Gannon *et al.* 2008) and single-walled carbon nanotubes (Gannon *et al.* 2007) provide the possibility of more efficient heating, allowing RFA to be accomplished noninvasively, with reported penetration depths of 7-17 cm. While RFA uses radiofrequencies to produce an alternating electric field, magnetic fluid hyperthermia uses radiofrequencies to generate an alternating magnetic field. This offers the advantage that the irradiation can reach all tissues in the body. Heat generation of magnetic nanoparticles exposed to this field is a result of energy losses during the magnetization reversal process. The first attempt to heat tissue with magnetic materials was performed by Gilchrist *et al.* (1957), and since then the field has advanced greatly. Recently, the first clinical studies regarding

magnetic fluid hyperthermia were published, demonstrating the feasibility of this therapy for treatment of prostate cancer (Johannsen *et al.* 2005; Johannsen *et al.* 2007) and glioblastoma multiforme (Maier-Hauff *et al.* 2007; Maier-Hauff *et al.* 2010). These studies incorporated aminosilane-coated iron-oxide nanoparticles. While iron-oxide is the most common choice of material for magnetic hyperthermia, a recent article suggested that carbon-coated iron could be an excellent alternative (Xu *et al.* 2010).

The most extensively studied approach to thermal cancer therapy is excitation of nanoparticles with near-infrared light, and within this field plasmonic gold-based nanoparticles have received the most attention because they are biocompatible and their optical properties can be tuned by adjusting particle size, shape, and composition. When these nanoparticles are exposed to light at their resonance wavelength, the conduction-band electrons begin to oscillate in unison, resulting in light absorption or scattering (Kennedy *et al.* 2010). Therapeutic applications take advantage of the fact that some of the absorbed light energy is converted into heat that induces damage of nearby cells; thus this approach to cancer treatment is known as photothermal therapy. Some of the nanoparticles investigated for photothermal therapy include gold nanorods (Dickerson *et al.* 2008), gold nanocages (Chen *et al.* 2007; Chen *et al.* 2010), hollow gold nanoshells (Lu *et al.* 2009), gold-gold sulfide nanoparticles (Gobin *et al.* 2010), and silica-gold nanoshells (Hirsch *et al.* 2003; Gobin *et al.* 2007). This thesis aims to further develop photothermal therapy with gold-gold sulfide nanoparticles and silica-gold nanoshells, so in Section 1.3 these particles will be described in more detail. Section 1.3 is partially adapted from the following co-authored book chapters: Bickford *et al.* (2010) and Morton *et al.* (2010).

1.3 Introduction to Silica-Gold Nanoshells and Gold-Gold Sulfide Nanoparticles

Gold-based nanoparticles are perhaps the most thoroughly studied among the numerous nanoparticles being explored as agents for cancer management, partially attributed to the well-documented uses of gold in human history. Starting from Faraday's investigation of colloidal gold in the middle 1800s, optical properties of metal nanoparticles have long been of interest in physical chemistry. This exploration led to a major breakthrough in the middle 1990s when core-shell structures were discovered to have highly tunable optical properties. In general, a nanoshell can be classified as any nanoparticle composed of a core coated with different materials. The first experimentally developed metal nanoshell consisted of an Au_2S dielectric core surrounded by a gold shell (Zhou *et al.* 1994), although it was later proposed that these nanoparticles actually consist of a gold aggregate structure (Norman *et al.* 2002). The ensuing debate about their composition remains ongoing today (Raschke *et al.* 2005; Zhang *et al.* 2005; Schwartzberg *et al.* 2007), so within this thesis these nanoparticles will be referenced more generally as gold-gold sulfide nanoparticles. More recently, a new nanoshell design consisting of a silica (SiO_2) core coated with a thin layer of gold was developed (Oldenburg *et al.* 1998). Since their inception, silica-based gold nanoshells have been studied as instruments for achieving superior diagnostic imaging applications, photothermal therapy, laser-tissue welding, controlled drug delivery, and for immunoassays (reviewed in Hirsch *et al.* (2006)). The following sections will discuss the properties of these two types of nanoparticles and then describe their current use in cancer management.

1.3.1 Optical Properties

The optical properties of gold-gold sulfide nanoparticles and silica-gold nanoshells, particularly the scattering and absorbing cross-sections, can be obtained using the Mie solution to Maxwell's equations, or Mie theory, for concentric spheres. Since the diameter (d) of both gold-gold sulfide nanoparticles and nanoshells is much less than the wavelength of the incident electromagnetic field (λ), that is $d << \lambda$, Mie theory calculations can be performed using the quasi-static approach in which spatial variation is ignored but temporal dependence is preserved. To further simplify the calculations, the particles are approximated as perfect spheres and dipole-dipole interactions are neglected since the particle concentration in solution is low. The complete derivation of the optical properties of gold-gold sulfide nanoparticles using Mie theory has been published by Averitt *et al.*, so only important results of the derivation will be discussed here (1999). **Figure 1.4** displays the geometry used in performing Mie scattering simulations (Averitt *et al.* 1999). To solve the equations, the dielectric constants of the core (ε_1), shell (ε_2), and dispersive medium (ε_3) must be known, as well as the radius of the core (r_1) and whole particle (r_2).

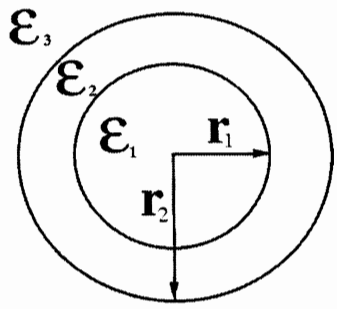

Figure 1.4: Nanoshell geometry used in Mie theory calculations. The core radius is r_1 and the total particle radius is r_2. The dielectric constants ε_1, ε_2, and ε_3 are those of the core, shell, and dispersive medium, respectively. Image from Averitt *et al.* 1999.

To determine the scattering and absorption cross-sections of the particles, some definitions must first be made. As shown in Equation 1, P is the ratio of shell volume to total particle volume and it is needed to define ε_a and ε_b, displayed in Equations 2 and 3. These are subsequently used to solve for the polarizability (α) in Equation 4, where ε_o is the permittivity of free space, 8.85×10^{-12} F/m. Polarizability describes the tendency of charge distribution to be distorted by an external electric field.

$$P = 1 - \left(\frac{r_1}{r_2}\right)^3 \qquad \textbf{Equation 1}$$

Equation 2

$$\varepsilon_b = \varepsilon_1 P + \varepsilon_2 (3 - P) \qquad \textbf{Equation 3}$$

$$\alpha = 4\pi\varepsilon_o r_2^{\,3}\left[\frac{\varepsilon_2\varepsilon_a - \varepsilon_3\varepsilon_b}{\varepsilon_2\varepsilon_a + 2\varepsilon_3\varepsilon_b}\right] \qquad \textbf{Equation 4}$$

Plasmon resonance of the electrons in the shell occurs at the point of maximum polarizability, which takes place when the denominator of Equation 4 approaches zero. Using the polarizability equation and the above definitions, the absorption (Equation 5) and scattering (Equation 6) cross sections can be obtained. Averitt *et al.* used these relationships to show that the wavelength of resonance depends on the ratio of the core radius to the total particle radius, seen in Equation 7 (1999).

$$\sigma_{abs} = \frac{8\pi^2\sqrt{\varepsilon_3}}{\lambda} r_2^{\,3}\,\mathrm{Im}\left(\frac{\varepsilon_2\varepsilon_a - \varepsilon_3\varepsilon_b}{\varepsilon_2\varepsilon_a + 2\varepsilon_3\varepsilon_b}\right) \qquad \textbf{Equation 5}$$

$$\sigma_{sca} = \frac{128\pi^5}{3\lambda^4}\varepsilon_3^{\,2} r_2^{\,6}\left|\frac{\varepsilon_2\varepsilon_a - \varepsilon_3\varepsilon_b}{\varepsilon_2\varepsilon_a + 2\varepsilon_3\varepsilon_b}\right|^2 \qquad \textbf{Equation 6}$$

$$\frac{r_1}{r_2} = \left[1 + \frac{3}{2}\frac{\varepsilon_2'(\lambda)(\varepsilon_1 + 2\varepsilon_3)}{\left[\varepsilon_2'(\lambda)\right]^2 - \varepsilon_2'(\lambda)(\varepsilon_1 + \varepsilon_3) + \left\{\varepsilon_1\varepsilon_3 - \left[\varepsilon_2''(\lambda)\right]^2\right\}}\right]^{\frac{1}{3}}$$

Equation 7

The relationship displayed in Equation 7 is important because it shows that the wavelength of plasmon resonance can be tuned based on particle geometry. For example, with a given shell thickness, a larger particle diameter shifts the peak plasmon resonance to longer wavelengths. Although these calculations were performed based on the values for gold-gold sulfide nanoshells, Oldenburg *et al.* showed that tunable optical resonances are also achievable with silica-gold nanoshells (1998). **Figure 1.5** shows how nanoshells with a silica core can be tuned to have a peak plasmon resonance throughout the electromagnetic spectrum by altering the ratio of the core to total particle radius.

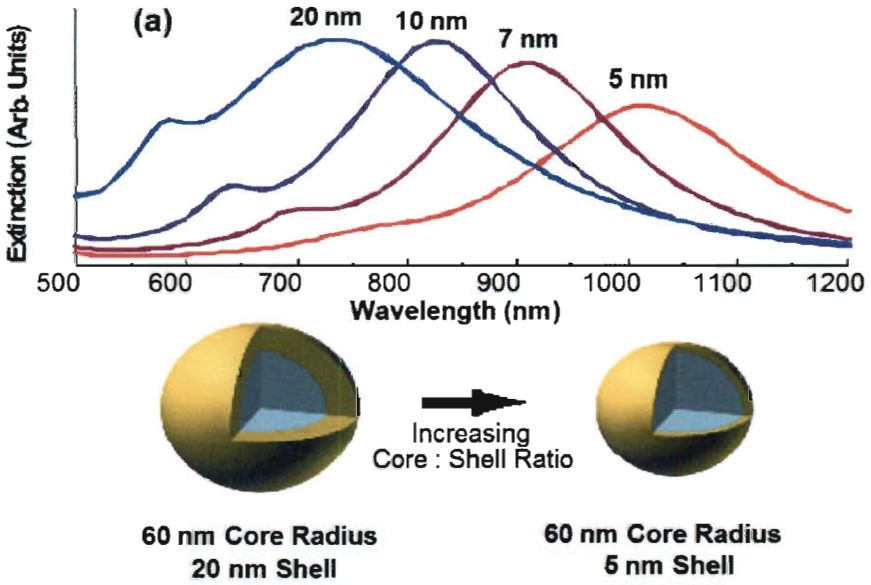

Figure 1.5: Optical resonances of nanoshells calculated with Mie theory. Nanoshells with a fixed 60 nm core radius display a shift in peak extinction of over 300 nm as the gold shell thickness decreases from 20 nm to 5 nm. Image from Day *et al.* 2010.

The optical "tunability" of nanoshells and gold-gold sulfide nanoparticles renders them desirable for many biomedical applications, as will be discussed in the following section. In this thesis, nanoshells and gold-gold sulfide nanoparticles will be compared for use in imaging and treatment of breast and brain tumors.

1.3.2 Applications in Cancer

The ability to synthesize nanoshells and gold-gold sulfide nanoparticles (GGS-NPs) with peak extinction in the near infrared (NIR) region of the electromagnetic spectrum makes them particularly attractive for use as cancer diagnostic and therapeutic agents. This may be understood by considering interactions between light and tissue. There is a wavelength-dependent absorption of light by native chromophores in tissue, with the two main absorbers of visible and infrared light being water and hemoglobin. As seen in **Figure 1.6**, there is low absorbance by each of these tissue components in the "NIR window" from 650-900 nm (Weissleder 2001). Within this region light may penetrate deeply into tissue, allowing for noninvasive imaging and therapy of cancer when combined with nanoparticles having their peak extinction at the same wavelength. By definition, extinction measures the amount of energy removed from incident light and is a combination of both absorption and scattering. Absorbed energy is mainly dissipated as Ohmic heating, which enables nanoshells and GGS-NPs to be used for photothermal applications, such as controlled drug delivery (Sershen *et al.* 2000; Bikram *et al.* 2007; Huang *et al.* 2008) and cancer hyperthermia (Hirsch *et al.* 2003; O'Neal *et al.* 2004; Gobin *et al.* 2010). Meanwhile, scattered light permits nanoshells to serve as contrast agents for several imaging applications, such as darkfield microscopy (Loo *et al.* 2005) and optical coherence tomography (OCT) (Gobin *et al.* 2007). The next few paragraphs

will overview some of the research accomplishments with gold-gold sulfide nanoparticles and nanoshells that provided a foundation for this thesis.

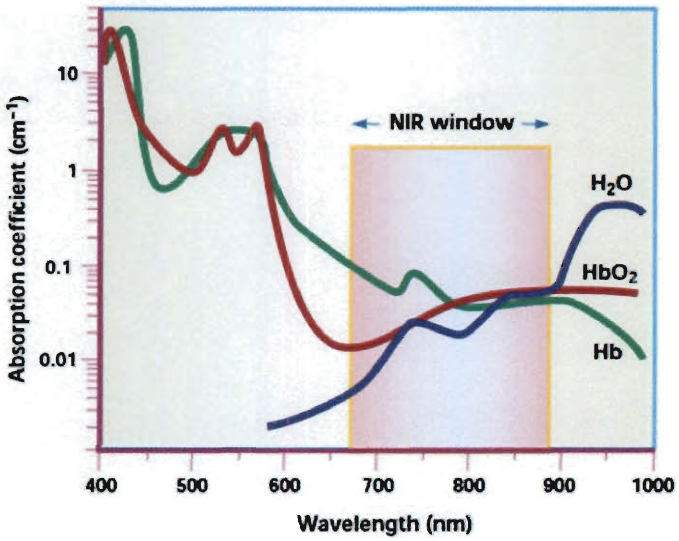

Figure 1.6: Absorption coefficient of major chromophores in tissue. Near infrared (NIR) wavelengths of light are best suited for biological applications due to minimal absorption by native tissue components. This region is thus dubbed the "NIR window." Image from Weissleder 2001.

Cancer imaging and photothermal therapy mediated by gold-gold sulfide nanoparticles (GGS-NPs) or nanoshells (NS) can be summarized in a few steps. First, these nanoparticles must accumulate within the tumor, and this can be accomplished via intratumoral or intravenous delivery. When administered intravenously, nanoparticles utilize the EPR effect described earlier to accumulate within the tumor. Once a sufficient number of nanoparticles are within the tumor, imaging or therapy can be performed. For therapy, a NIR laser applied transdermally induces heating of the nanoparticles and subsequent necrosis of the tumor tissue. This process is depicted schematically in **Figure 1.7**.

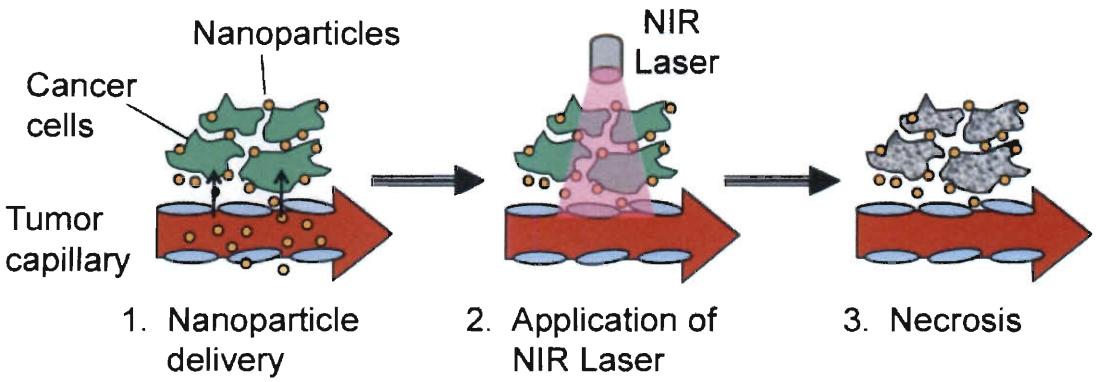

Figure 1.7: The steps of nanoparticle-mediated photothermal therapy. First, nanoparticles delivered intravenously accumulate in the tumor by passing through inter-endothelial cell openings. If desired, imaging may be performed to confirm nanoparticle presence. Second, a near-infrared laser is externally applied to the tumor region for a few minutes. This induces heating of the nanoparticles sufficient to induce cancerous cell death and necrosis of the tumor tissue.

In 2003, Hirsch *et al.* were the first to demonstrate nanoparticle-mediated photothermal therapy using nanoshells to induce damage to SK-BR-3 human breast carcinoma cells *in vitro* (Hirsch *et al.* 2003). In the same report, they demonstrated the effects of this therapy *in vivo*. Transmissible venereal tumors grown subcutaneously in SCID mice were injected with PEG-passivated nanoshells or saline and then a NIR laser was applied (820 nm, 4 W/cm^2, <6 min). Temperature measurements acquired during laser application demonstrated a mean temperature increase in the nanoshell group of almost 40°C, compared to only 10°C in the control group. Histology of excised tumors confirmed that tissue damage was confined to areas of nanoshell localization (**Figure 1.8**). This was the first time that local heat delivered by light-activated nanoshells was shown to damage tumor tissue *in vivo*.

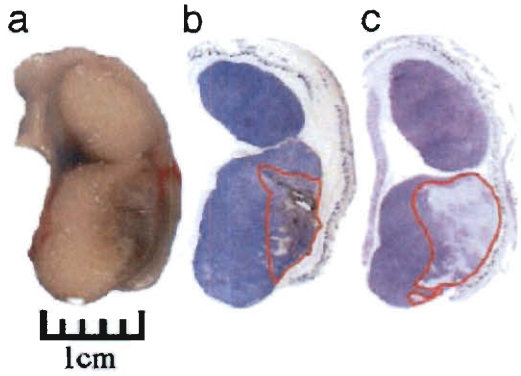

Figure 1.8: Damage due to photothermal therapy is confined to regions within tumors that contain nanoshells. (a) Gross pathology of a tumor treated with nanoshells and NIR laser exposure. (b) Nanoshell location identified by silver staining. (c) Tissue damage in the region with nanoshells confirmed by H&E staining. (Hirsch *et al.* 2003)

Following this study, the ability of intravenously administered PEG-coated nanoshells to thermally ablate tumors and thereby improve animal survival was verified with a subcutaneous murine tumor model (O'Neal *et al.* 2004). As shown in **Figure 1.9**, mice bearing CT26 colon carcinoma tumors that received nanoshell therapy displayed complete tumor regression and remained 100% tumor-free for the duration of the study. By comparison, the mean lifespan was 10.1 days for the non-treated group and 12.5 days for mice that received only laser exposure. This was the first demonstration that nanoshells delivered systemically could accumulate in tumors at levels sufficient for photothermal tumor destruction. Since these first two studies with breast and colon carcinoma tumors were published, *in vitro* studies have demonstrated that nanoshell-mediated photothermal therapy is also effective against prostate (Stern *et al.* 2007; Gobin *et al.* 2008), brain (Bernardi *et al.* 2008), and liver cancers (Liu *et al.* 2010). Currently, photothermal therapy with PEG-coated nanoshells is being investigated in a Phase I clinical trial for treatment of refractory head and neck cancer (ClinicalTrials.gov 2010).

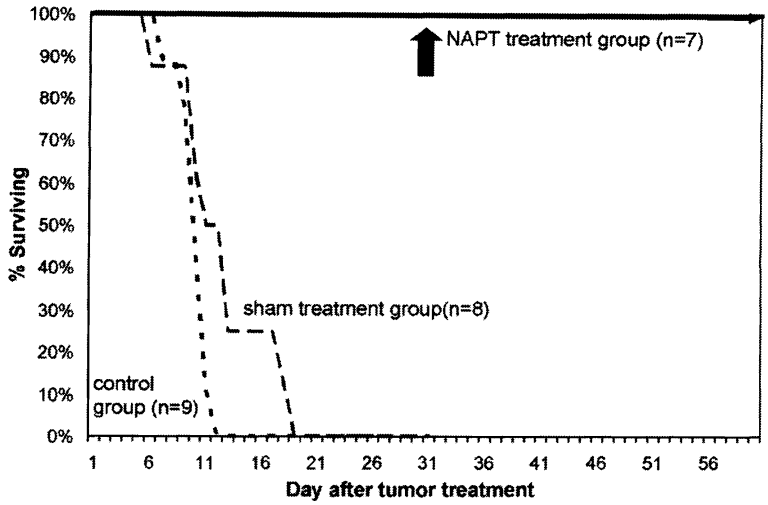

Figure 1.9: Nanoshell-assisted photothermal therapy improves survival of tumor-bearing mice. This plot depicts the differences in survival time for mice bearing CT26 tumors that received no treatment, sham treatment (laser only), or nanoshell-assisted photothermal therapy (NAPT). (O'Neal *et al.* 2004)

Although gold-gold sulfide nanoparticles were invented before silica-gold nanoshells, it wasn't until recently that their potential as mediators of photothermal therapy was tested. In a novel study, Gobin *et al.* used Mie theory to prove that GGS-NPs have a larger ratio of absorption to scattering than nanoshells (2010). Then, using a subcutaneous murine tumor model, it was shown that these particles are equally effective at inducing tumor regression. Importantly, the GGS-NPs accumulated in the tumors used in this study over a longer timeframe than the silica-gold nanoshells; consequently therapy was more effective for GGS-NPs if the laser was applied 48 h post-intravenous injection (82% survival) rather than 24 h (71% survival). For silica-gold nanoshells the maximum tumor accumulation occurred at 24 h, and following laser application at that time the mice experienced 82% survival (Gobin *et al.* 2010). This result emphasizes the importance of understanding nanoparticle distribution profiles so that the exciting energy source is applied at the proper time to maximize treatment effect.

For future clinical success, it may be necessary to exploit the ability of nanoshells and gold-gold sulfide nanoparticles to act as contrast agents for a variety of imaging modalities; this could allow nanoparticle accumulation in the tumor to be monitored in real time, guiding decisions regarding when the laser should be applied. At present, nanoshells, but not GGS-NPs have been tested as *in vivo* contrast agents. Using optical coherence tomography, Gobin *et al.* successfully monitored nanoshell accumulation in subcutaneous tumors (**Figure 1.10**) and showed that these same nanoshells could also be used for photothermal therapy (2007). Similarly, two-photon microscopy has been used to monitor nanoshell accumulation in tumors and relate particle position to tumor vessels (**Figure 1.11**) (Park *et al.* 2008). One aim of this thesis is to prove that GGS-NPs are also suitable contrast agents for two-photon microscopy; this ability will be demonstrated in Chapter 4.

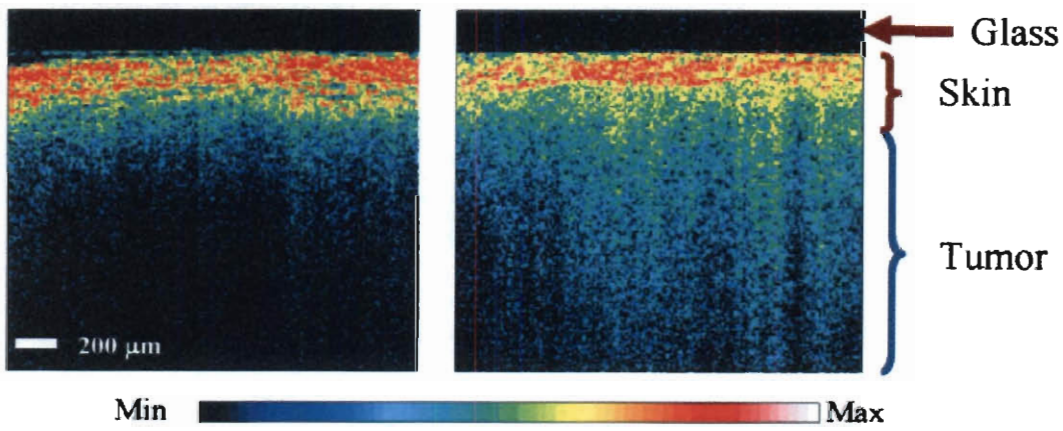

Figure 1.10: Optical coherence tomography (OCT) detects nanoshells in tumor tissue. The left and right panels show an OCT image from a tumor in a mouse that received saline or nanoshells, respectively. There is a significant increase in contrast intensity in the presence of the nanoshells. (Gobin *et al.* 2007)

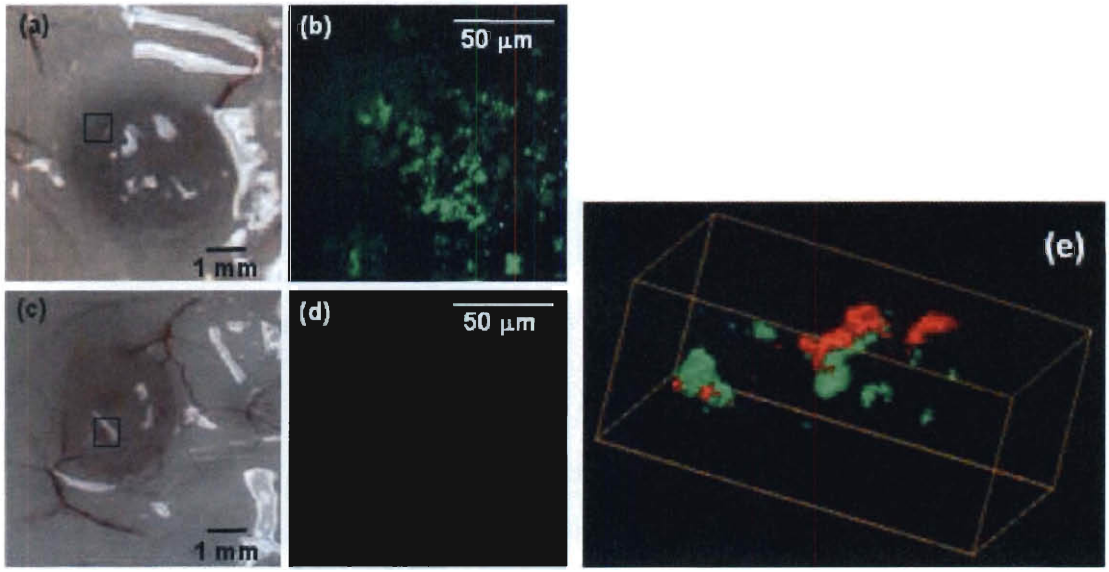

Figure 1.11: Nanoshells can be visualized in tumors with two-photon microscopy. White light (a,c) and two-photon photoluminescence (b,d,e) images from mice injected with nanoshells (a,b,e) or saline (c,d). 3D visualization (e) of nanoshells (green) and blood vessels (red) demonstrates that the nanoshells are proximal to the tumor vessels. (Park *et al.* 2008)

To provide the best possible imaging and therapy of cancer with nanoshells and gold-gold sulfide nanoparticles, their accumulation within tumors should be maximized. Some insight into the pharmacokinetics of these materials has been gained by studies investigating the biodistribution of PEG-coated nanoparticles in mice (James *et al.* 2007; Gobin *et al.* 2010). As previously mentioned, however, it is predicted that coating nanoparticles with targeting moieties should prolong the accumulation in the tumor and provide new opportunities for molecular-specific imaging and therapy. Working towards this goal, several groups have developed methods to functionalize nanoshells with antibodies or peptides, thereby enabling cell-specific binding (Loo *et al.* 2005; Gobin *et al.* 2008; Liu *et al.* 2010). For example, as shown in **Figure 1.12**, nanoshells coated with anti-IL13Rα2 antibodies bind U373 human high-grade glioma cells that over-express IL13Rα2 (interleukin 13 receptor alpha 2) to enable thermal therapy (Bernardi *et al.*

2008). In Chapter 4 it will be demonstrated that GGS-NPs can be molecularly addressed using the same chemistry described for silica-gold nanoshells. One flaw of all these preliminary targeting studies, however, is that they were performed *in vitro*, and it remained unknown if altering the surface coating on nanoshells and GGS-NPs would significantly alter their organ distribution and tumor accumulation profile *in vivo*. Therefore, one major goal of this thesis was to provide insight to this question. In Chapter 3 it will be shown that antibody-coated nanoshells can bind ovarian tumor tissue *ex vivo* at levels corresponding to the receptor expression, suggesting that targeting mechanisms should continue to work in the more complex *in vivo* environment. The biodistribution of targeted and PEG-coated nanoshells and GGS-NPs in tumor-bearing mice will be presented in Chapters 5 and 6.

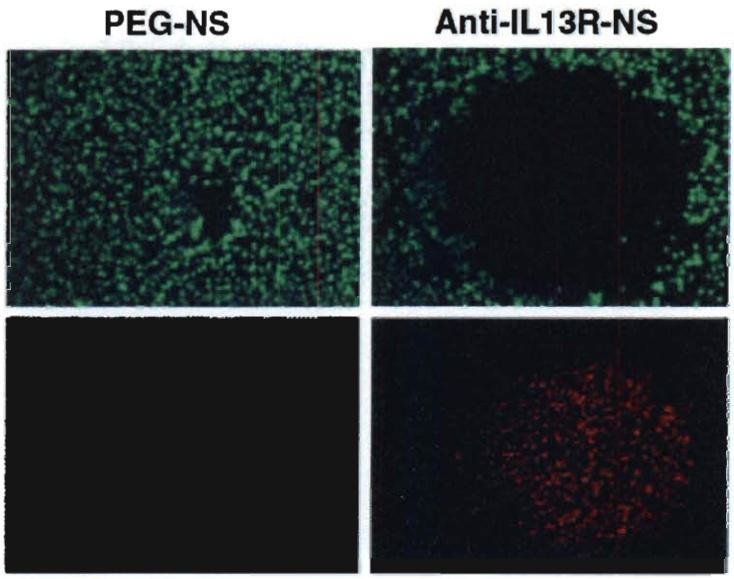

Figure 1.12: Antibody-coated silica-gold nanoshells bind targeted cells to mediate photothermal therapy. U373 cells that over-express the receptor IL13Rα2 were exposed to PEG-NS or Anti-IL13Rα2-NS prior to laser irradiation. Calcein AM and ethidium homodimer-1 staining was performed to show live cells (green) and dead cells (red). Only antibody-coated nanoshells bound the targeted cells at levels sufficient to induce thermal damage upon laser irradiation. (Bernardi *et al.* 2008)

1.4 Conclusions: Opportunities to Advance Cancer Therapy with Nanoshells and Gold-Gold Sulfide Nanoparticles

This thesis seeks to advance cancer therapy by further developing photothermal therapy mediated by nanoshells and gold-gold sulfide nanoparticles. Photothermal therapy offers numerous benefits over conventional cancer therapy: compared to surgery, photothermal therapy is much less invasive; and, in contrast to radiation and chemotherapy, the mechanism of action is imparted only at desired locations when the laser is applied, creating a therapy that should have few side effects. Photothermal therapy is also advantageous compared to magnetically induced heating of nanoparticles because much lower concentrations of nanoparticles are required (minimizing toxicity concerns) and because the procedures are faster and do not require expensive, specialized equipment.

Silica-gold nanoshells and gold-gold sulfide nanoparticles were chosen for investigation in this thesis from among the many nanoparticles that could be used for near-infrared photothermal therapy for several reasons. First, these nanoparticles are simple to fabricate and do not present toxicity concerns since the outer layer is comprised of metallic gold which has been shown to be relatively inert and thus biocompatible. Comparatively, nanorods require capping with cetyltrimethylammonium bromide (CTAB) during synthesis, which has known toxicities and must be replaced before *in vivo* application (Niidome *et al.* 2006). The compatibility of gold nanocages and hollow gold nanoshells remains to be validated in thorough studies, although it is anticipated that these nanoparticles will be non-toxic. Second, the gold outer layer of nanoshells and GGS-NPs provides an added benefit as a surface readily available for bioconjugation. Finally, a third consideration in choosing a nanoparticle platform is the photothermal

transduction efficiency, defined as the proportion of incident light being converted into photothermal power. Cole *et al.* found that for solutions of nanoparticles at equal optical densities gold-gold sulfide nanoparticles and nanorods have similar photothermal transduction efficiencies that are higher than that of silica-gold nanoshells; though, when calculated on a per-particle basis, silica-gold nanoshells have the highest transduction cross section (Cole *et al.* 2009). Notably, all of these differed by less than a factor of 3, suggesting that there is likely not a significant advantage of one nanoparticle versus another. Therefore, based on all these criteria, it was determined to include both gold-gold sulfide nanoparticles and silica-gold nanoshells in these experiments.

Previous research has indicated that PEG-coated nanoshells and gold-gold sulfide nanoparticles may be used in cancer management, and it has been predicted that the addition of targeting moieties to the nanoparticle surfaces will enhance cancer therapy by improving nanoparticle retention within tumors. This thesis aims to evaluate the benefits of molecular targeting through a series of experiments. To begin, Chapter 2 explains the methods used to synthesize nanoparticles for these experiments. In Chapter 3, the ability of antibody-coated nanoshells to specifically bind and treat cancerous cells in co-culture with non-targeted normal cells is demonstrated. In addition, the potential of antibody-coated nanoshells to act as *ex vivo* diagnostic agents is shown. Using an *in vitro* model, Chapter 4 proves that antibody-coated gold-gold sulfide nanoparticles can be used as dual imaging and therapeutic agents. The second half of this thesis then focuses on *in vivo* validation of targeting schemes using high-grade glioma as a model tumor. Chapter 5 describes the first attempt to compare the distribution of antibody-coated and PEG-coated nanoparticles in tumor-bearing mice. The sensitivity of glioma to nanoparticle-mediated

photothermal therapy is also established. Finally, Chapter 6 demonstrates the ability to treat intracranial glioma tumors using vascular-targeted nanoparticles. To conclude this thesis, Chapter 7 summarizes the importance of the results, overviews the potential applications, and discusses the future directions for enhancing cancer imaging and photothermal therapy through targeted delivery of nanoparticles.

Chapter 2: Methods for Nanoparticle Synthesis, Stabilization, and Characterization

2.1 Introduction

This chapter presents the methods used throughout this thesis to synthesize, stabilize, and characterize silica-gold nanoshells and gold-gold sulfide nanoparticles.

2.2 Synthesis of Silica-Gold Nanoshells

A four-step process developed by Oldenburg *et al.* was used to fabricate nanoshells consisting of spherical silica cores and thin gold shells (Oldenburg *et al.* 1998). First, colloidal silica (120 nm diameter, synthesized or purchased from Precision Colloids, Cartersville, GA) was functionalized with 3-aminopropyl-triethoxysilane and decorated with small (~3 nm) gold colloidal particles. These gold colloid islands provided nucleation sites where additional gold could be reduced until a complete shell was formed. More thorough details of the production process are outlined below.

2.2.1 Formation and Functionalization of Silica Nanoparticles

Silica nanoparticles were formed following the Stöber method (Stöber *et al.* 1968). To produce ~120 nm diameter silica spheres 2.7-3.1 ml ammonium hydroxide (NH_4OH, 28%, Aldrich, St. Louis, MO) was added to 45 ml 200 proof ethyl alcohol (EtOH) and, while stirring rapidly, 1.5 ml tetraethyl orthosilicate (TEOS, Aldrich) was added. After the mixture reacted overnight, the nanoparticle solutions were centrifuged twice (1750 g, 30 min each) and re-suspended in EtOH. The silica nanoparticles were sized using

scanning electron microscopy and only batches with polydispersity less than 10% were used for subsequent steps.

To promote binding of negatively charged gold colloid to the silica nanoparticles, the silica surfaces were terminated with positively charged amine groups. This was accomplished by adding 5 µl 3-aminopropyltriethoxysilane (APTES, Aldrich) per 1 ml silica cores (at 4% by weight), and the reaction proceeded at room temperature for at least 8 h. To encourage covalent bonding of silane groups to the surface, the spherical particles were then boiled for 1 h at 75°C while maintaining a constant volume in EtOH. This was followed by another two-step centrifugation (1750 g, 15 min) and re-suspension in fresh EtOH.

2.2.2 Gold Colloid Formation and Seed Growth

Gold colloid particles (~3 nm diameter) were prepared as described in the literature (Duff *et al.* 1993). A working dilution of tetrakis(hydroxylmethyl)phosphonium chloride (THPC) was made by addition of 400 µl THPC (Aldrich) to 33 ml Millipore water. Then, while stirring rapidly, 4 ml of the THPC dilution and 1.2 ml 1 M NaOH (Aldrich) were added to 180 ml Millipore water chilled to 10°C. After stirring 5 min, 6.75 ml of 1% chloroauric acid ($HAuCl_4$, Aldrich) was quickly added, resulting in a light reddish-brown suspension of colloid which was subsequently aged at 4°C for a minimum of 2 weeks to allow the gold particles to reach the correct size.

Seed particles are the precursors to silica-gold nanoshells are they are comprised of silica cores with evenly dispersed gold particles adsorbed to the surface. To make seed particles, 40 ml gold colloid was mixed with 300 µl amine-functionalized cores and 4 ml 1 M NaCl. This reacted 2-3 days and the resulting seed was washed with Millipore water

through centrifugation (1650 g, 25 min, performed twice). Lastly, seed particles were diluted with Millipore water to an extinction of 0.1 units at 530 nm wavelength. The seed formation process is illustrated in **Figure 2.1 (a)** and a transmission electron micrograph of a single seed particle is shown in **Figure 2.1 (b)**.

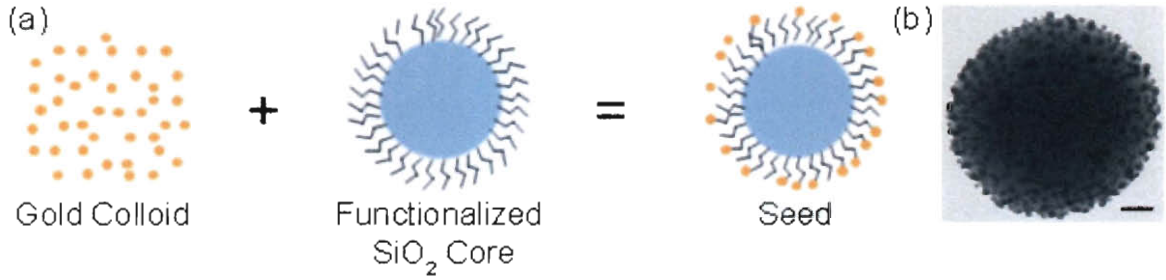

Figure 2.1: Production of "seed" nanoparticles. (a) Reacting gold colloid with amine-functionalized silica nanoparticles yields "seed" nanoparticles composed of a discontinuous metal surface on a dielectric core. (b) Representative TEM of a seed particle. Scale bar = 20 nm.

2.2.3 Shell Growth

The final step in formation of nanoshells is completion of the gold shell. First, a mixture of 12 ml of 29.7 mM $HAuCl_4$ and 800 ml 1.8 mM potassium carbonate was prepared and aged for a minimum of 24 h; this solution is referred to as KCarb-Gold. Optimization sweeps were performed in small quantities to determine volume ratios of seed solution to KCarb-Gold that produced nanoshells with the desired extinction characteristics; typically ratios ranged from 200-500 µl seed per 1 ml KCarb-Gold. Once determined, the appropriate ratio was scaled up linearly to produce larger volumes of nanoshells. Seed was mixed with KCarb-Gold and, while rapidly mixing, formaldehyde was added at 10 µl per 1 ml KCarb-Gold. This process reduces the gold and results in a contiguous gold shell over the surface of the silica particle. The characteristics of the nanoshells were determined by examining the spectral extinction profile in the range of 400-1100 nm with

a UV-Vis spectrophotometer (Cary Bio 50, Varian, Walnut Creek, CA). After analysis the nanoshells were washed for storage by centrifuging twice (750 g, 20 min) with re-suspension in 1.8 mM potassium carbonate. Before use, nanoshells were re-suspended in DI water. Transmission electron micrographs of the process of nanoshell formation have been published and are reproduced below (**Figure 2.2**) (Oldenburg *et al.* 1998).

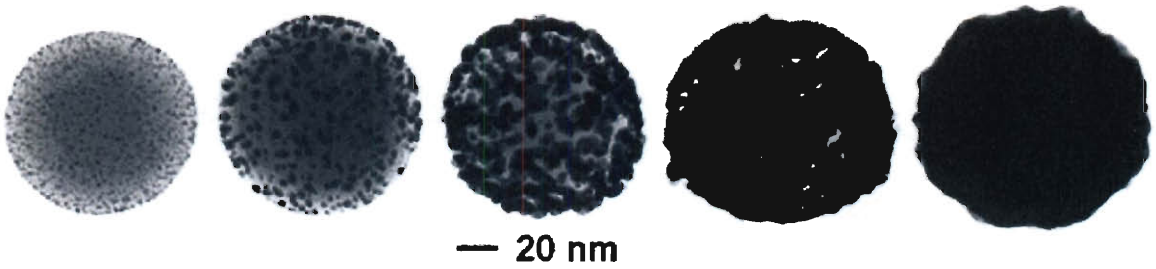

Figure 2.2: The process of shell growth on a "seed" particle. This series of transmission electron micrographs displays the shell growth process. At left an initial "seed" nanoparticle is shown. The three center images display gradual growth and coalescence of gold colloid on the silica nanoparticle. At right is a completed nanoshell. Modified from Oldenburg *et al.* 1998.

2.3 Synthesis of Gold-Gold Sulfide Nanoparticles

Gold-gold sulfide nanoparticles (GGS-NPs) were synthesized using a variation of published literature techniques (Averitt *et al.* 1999; Schwartzberg *et al.* 2007). Solutions of 2 mM $HAuCl_4$ (Alfa Aesar, Ward Hill, MA) and 1 mM $Na_2S_2O_3$ (Sigma, Saint Louis, MO) were prepared in Millipore water in amber glass vials, aged two days at room temperature, and mixed in small quantities at volumetric ratios ranging from 1:1 to 1:2 ($HAuCl_4$:$Na_2S_2O_3$). The ratio that produced nanoparticles resonant near 800 nm as determined with a UV-visible spectrophotometer (Cary 50, Varian) was used to synthesize a large batch of nanoparticles by linearly scaling the reaction volumes.

An abundance of small gold spheres, rods, and flat triangular nanoparticles existed in the initial reaction solutions as evidenced by electron microscopy and UV-

visible spectrophotometry. It was important to enrich the fraction of NIR-absorbing nanoparticles in the experimental solutions for several reasons: first, since the resonant wavelength of colloidal gold is not in the NIR, these nanoparticles do not offer diagnostic or therapeutic benefits with the approach under investigation in this thesis; second, eliminating these non-therapeutic nanoparticles allows the total nanoparticle dosage to be reduced, thereby minimizing concerns of organ toxicity; and third, elimination of these nanoparticles prevents their competitive binding to targets intended for the GGS-NPs. A multi-step centrifugation process was carried out to remove the by-product nanoparticles so that the final nanoparticle solutions used in experiments consisted of a majority of GGS-NPs. Changes in the fraction of contaminant nanoparticles and GGS-NPs were monitored by TEM and spectrophotometry, which indicated reduction in the peak near 530 nm (indicative of colloidal gold) following purification (**Figure 2.3**). After purification, GGS-NPs were evaluated for *in vitro* and *in vivo* diagnostic and therapeutic capabilities in studies that will be detailed in later chapters of this thesis.

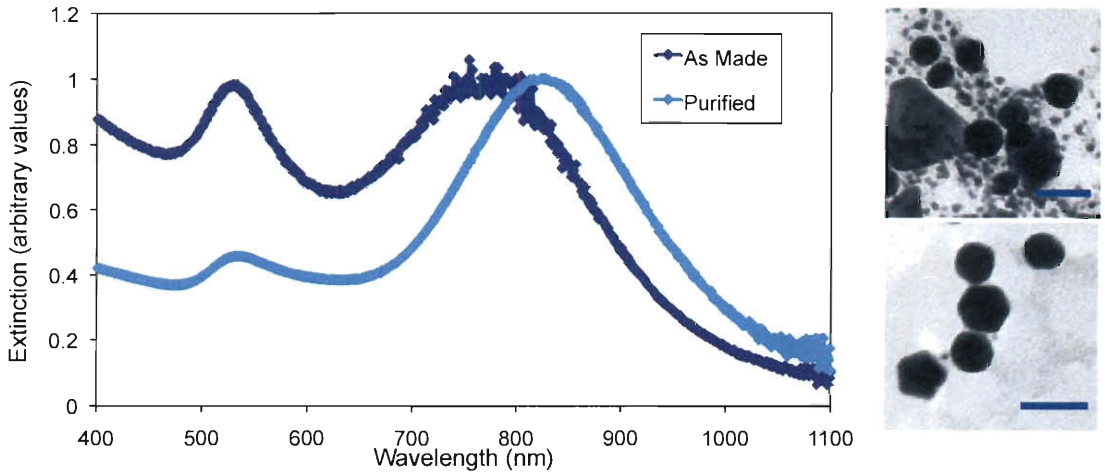

Figure 2.3: Purification of gold-gold sulfide nanoparticles. UV-visible spectroscopy shows reduction in the peak near 530 nm after centrifugation, indicating removal of small gold colloid. Transmission electron micrographs of a sample before (top right) and after (bottom right) centrifugation support this data. Scale bars = 35 nm.

2.4 Nanoparticle Stabilization with Poly(ethylene) Glycol

The addition of poly(ethylene glycol) (PEG) to nanoparticles produces a hydrophilic and flexible coating that provides steric stabilization and prevents opsonization, thereby reducing aggregate formation between nanoparticles and increasing blood circulation half-life (Wang and Thanou 2010). For the studies in this thesis, PEG coatings were formed by adding mPEG-SH (5 kDa) to nanoshells or GGS-NPs suspended in Millipore water at an optical density of 1.5. For nanoshells, 1 part 25 μM mPEG-SH was added to 9 parts nanoshells (~3 x 10^9 particles/ml), and for GGS-NPs 1 part 250 μM mPEG-SH was added to 9 parts GGS-NPs (4 x 10^{11} particles/ml); these samples reacted overnight at 4°C while rocking. mPEG-SH self-assembles on the nanoparticles due to gold-sulfur interactions. PEGylated nanoparticles were centrifuged or filtered to remove unbound molecules and suspended in the appropriate medium for the forthcoming application.

2.5 Characterization Methods

2.5.1 Electron Microscopy

Scanning electron microscopy (SEM) and transmission electron microscopy (TEM) were used to visualize bare (non-PEGylated) nanoparticles. Electron microscopy samples were prepared by drying 20 μl suspensions of nanoparticles on 300 mesh copper Gilder grids (Ted Pella, Inc., Redding, CA). SEM was performed on a FEI Quanta 400 field emission scanning electron microscope and TEM was performed on a JEOL 1230 high-contrast transmission electron microscope or a JEOL 2010 transmission electron microscope. Typical SEM images of silica-gold nanoshells (left) and unpurified gold-gold sulfide nanoparticles (right) are displayed in **Figure 2.4**.

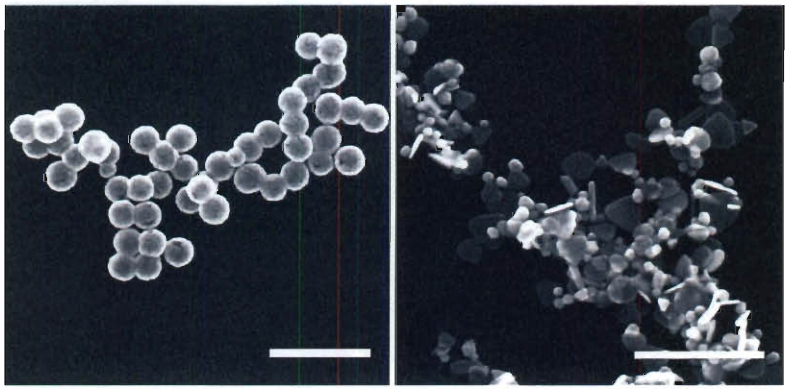

Figure 2.4: Scanning electron micrographs of nanoparticles. SEM images of nanoshells (left) and unpurified gold-gold sulfide nanoparticles (right) can be used to determine particle size and level of heterogeneity. Scale bars = 500 nm.

2.5.2 UV-Visible Spectroscopy

Nanoparticle extinction characteristics were determined by UV-visible spectroscopy with a Cary 50 Bio spectrophotometer (Varian). Red-shifts in plasmon resonance following conjugation indicated adequate PEG coverage. In addition, the quality of PEG coverage was gauged with spectroscopy by monitoring changes in extinction after mixing 900 μl nanoparticles and 100 μl 1 M NaCl. If nanoparticles were not properly stabilized, suspension in salt quickly resulted in lowered peak extinction due to formation of nanoparticle aggregates; nanoparticles were considered sufficiently stabilized if the peak extinction reduced by no more than 20% within 2 h of salt addition. Sample results from a salt stability test on nanoshells appear in **Figure 2.5**. Nanoshells coated with PEG remain in suspension after addition of salt so the optical density remains 91% of the original value; non-coated nanoshells aggregate, causing the absorbance to drop to 22% of the original value. Control nanoshells incubated with water remain suspended, with 98-99% of the initial absorbance maintained regardless of coating.

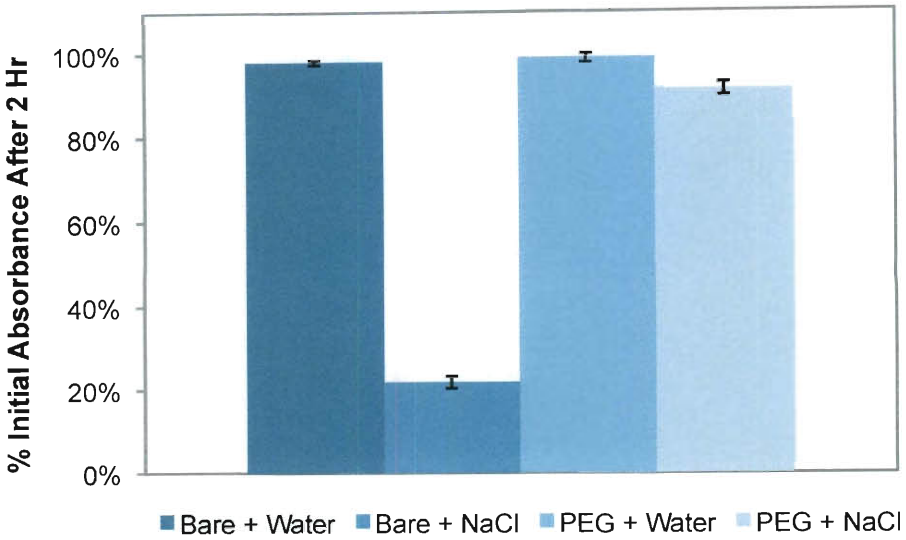

Figure 2.5: Stability of PEG-coated nanoshells in salt solution. Nanoshells coated with PEG remain stable in salt solution while bare nanoshells aggregate, leading to a drop in the absorbance over a period of 2 h.

2.5.3 Dynamic Light Scattering and Zeta Potential Analysis

Dynamic light scattering (DLS) and Zeta potential measurements were performed on a ZetaSizer NanoZS (Malvern Instruments, Worcestershire, UK) to confirm PEG coverage. DLS measures Brownian motion of nanoparticles in solution to estimate particle hydrodynamic diameter; larger nanoparticles display slower Brownian motion. Translational diffusion depends not only on particle size, but also on surface structure, so adding polymer coatings increases the hydrodynamic diameter. Hence, upon adequate PEG conjugation, nanoparticles should demonstrate increased hydrodynamic diameter.

When a charged nanoparticle is placed in suspension, oppositely charged ions are attracted to the surface of the nanoparticle to form an electric double layer; ions closer to the nanoparticle are strongly bound while ions further from the surface are loosely bound. The edge of this loosely bound layer is known as the slipping plane, and ions within that boundary move with the particle as it moves in liquid. Zeta potential is the potential at

the slipping plane, and its magnitude indicates the stability of the colloidal system. As PEG is added to nanoparticles the zeta potential neutralizes since the polymer chains increase the distance of the slipping plane from the nanoparticle surface and reduce the nanoparticle mobility. Therefore, observing decreases in Zeta potential magnitude can be used as a quality control step to confirm sufficient coating. Sample DLS and Zeta potential measurements for nanoshells used in this thesis are demonstrated in **Figure 2.6.**

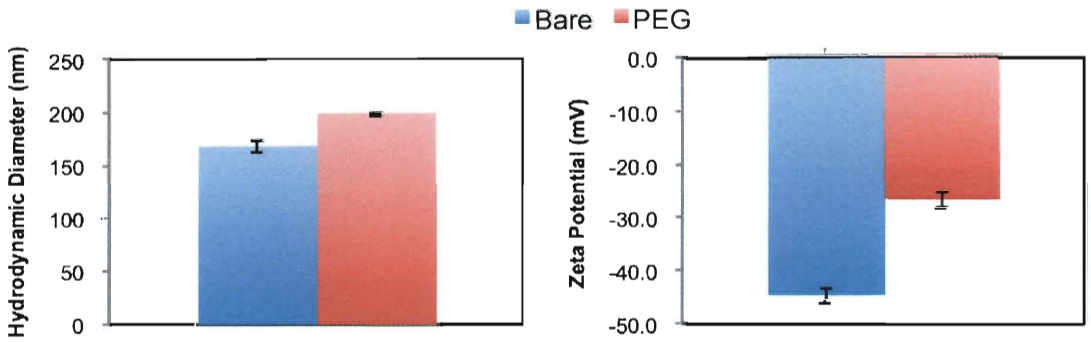

Figure 2.6: Hydrodynamic diameter and Zeta potential of bare and PEG-coated nanoshells. (Left) Hydrodynamic diameter of nanoshells increases by 30 nm upon addition of mPEG-SH. (Right) Zeta potential increases by 20 mV upon addition of mPEG-SH.

2.6 Conclusions

The methods in this chapter describe the synthesis and PEG passivation of nanoshells and gold-gold sulfide nanoparticles. The techniques used to characterize nanoparticles introduced here were used throughout the remainder of this thesis to ensure nanoparticle quality prior to use in experiments.

Chapter 3: Antibody-Coated Nanoshells for Enhanced Cancer Diagnosis and Therapy

3.1 Introduction

In the process of tumorigenesis, genetic alterations within cancer cells often induce up-regulation of cell surface receptors. These over-expressed receptors are known as "molecular markers" that distinguish diseased tissue from normal tissue, and they provide a potential binding site for novel therapeutics. Molecularly-targeted therapeutics may improve cancer therapy by enhancing specificity, prolonging retention within tumors, and minimizing off-target effects. In this chapter, the addition of antibodies to nanoshell surfaces is evaluated as a means of providing tumor cell-specific targeting and enhanced photothermal therapy *in vitro*. In addition, the diagnostic potential of anti-HER2 nanoshells is evaluated with *ex vivo* tumor samples.

3.1.1 Passive versus Active Targeting of Tumors

Nanoparticle accumulation within tumors can be accomplished through "passive" or "active" targeting. In passive targeting, nanoparticles' small size allows them to exploit tumors' leaky vasculature and poor lymphatic drainage, which promote increased extravasation and longer retention in the tumor interstitial space, respectively; this phenomenon is known as the enhanced permeability and retention (EPR) effect (Matsumura and Maeda 1986). While passive targeting can be effective, it is limited by the fact that the size and number of fenestrations within tumor vasculature varies widely; as a result, nanoparticles cannot be delivered to tumors with much precision.

The recent discovery of cancer cell biomarkers initiated a new thrust in the development of nanoparticle delivery mechanisms; scientists are now utilizing active targeting schemes that direct nanoparticles toward specific cell populations within a tumor by functionalizing the particles with moieties known to bind tumor cell antigens. For active targeting to be beneficial, it is imperative that the targeting ligand of choice is selective for antigens uniquely over-expressed by cancerous cells relative to normal cells. One advantage of active targeting is that when targeted nanoparticles bind cancer cells, it may prolong retention within the tumor compared to passive accumulation. In addition, active targeting may increase therapeutic efficacy by promoting cellular internalization of the nanoparticle and any drugs or imaging agents it may be ferrying. The differences between active and passive targeting are summarized visually in **Figure 3.1** (Dong and Mumper 2010).

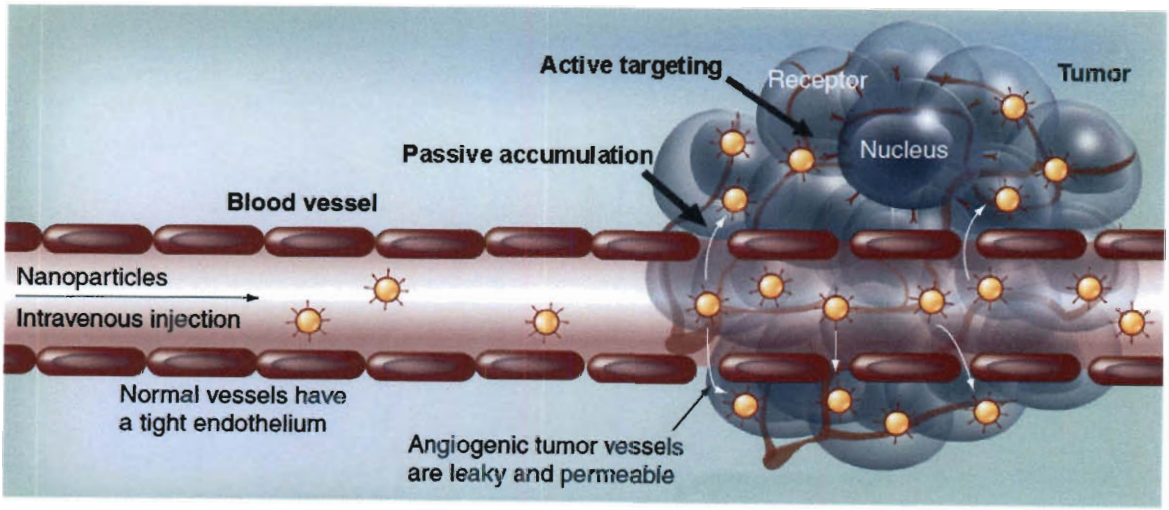

Figure 3.1: Passive and active tumor targeting. Nanoparticles passively accumulate in tumors via the EPR effect since tumors exhibit leaky vasculature and poor lymphatic drainage. In active targeting, conjugated ligands facilitate nanoparticle binding to tumor cell antigens; this binding prolongs nanoparticle retention in the tumor and promotes receptor-mediated endocytosis. Modified from Dong and Mumper (2010).

One biomarker that has been extensively studied as a potential target is human epidermal growth factor receptor 2 (HER2), which was first identified as being amplified in up to 30% of breast cancer cases (Slamon *et al.* 1987). It is now known that HER2 is up-regulated in many human tumors, including medulloblastoma, ovarian, lung, gastric, and oral tumors, and that its over-expression correlates with a poorer clinical prognosis (Hung *et al.* 1995). HER2 has no known ligands, but it dimerizes with other HER family receptors to induce intracellular phosphorylation that provides binding sites for molecules that activate pro-tumorigenic signaling cascades, such as the MAPK proliferation pathway and the PI3K/Akt pro-survival pathway (Menard *et al.* 2003). In the next section, different methods of targeting receptors such as HER2 will be introduced.

3.1.2 Targeting Schemes: Antibodies, Peptides, and Aptamers

Several types of bioactive molecules are being investigated for active targeting, including antibodies, peptides, and aptamers. Each of these will be discussed here in brief, with focus on moieties specific for HER2; for a more thorough discussion, several excellent reviews exist in the literature (Peer *et al.* 2007; Huynh *et al.* 2010; Ruoslahti *et al.* 2010).

Antibodies are the most commonly used targeting agents, with over 200 delivery systems based on antibodies and their fragments currently in development (Peer *et al.* 2007). The first antibody therapy targeted towards HER2, Trastuzumab (Herceptin), was approved for treatment of breast cancer in 1998 (Albanell and Baselga 1999). More recently, anti-HER2 conjugated liposomes have demonstrated successful delivery of paclitaxel (Yang *et al.* 2007) and doxorubicin (Park *et al.* 2002; Kirpotin *et al.* 2006) in preclinical models. While some therapies utilize whole antibodies, others utilize antibody fragments. Whole monoclonal antibodies are advantageous because they offer

two binding sites per molecule, yielding higher binding affinity. However, the Fc portion on whole antibodies can bind Fc receptors on normal cells such as macrophages, leading to increased immunogenicity and clearance to the liver and spleen (Peer *et al.* 2007). To avoid this problem, antibody fragments that lack the Fc portion can be utilized, but these are less stable than their whole antibody counterparts.

Some non-antibody targeting agents currently in development include growth factors (such as EGF or VEGF), vitamins (such as folic acid), and peptides (such as RGD, the ligand of the cell adhesion molecule $\alpha_v\beta_3$ that is up-regulated on tumor vessels, and Lyp-1, the ligand for the p32 receptor that is up-regulated on tumor cells undergoing stress) (Murphy *et al.* 2008; Park *et al.* 2010). Recently, a bi-functional peptide was developed that is capable of both neutralizing HER2 and delivering a toxin to disable mitochondrial function in HER2-positive tumors; this molecule is called BHAP, for bi-functional HER2-blocking and apoptosis-inducing peptide (Fantin *et al.* 2005).

The third class of targeting molecules to be discussed here are aptamers—short single-stranded DNA or RNA oligonucleotides that fold into well-defined structures that bind to their ligand by complimentary shape interactions (Blank and Blind 2005). These ligands are selected *in vitro* from large libraries of random sequences. A peptide aptamer against HER2 was recently developed and found to sensitize breast cancer cells to taxol (Kunz *et al.* 2006). While aptamers offer the benefits of having high affinity and no intrinsic toxicity or immunogenicity (Blank and Blind 2005), they are expensive to produce which minimizes their current utility.

This chapter evaluated antibody coatings as a means of enhancing tumor cell targeting of nanoshells since antibodies are the most widely accepted targeting technique

and have already achieved FDA approval. Nanoshells were coated with antibodies against HER2 and binding affinity was evaluated both *in vitro* and *ex vivo*. Anti-HER2 nanoshells selectively targeted HER2-positive cancerous cells and facilitated thermal ablation *in vitro* in both monoculture and co-culture experiments. The targeting ability of anti-HER2 nanoshells was further demonstrated through *ex vivo* binding to ovarian tumor tissue specimens; the degree of nanoshell binding correlated with HER2 expression. Together, these results imply that anti-HER2 nanoshells could be used clinically in the future to ascertain from biopsy specimens whether a patient might benefit from anti-HER2 targeted photothermal therapy; however, *in vivo* distribution and efficacy of anti-HER2 coated nanoshells remain to be evaluated in future studies.

3.2 Materials and Methods

3.2.1 Preparation of PEG-Antibody Conjugates

Heterobifunctional poly(ethylene glycol) (PEG) was employed as a linker to coat nanoshells with antibodies. Specifically, the linker was 2 kDa orthopyridyl-disulfide-poly(ethylene glycol)-N-hydroxysuccinimide (OPSS-PEG-NHS, Nektar, San Carlos, CA); this molecule has known biocompatibility and improves antibody mobility on the particle surface. OPSS-PEG-NHS was conjugated to anti-HER2 antibodies (NeoMarkers, Fremont, CA) by mixing 1 part 81 μM OPSS-PEG-NHS with 9 parts 1 mg/ml anti-HER2 at 4°C overnight. As shown schematically in **Figure 3.2** the NHS terminus is cleaved during this reaction and a stable amide bond is produced between primary amines on the antibody and carboxyl groups on the PEG chain.

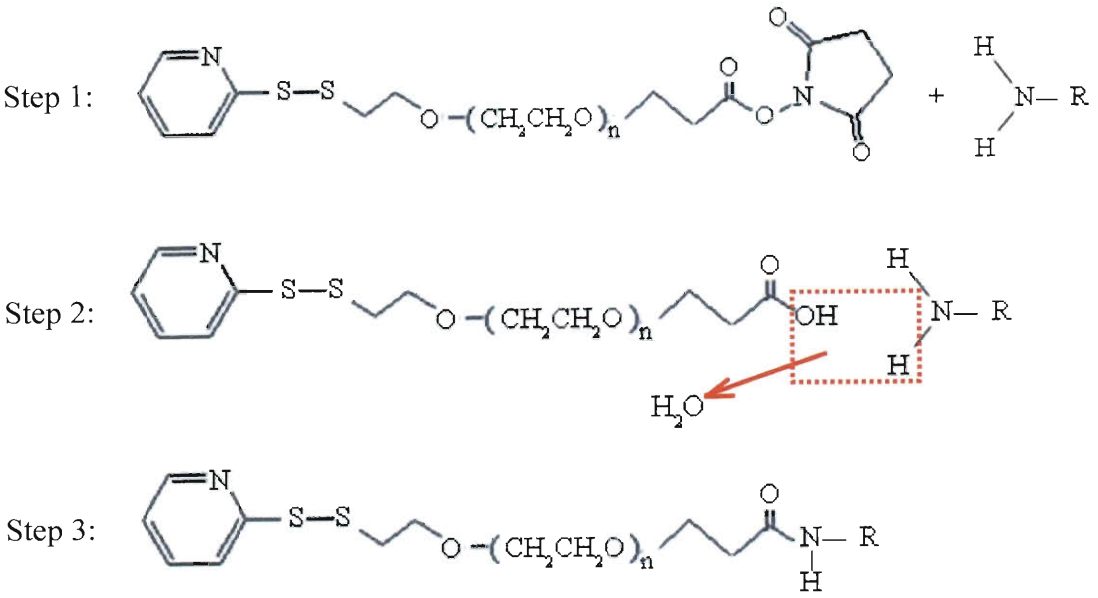

Figure 3.2: Preparation of PEG-antibody conjugates. This representation shows an antibody (R) with an available primary amine binding to OPSS-PEG-NHS in a basic solution. First the NHS group is cleaved in water and then an amide bond forms at the carboxylic terminus. At the end of the reaction the antibody is covalently attached to the PEG molecule.

3.2.2 Attachment of Targeting Agents to Nanoshells and Quantification of Antibody Coverage with the Enzyme-Linked Immunosorbent Assay

Nanoshells suspended in milli-Q water at an optical density (OD) of 1.5 were exposed to OPSS-PEG-anti-HER2 for 1 h at 4°C at a 1500:1 molar ratio. Next, samples reacted in 5 μM mPEG-SH (5 kDa, Laysan Bio, Inc., Arab, AL) overnight at 4°C to passivate any exposed gold surface area. Nanoshells coated with mPEG-SH only (no antibody) were also synthesized for use as a negative control. Following antibody and/or PEG modification, nanoshells were centrifuged to remove unbound molecules, aspirated, and suspended in the appropriate medium for the prospective application.

To quantify the number of antibodies on the nanoshells, a modified enzyme-linked immunosorbent assay (ELISA) was utilized. Targeted (coated with PEG-anti-HER2 and mPEG-SH) and control (only mPEG-SH coated) nanoshells incubated with

10 μg/ml horseradish peroxidase (HRP)-labeled goat anti-mouse IgG (Sigma). Nonspecific reaction sites were blocked with 3% bovine serum albumin (BSA, Sigma) in PBS. To remove unbound HRP-labeled antibodies, nanoshells were centrifuged twice at 500 g for 5 min and suspended in 3% BSA. Bound HRP was developed with 3,3',5,5'-tetramethylbenzidine dihydrochloride (TMB, Sigma) for 15 min and the reaction stopped by addition of 2 M sulfuric acid. Developed HRP was compared to a standard curve of the appropriate HRP-labeled anti-IgG by measuring the absorbance at 450 nm. The number of antibodies per nanoparticle was calculated by dividing the number of peroxidase-labeled anti-IgG moieties by the number of nanoshells in solution.

3.2.3 *In Vitro* Binding of Anti-HER2-Coated Nanoshells to Targeted Breast Carcinoma Cells and Subsequent Photothermal Therapy

To demonstrate that antibody targeting yields enhanced nanoshell binding to cell surface receptors, anti-HER2 nanoshells and PEG nanoshells were incubated with SK-BR-3 breast carcinoma cells, which over-express the HER2 receptor (Kraus *et al.* 1987). SK-BR-3 cells were cultured in McCoy's 5A Medium (Sigma) containing 10% fetal bovine serum and 1% penicillin-streptomycin at 37°C in a 5% CO_2 environment and incubated for 1 hour with 5×10^9 anti-HER2 nanoshells or PEG nanoshells (both suspended in McCoy's 5A). Rinsing with PBS removed unbound particles and treatment with 2.5% gluteraldehyde fixed the cells. Staining with Amersham Silver Enhancer, which deposits silver onto the gold surface, allowed visualization of nanoshells via light microscopy.

Following the binding assay, a second experiment tested whether the degree of anti-HER2 nanoshell binding to cells was sufficient for photothermal ablation. SK-BR-3 cells were again cultured and exposed to anti-HER2 nanoshells or PEG nanoshells for 1 h

prior to rinsing thrice with PBS. Samples were covered with McCoy's 5A Medium and irradiated with an 808 nm laser (Coherent, Inc., Santa Clara, CA) at 88 W/cm^2 for 7 min. After incubating 2 h at 37°C, cell viability was assessed by labeling with calcein AM (1 μM, Molecular Probes, Eugene, OR), a live cell stain, and ethidium homodimer-1 (4 μM, Molecular Probes), a dead cell stain. Fluorescence microscopy was performed with an inverted Zeiss Axiovert 135 microscope (Carl Zeiss) to determine viability.

3.2.4 *In Vitro* Destruction of Targeted Breast Carcinoma Cells in Co-Culture with Non-Targeted Endothelial Cells

To prove specificity of antibody targeting, photothermal therapy of cancerous cells that over-express HER2 placed side-by-side with healthy cells exhibiting normal HER2 expression was attempted. SK-BR-3 (HER2+) and Human Umbilical Vein Endothelial Cells (HUVECs) were cultured separately on cover slips coated with 1% gelatin and placed adjacently in a 1-well culture slide with no gap between the slips. The samples were incubated with anti-HER2 nanoshells or with PEG nanoshells for 1 h prior to rinsing and laser treatment at the interface of the coverslips (88 W/cm^2, 7 min). Samples incubated at 37°C overnight prior to examination of viability with a fluorescent live/dead stain as described above.

Differences in receptor expression between the two cell types were confirmed with immunohistochemistry. Cultured SK-BR-3 cells and HUVECs were fixed in 10% formalin for 10 min, rinsed with PBS, and endogenous peroxidase activity was blocked with 5 min treatment in 3% H_2O_2 in PBS. To block nonspecific sites, cells incubated with 3% BSA in PBS for 90 min; next, 300 μl mouse anti-human HER2 antibody (5 μg/ml, Lab Vision) was added to the wells. After 1 h, cells were rinsed 3 times with

PBS. The HRP-conjugated secondary antibody (2 μg/ml, Sigma) was then added to each well for 40 min. After three changes of PBS, samples were developed with AEC (3-amino-9-ethylcarbazole) to produce a red stain indicative of HER2 presence.

3.2.5 *Ex Vivo* Binding of Immunonanoshells to Ovarian Tumor Tissue with Varying Target Receptor Expression

Lastly, to prove that anti-HER2 nanoshells could be utilized in a diagnostic setting to guide treatment decisions, ovarian tumor tissue with varying HER2 expression was exposed to anti-HER2 nanoshells and PEG nanoshells *ex vivo*. Frozen sections (30 μm thickness) of tumors grown in mice were received from Dr. Anil Sood's lab at MD Anderson Cancer Center. The three ovarian tumor types studied were SKOV3ip1, HeyA8, and A2780-PAR, listed in order of decreasing HER2 expression according to literature review (Marth *et al.* 1992; Lewis *et al.* 1993; Peles *et al.* 1993; Yu *et al.* 1993). Sections were brought to room temperature and a hydrophobic barrier was drawn around the tissue. Samples incubated in PBS for 5 min and were blocked with 3% BSA in PBS for 2 h prior to incubation with anti-HER2 nanoshells or PEG nanoshells for 1 h at room temperature. After rinsing three times with PBS, samples were mounted and imaged via darkfield microscopy using a CytoViva adaptor coupled to an Axiovert 135 microscope (Carl Zeiss). With this technique, images are produced from light scattered by the samples and nanoshells are easily detected since they have superior scattering compared to tissue components (Loo *et al.* 2005; Loo *et al.* 2005; Gobin *et al.* 2008).

3.3 Results and Discussion

3.3.1 Quantification of Antibodies on Nanoshells

Antibody quantification with the modified ELISA confirmed that anti-HER2-coated nanoshells bound significantly more HRP-antibodies than PEG-coated nanoshells ($p=0.01$, student's t-test). The ELISA indicated ~300 antibodies per anti-HER2-coated nanoshell, while control PEG-coated nanoshells remained free of antibody (25 ± 29 antibodies/nanoparticle).

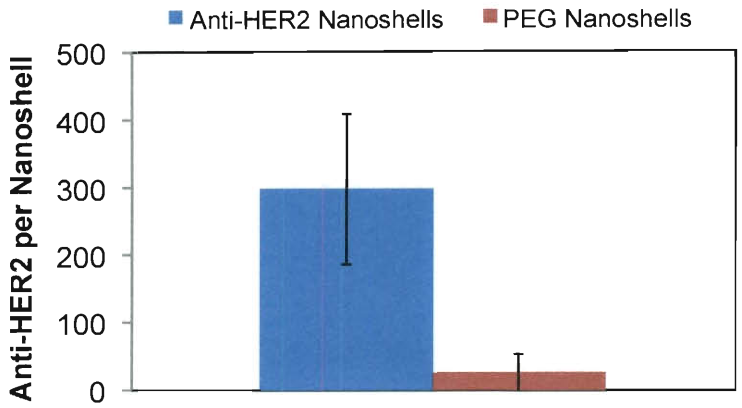

Figure 3.3: Quantification of anti-HER2 antibody coverage on nanoshells. Number of anti-HER2 antibodies bound per nanoshell determined by the modified ELISA. Antibody-free controls show minimal background signal.

3.3.2 Antibody-Coated Nanoshells Bind to Targeted Cancer Cells and Facilitate Thermal Ablation

Silver enhancement confirmed that anti-HER2 nanoshells were able to bind the HER2-expressing SK-BR-3 cells (**Figure 3.4**). By comparison, PEG nanoshells showed minimal staining, demonstrating the ability of PEG to prevent non-specific adsorption. Cells that did not receive nanoshells also showed minimal staining.

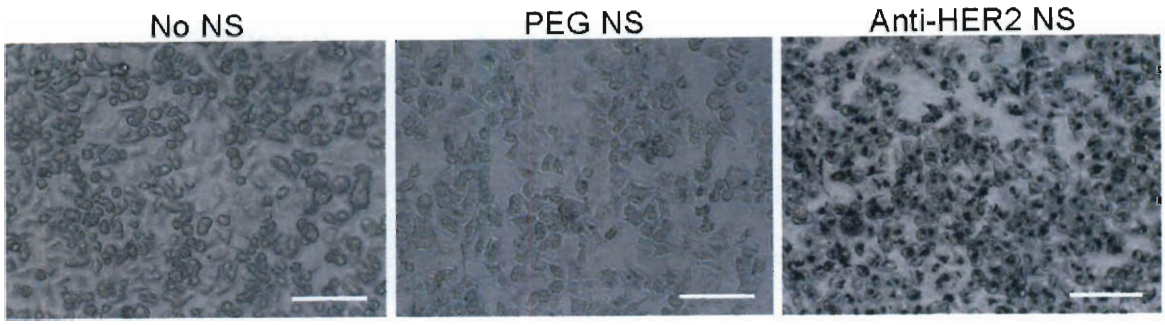

Figure 3.4: Anti-HER2 nanoshells bind HER2-positive cells. A high degree of silver staining provided evidence that anti-HER2 nanoshells bound to HER2-positive SK-BR-3 cells, while minimal staining was observed on cells that incubated with PEG nanoshells or saline. Scale bar = 100 μm.

Figure 3.5 shows the results of the viability assay performed after laser irradiation on SK-BR-3 cells grown in monoculture and exposed to different nanoparticle solutions. Cells receiving laser irradiation after incubation with saline or PEG-coated nanoshells remain viable, as demonstrated by the green calcein AM fluorescence. In contrast, cells that were exposed to anti-HER2 nanoshells display a circular region of death (red, EthD-1) where the laser was applied. In these targeted samples, a sufficient number of nanoshells bound to the cells in order to produce heat capable of inducing irreversible membrane damage.

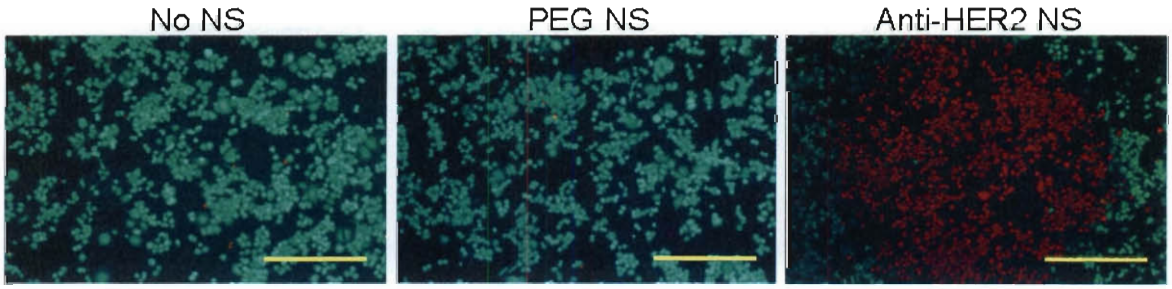

Figure 3.5: Targeted nanoshells mediate photothermal ablation of cancer cells. Calcein AM staining indicated that cancerous cells remained viable (evidenced by green fluorescent signal) when exposed to saline or PEG nanoshells prior to laser irradiation. When SK-BR-3 cells were incubated with anti-HER2 nanoshells and exposed to the laser, a red fluorescent EthD-1 signal indicative of cell membrane damage was observed in the region where the laser was applied. Scale bar = 500 μm.

3.3.3 Antibody-Coated Nanoshells Enable Specific Targeted Ablation of Cancerous Cells in Co-Culture with Endothelial Cells

Attempting photothermal therapy of cancerous cells that over-express HER2 placed side-by-side with healthy cells exhibiting lower HER2 expression proved specificity of antibody targeting. Expression of HER2 on SK-BR-3 cells but not HUVECs was confirmed with immunohistochemistry (**Figure 3.6**). HUVECs and SK-BR-3 cells grown on coverglass and placed adjacently were exposed to the same particles and laser parameters, and then a viability assay was performed. In **Figure 3.7**, when HUVECs (top half of each image) and SK-BR-3 cells (bottom half of each image) were exposed to PEG nanoshells, which do not bind cells, both cell types remained alive post-laser treatment (evidenced by green calcein AM fluorescence). When these cells were exposed to anti-HER2 nanoshells, only the targeted SK-BR-3 cells within the laser spot were destroyed while the proximal HUVECs remained unharmed. Cells of each type outside the laser path remained viable, proving that photothermal therapy requires a balanced dose of nanoparticles and laser energy.

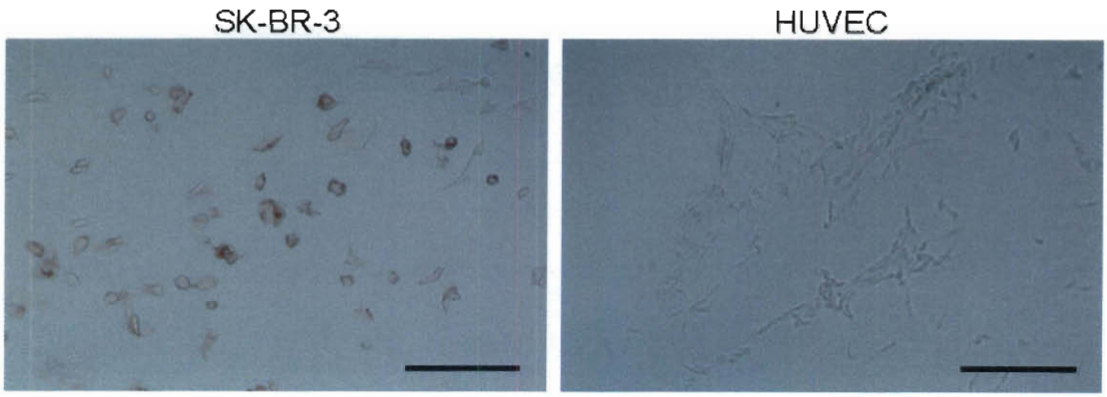

Figure 3.6: HER2 expression status in two cell lines. Immunohistochemistry revealed that SK-BR-3 cells over-express HER2, shown by red HRP/AEC staining, while HUVECs do not. Thus, these cell lines are useful for determining the specificity of anti-HER2 coated nanoshells. Scale bar = 200 μm.

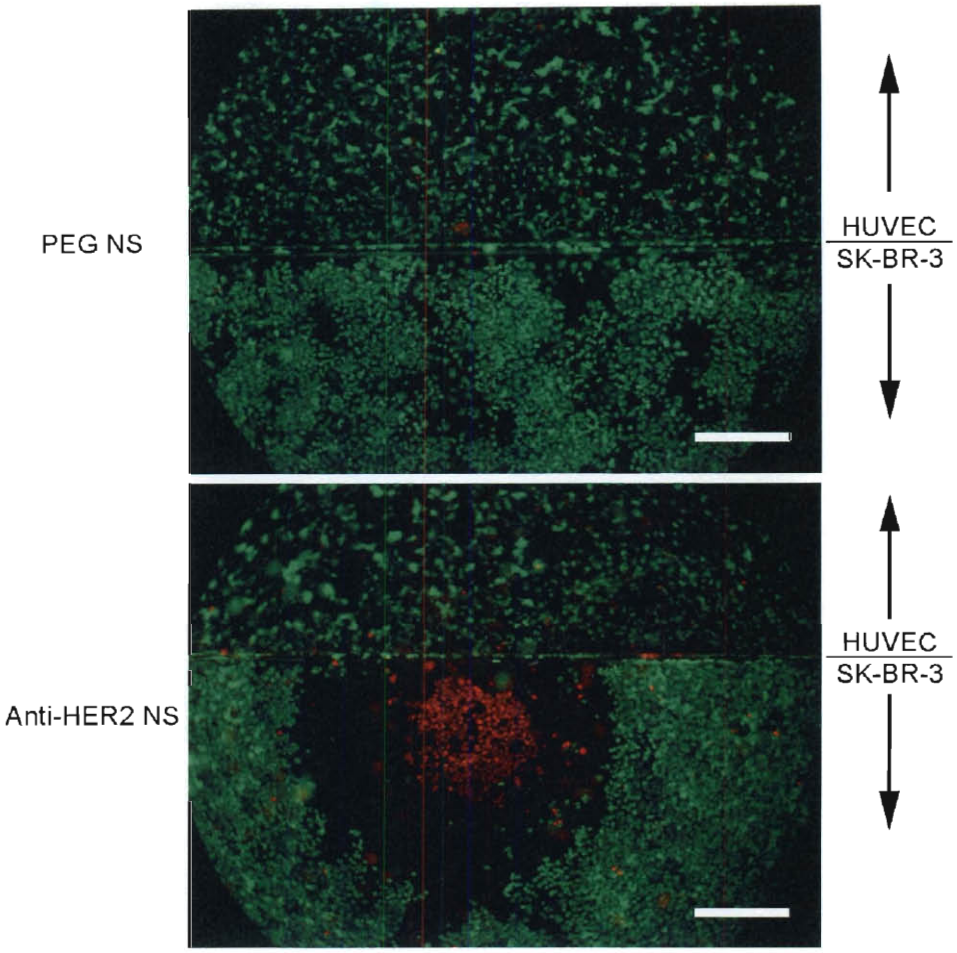

Figure 3.7: Targeted nanoshells provide cell type-specific photothermal therapy. HUVECs and SK-BR-3 cells grown on coverslips and placed adjacently were exposed to either PEG nanoshells (top image) or anti-HER2 nanoshells (bottom image) prior to laser irradiation at the interface of the slips. (Top): Since PEG nanoshells do not bind cells, both cell types remained viable after laser exposure, indicated by green calcein AM fluorescence. (Bottom): Anti-HER2 nanoshells bound the HER2-expressing SK-BR-3 cells but not the HUVECs, so only SK-BR-3 cells experienced loss in viability after laser treatment, shown by red ethidium homodimer-1 fluorescence. Scale bar = 500 μm.

3.3.4 Anti-HER2 Nanoshells Bind Tumor Tissue *Ex Vivo* to Indicate Relative Target Receptor Expression

While the above *in vitro* studies confirmed the ability of anti-HER2 nanoshells to bind HER2-positive cells grown in culture, it remained unknown whether this ability would be maintained when the nanoparticles were exposed to complex tissue architectures. To

answer this question, anti-HER2 and PEG-coated nanoshells were incubated with ovarian tumor tissue specimens having varied receptor expression, and samples were imaged with darkfield microscopy. As shown in **Figure 3.8**, the anti-HER2 nanoshells bound tumor tissue at levels corresponding to the HER2 expression, while the PEG nanoshells showed minimal binding to each tumor type. Thus, there is good correlation between the ability of targeted nanoshells to bind receptors both *in vitro* and *ex vivo*.

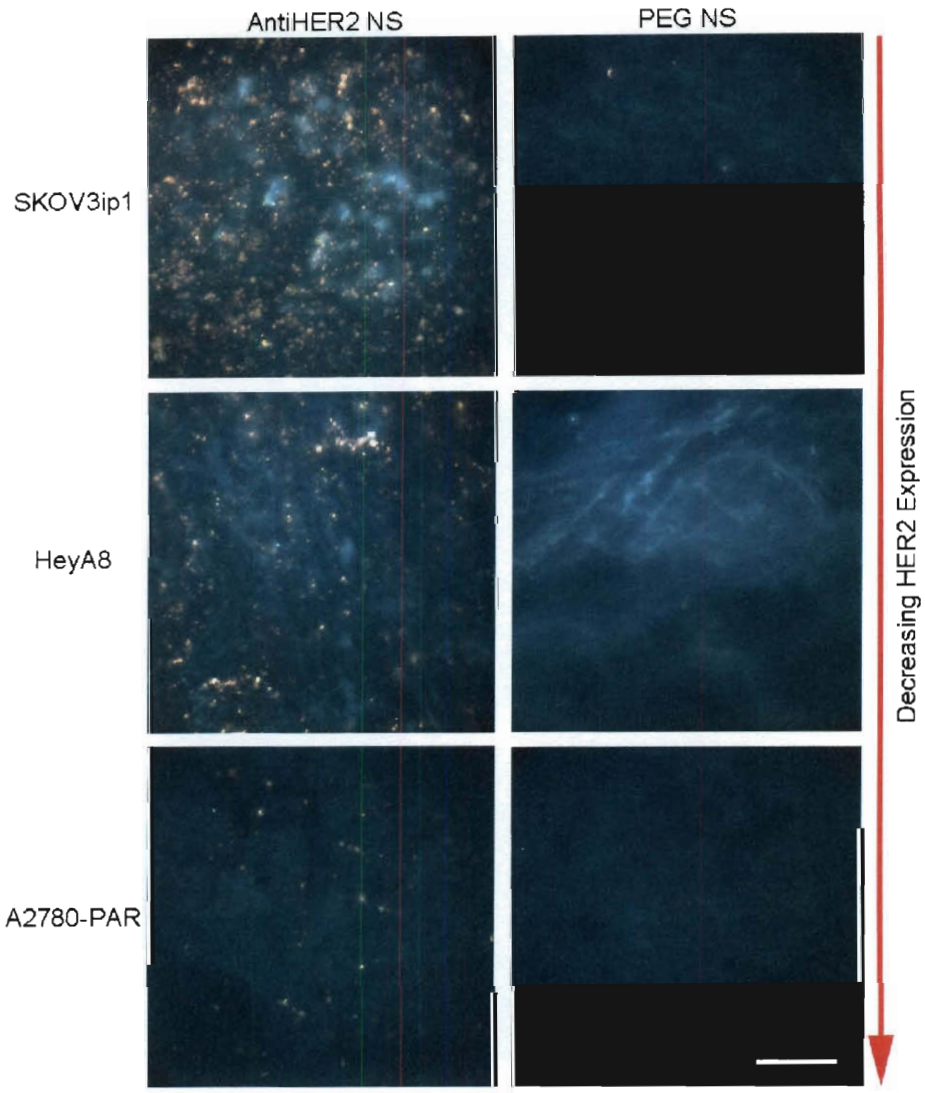

Figure 3.8: Darkfield microscopy of nanoshell binding to ovarian tumor tissue *ex vivo*. Nanoshells appear golden red against the bluish tissue background and the degree of anti-HER2 nanoshell binding correlates with tissue HER2 expression. PEG nanoshells do not bind the tumor tissue. Scale bar = 50 μm.

3.3.5 Discussion

Molecular targeting has emerged as a promising new tool in the fight against cancer and this chapter aimed to demonstrate enhancement of photothermal cancer therapy through targeted delivery of nanoshells. Previous *in vivo* studies have relied on the EPR effect to deliver nanoshells to tumors (O'Neal *et al.* 2004); it is predicted that antibody targeting may enhance the accumulation of nanoshells in tumors, allowing the use of lower nanoshell or laser dosages.

As demonstrated by the modified ELISA, the OPSS-PEG-NHS linker was able to bind a significant number of antibodies to the nanoshell surface. The density of ~300 anti-HER2 antibodies per nanoshell greatly exceeded the reported density of 30-50 antibodies on liposomes of similar size (Park *et al.* 2002), so nanoshells should demonstrate greater binding affinity. Silver staining confirmed that antibody-coated nanoshells bound HER2-positive SK-BR-3 breast carcinoma cells at high levels and a viability assay proved that these targeted nanoshells enabled thermal ablation upon exposure to a near-infrared laser. PEG nanoshells, which do not bind cell surface receptors, were rinsed away during washing thus preventing cell death after NIR irradiation.

The specificity of antibody targeting was demonstrated in a co-culture experiment in which HER2-negative HUVECs and HER2-positive SK-BR-3 cells were placed side-by-side prior to incubation with the nanoshells and subsequent laser treatment. The anti-HER2 nanoshells bound only the SK-BR-3 cells, so only these targeted cells died when the laser was applied. When co-cultured cells were incubated with PEG nanoshells, neither cell type lost viability following therapy. In a similar experiment, anti-HER2

nanoshells' specificity was confirmed by treating SK-BR-3 in co-culture with human dermal fibroblasts (HDFs); these data were recently published (Lowery *et al.* 2006). These *in vitro* results demonstrate the ability of nanoshell-mediated photothermal therapy to provide extremely localized and specific cancer therapy, which should minimize side effects when translated *in vivo*.

Lastly, the ability of anti-HER2 nanoshells to bind targeted receptors in a more complex tissue environment was demonstrated. Anti-HER2-coated nanoshells exposed to ovarian tumor tissue with relatively high or low levels of HER2 expression bound to the specimens at corresponding frequencies, while PEG-coated nanoshells did not bind the tumor specimens. This agrees with the results of Bickford *et al.*, who demonstrated that anti-HER2 nanoshells could bind to HER2-positive human breast tumor specimens *ex vivo* but not to HER2-negative tumor specimens or to healthy tissue (Bickford *et al.* 2010). In the future, biopsy specimens could be exposed to anti-HER2 nanoshells to determine a patient's receptor level status and guide decisions regarding treatment. By evaluating receptor status *ex vivo*, it could be possible to predict whether a patient would benefit from anti-HER2 targeted photothermal therapy.

3.4 Conclusions

In conclusion, these results support the hypothesis that antibody targeting may provide a means of enhancing nanoshell-mediated photothermal therapy. Targeted nanoshells specifically bind cancerous cells that over-express the desired receptor, even when in close proximity to cells with normal HER2 expression. The ability of antibody-coated nanoshells to bind a variety of tumor cell types has now been demonstrated *in vitro*; this includes breast (Loo *et al.* 2005; Lowery *et al.* 2006), medulloblastoma (Bernardi *et al.*

2008), and glioma cell lines (Bernardi *et al.* 2008). Recently, some exciting new data has established that photothermal therapy with anti-HER2 nanoshells is effective even against Trastuzumab-resistant breast cancer cells *in vitro* (Carpin *et al.* 2011); thus, anti-HER2 nanoshell photothermal therapy may be an appropriate alternative for patients whose tumors have failed to respond to prior immunotherapy.

While the results of *in vitro* targeting studies are positive, antibody targeting of these nanoparticles remains to be validated *in vivo*; this will be a major focus of the second half of this thesis. In Chapter 4, it will be shown that the same conjugation chemistry used to functionalize nanoshells may also be used to functionalize gold-gold sulfide nanoparticles. Then, in Chapter 5, the ability of antibody-targeted nanoshells and gold-gold sulfide nanoparticles to reach subcutaneous glioma tumors in the complex biological milieu will be examined and compared to the distribution and tumor uptake of PEG-coated nanoparticles. Ultimately, it will be important to test multiple tumor types and targeting schemes *in vivo* to determine the best molecular markers and nanoparticle formulations for effective photothermal therapy.

Chapter 4: Gold-Gold Sulfide Nanoparticles as Multifunctional Agents for Imaging and Therapy of Cancer

4.1 Introduction

Researchers have recently begun to engineer nanoparticles with properties suitable for integrated imaging and therapy of cancer in an effort to better manage the disease (Ferrari 2005). The advantage of these technologies lies in the possibility to "see and treat" tumors in a single setting, which is anticipated to reduce the cost of patient care and to improve personalized medicine. This chapter introduces gold-gold sulfide nanoparticles (GGS-NPs) as multifunctional agents for targeted imaging and therapy of cancer via multiphoton microscopy followed by higher intensity photoablation. This "theranostic" approach would be ideal for pinpointing precise treatment sites following initial tumor detection with wide-field imaging modalities. Much of this work was published in: Day ES *et al.* "Antibody-conjugated gold-gold sulfide nanoparticles as multifunctional agents for imaging and therapy of breast cancer." Int J Nanomedicine (2010); 5: 445-454.

4.1.1 Nanoparticle Theranostics

Theranostic nanoparticles are defined by the ability to simultaneously deliver imaging and therapeutic functions (Xie *et al.* 2010). Two main classes of nanoparticle theranostics exist: the first uses imaging to track therapeutic delivery, while the second uses imaging to guide subsequent on-demand, site-specific therapy. Here, a few examples from each class will be discussed to demonstrate the advantages of nanoparticle theranostics and to indicate where improvements can be made.

Image-guided drug delivery (IGDD) is an important concept in medical oncology because it may help clinicians optimize local delivery of therapeutics or gather feedback of treatment response. One IGDD method encapsulates contrast agents and drugs within polymeric or liposomal nanoparticles and has been shown not only to enable *in vivo* monitoring but also to improve therapeutic efficacy. For instance, Murphy *et al.* visualized real-time delivery of doxorubicin to tumor vessels with intravital microscopy by co-encapulating the cytotoxic drug in small unilamellar vesicles (SUVs) with the fluorophore BODIPY; these SUVs reduced tumor growth and inhibited metastasis of two orthotopic tumor models with 15 times less doxorubicin than required for free drug delivery (Murphy *et al.* 2008). This improvement was significant given that chemotherapy is often dose-limited due to systemic toxicity. Unfortunately, one drawback of this technique is that fluorophores are susceptible to photobleaching. To circumvent this limitation the fluorophore could be replaced with small nanoparticle contrast agents. For example, iron-oxide nanoparticles (IONPs) have been placed within larger polyacrylamide nanoparticles (Reddy *et al.* 2006) or micelles (Nasongkla *et al.* 2006) to provide contrast for magnetic resonance imaging (MRI), one of the most common diagnostic techniques employed in cancer.

A second approach to IGDD involves covalent attachment of therapeutic agents to a nanoparticle contrast agent. This approach was elegantly demonstrated using IONPs for gene therapy: researchers predicted that conjugating silencing RNA (siRNA) to IONPs would reduce the rate of degradation by RNases *in vivo*, a major barrier to clinical translation (Medarova *et al.* 2007). In a landmark study, Moore and colleagues demonstrated that dextran-coated IONPs coupled to siRNA against Birc5 (an anti-

apoptotic gene encoding the protein survivin) dramatically reduced survivin expression in human colon adenocarcinoma xenografts (Medarova *et al.* 2007). Additionally, the IONPs were linked to the NIR dye Cy5.5, allowing distribution to be monitored with both optical microscopy and MRI. More recently, a peptide targeting the tumor antigen uMUC-1 has been added to the conjugate in an attempt to improve tumor accumulation and enable image-guided delivery of siRNA to breast adenocarcinoma xenografts (Kumar *et al.* 2010). This approach exemplifies the potential of theranostic nanoparticles to provide multiple functionalities (imaging, therapy, targeting) and to improve therapeutic efficacy compared to free delivery.

Although several groups have employed nanoparticles as cargo-carriers with some success, controlled release of cargo has yet to be gained, so risk remains for non-specific delivery. To eliminate this risk of burst drug release at undesired locations, researchers are developing a second class of theranostic nanoparticles that can provide on-demand therapy without incorporating potentially toxic drugs; these nanoparticles have intrinsic properties suitable for imaging and therapy. One recently developed and interesting technique uses a laser pulse to generate intracellular plasmonic nanobubbles (PNBs) around excited gold nanoparticle clusters (Lukianova-Hleb *et al.* 2010; Lukianova-Hleb *et al.* 2010). The laser energy determines the size and lifetime of the bubble created, allowing precise control over imaging and therapy: nanometer-sized PNBs act as diagnostic agents by scattering light from a probe laser, while larger micrometer-sized PNBs rapidly expand and collapse to induce mechanical damage to cell membranes. While this new theranostic platform is exciting in that it offers cell-specific imaging and therapy, it requires additional development. Currently the pump and probe

lasers operate at 532 nm and 690 nm, respectively, which are outside the tissue water window (650-900 nm), so it is likely that application in large organisms will be limited by light penetration. Furthermore, the technique relies on nanoparticle cluster formation through receptor-mediated endocytosis and since this process cannot be controlled, it is uncertain whether PNB generation will work in large tumors where individual cell-uptake of nanoparticles may be heterogeneous throughout the tumor volume.

While plasmonic nanobubbles offer an interesting approach to combined cancer imaging and therapy, they are still in the early stages of development; a more established theranostic approach is to use iron oxide or gold-based plasmonic nanoparticles for cancer hyperthermia and simultaneous imaging. One advantage of these nanoparticles is that because they have already demonstrated therapeutic efficacy against a variety of tumor types *in vivo,* clinical translation of theranostic approaches that incorporate these nanoparticles may be more rapid. Furthermore, these nanoparticles are appropriate imaging agents without modification. Maier-Hauff *et al.* recently reported results of a clinical trial of magnetic fluid hyperthermia (MFH) in which the density of aminosilane-coated iron-oxide magnetite nanoparticles was mapped in glioblastoma tumors using computed tomography (CT) to guide subsequent thermotherapy (Maier-Hauff *et al.* 2010). They observed a significant increase in patient survival compared to a reference population, a remarkable feat given the aggressive nature of this type of tumor. Even so, MFH also exhibits limitations, one being the high iron concentration (~30 mg/cm^3 tumor) required for heating; it will be critical to monitor long-term effects of this high nanoparticle exposure. Perhaps a more noteworthy limitation is that MRI cannot be used to track tumor progression after nanoparticle infusion due to imaging artifacts caused by

their presence. Given that MRI is a very common diagnostic method, it will be undesirable to exclude its use.

As an alternative to IONPs, gold-based nanoparticles for cancer hyperthermia (such as nanorods, nanoshells, and nanocages) are an acceptable theranostic platform whose use has not been shown to interfere with the performance of MRI and CT. These nanoparticles also achieve effective heating at much lower concentrations than IONPs, reducing the risk of nanoparticle-induced toxicity in clearance organs such as the liver, spleen, and kidney. Gold-based, NIR-resonant nanoparticles are suitable contrast agents for a variety of optical imaging modalities, allowing oncologists to choose the imaging technique most appropriate for the tumor location. Moreover, optical imaging is rapid and simple, allowing quick tumor visualization prior to subsequent laser application for thermal therapy. Thus far, optical coherence tomography (Cang *et al.* 2005; Gobin *et al.* 2007) and photoacoustic tomography (Wang *et al.* 2004; Li *et al.* 2009; Song *et al.* 2009; Lu *et al.* 2010) have been evaluated with gold-based NIR-resonant nanoparticles as contrast agents, but these techniques are limited to wide field-of-view applications. In the next section, multiphoton microscopy will be introduced as a more promising imaging modality that offers high resolution at the microscopic level, with the ability to obtain both functional and morphological information.

4.1.2 Multiphoton Microscopy

Multiphoton microscopy has historically been used to evaluate fluorescent signals in cell and animal model studies (Zipfel *et al.* 2003). Similar to confocal microscopy, multiphoton microscopy excites fluorophores by delivering photons with a focused laser beam. With confocal microscopy a continuous wave, visible wavelength laser delivers

single photons of energy sufficient for fluorophore excitation; however, because the excitation is not limited to the focal plane, a pinhole must be added to the optical configuration to eliminate out-of-focus light and improve image resolution. Instead, multiphoton microscopy incorporates an ultrafast, pulsed laser to simultaneously deliver two near-infrared photons of half the required excitation energy. As a result, acquired images have superior resolution since NIR light interferes minimally with tissue and only fluorophores at the focal plane of the laser become excited since this is where the probability of two photon events is maximal. The differences in fluorophore excitation between confocal microscopy and multiphoton microscopy are represented in **Figure 4.1**. Although fluorophores are the traditional contrast agents for two-photon microscopy, recent work has demonstrated that nanoparticles with strong surface plasmon resonance in the near-infrared regime can be employed as well. The next section will expand on use of nanoparticles as multiphoton contrast agents reported in recent literature.

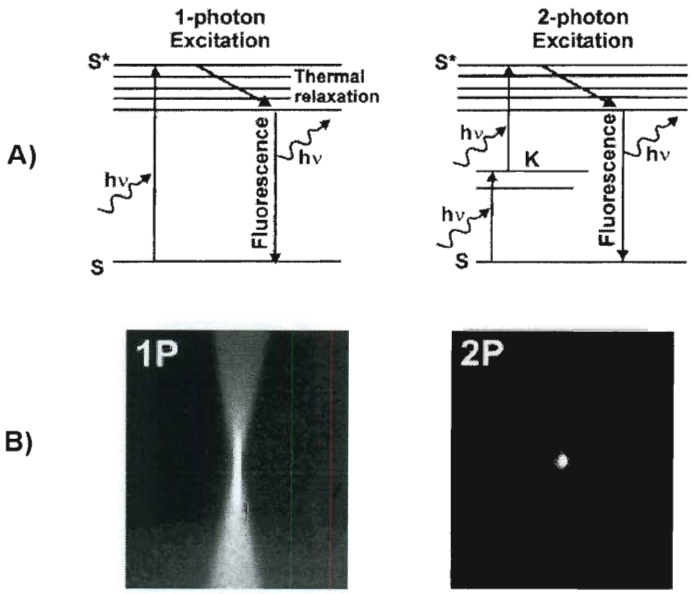

Figure 4.1: Comparison of one- and two-photon fluorophore excitation. A) Jablonski diagrams of the excitation, relaxation, and fluorescence emission processes. B) Excitation occurs throughout a fluorescein solution with single-photon illumination but only at the focal volume using two-photon excitation. (Soeller and Cannell 1999).

4.1.3 Multiphoton Microscopy with Near-Infrared Absorbing Nanoparticles

Advances in the use of nanoparticles as contrast agents for multiphoton microscopy came following the discovery by Boyd *et al.* that roughened metal surfaces exhibit two-photon induced photoluminescence (TPL), a phenomenon attributed to coupling of light with localized plasmon resonances (Boyd *et al.* 1986). Similarly, NIR-resonant nanoparticles excited with a pulsed laser luminesce when electrons in the sp-band recombine with holes in the d-band created following near-simultaneous absorption of single photons (Imura *et al.* 2005). Recent studies of two-photon induced photoluminescence of silica-gold nanoshells and gold nanorods have indicated that these nanoparticles display enhanced properties for multiphoton microscopy compared to traditional fluorophores, including brighter signals and increased resistance to photobleaching (Wang *et al.* 2005; Park *et al.* 2008). Specifically, the TPL signal of a single nanorod is nearly 60 times brighter than a single rhodamine 6G molecule (Wang *et al.* 2005), and nanoshells are approximately 140 times brighter than fluorescent beads and display brightness on the same order of magnitude as nanorods (Park *et al.* 2008). Furthermore, the signal intensity of both nanoshells (Bickford *et al.* 2008) and nanorods (Durr *et al.* 2007) is much greater than cell autofluorescence in this spectral region, enabling superior contrast with this imaging modality. The enhanced luminescent signal reported for gold-based nanoparticles compared to traditional fluorophores and the ease of conjugation of biomolecules to gold surfaces renders these materials ideal contrast agents for multiphoton microscopy.

In this thesis, gold-gold sulfide nanoparticles (GGS-NPs) were tested as a theranostic alternative to nanoshells and nanorods for combined multiphoton microscopy and thermal cancer therapy. Although GGS-NPs have been utilized as drug-delivery

vehicles (Huang *et al.* 2008; Ren *et al.* 2008; Tan *et al.* 2009), mediators of hyperthermia (Gobin *et al.* 2010), and as single nanoparticle molecular sensors (Raschke *et al.* 2004) their application as simultaneous imaging and therapy probes has not been previously explored; in this chapter, the multifunctional capacity of GGS-NPs will be demonstrated. Considering that GGS-NPs display stronger absorption efficiency than nanoshells and do not possess the toxicity concerns associated with the capping surfactants of nanorods, these nanoparticles appear ideally suited as theranostic agents. In the following experiments, the optical properties and gold surface chemistry of GGS-NPs were exploited to provide targeted contrast and therapy of cancerous cells *in vitro.* Using the same chemistry described in Chapter 3 for silica-gold nanoshells, GGS-NPs were functionalized with anti-HER2 antibodies to specifically target SK-BR-3 breast carcinoma cells that over-express the HER2 receptor (Kraus *et al.* 1987). This receptor is amplified in approximately 30% of breast cancer cases, thereby making it an excellent target for novel therapeutics (Slamon *et al.* 1987). Upon exposure to a pulsed NIR laser, GGS-NPs demonstrated TPL and could therefore be used to visualize targeted SK-BR-3 cells *in vitro* via multiphoton microscopy with low incident laser powers. By then increasing the power output of the excitation laser, thermal damage could be induced to targeted cells and not to non-targeted cells. The ability to image GGS-NPs during their concurrent use as photothermal agents renders them highly attractive for use in cancer management, particularly since most procedures necessitate specific heat delivery to maintain integrity of nearby vital tissue.

4.2 Materials and Methods

4.2.1 Nanoparticle Preparation

Gold-gold sulfide nanoparticles were synthesized as described in Chapter 2 following literature techniques (Averitt *et al.* 1999; Schwartzberg *et al.* 2007). GGS-NPs were visualized with transmission electron microscopy (TEM); the diameter of at least 50 nanoparticles per sample was measured with ImageJ software (NIH, Bethesda, MD). Calculation of the mean diameter revealed a slight batch-to-batch variability in average particle size, which ranged from 26 nm to 37 nm. Dynamic light scattering was also incorporated to assess nanoparticle size, and analysis of multiple batches with a ZetaSizer NanoZS (Malvern Instruments, Worcestershire, UK) revealed an average hydrodynamic diameter of 42.2 nm, in good agreement with the TEM results.

GGS-NPs were conjugated to either anti-HER2 (NeoMarkers, Fremont, CA) or nonspecific anti-IgG (Sigma) antibodies using 2 kDa orthopyridyl-disulfide-poly(ethylene glycol)-N-hydroxysuccinimide (OPSS-PEG-NHS, Creative PEGWorks, Winston Salem, NC) as a linker. PEG-antibody conjugates were prepared by reacting one part 125 μM OPSS-PEG-NHS with 9 parts 1 mg/ml antibody at 4°C overnight. This reaction produces a stable amide bond between primary amines on the antibody and carboxyl groups on the PEG chain that are exposed when the NHS terminus is cleaved in water. Particles suspended in milli-Q water at an optical density of 1.5 were exposed to PEG-antibody conjugates for 1 h at 4°C at a 100:1 volumetric ratio. Following antibody coupling, GGS-NPs reacted with a solution of mPEG-SH (5 mM, 5 kDa, Laysan Bio, Inc., Arab, AL) for a minimum of 4 h at 4°C (1:200 volumetric ratio) to passivate any exposed gold surface area. GGS-NPs coated with mPEG-SH only (no antibody) were

also synthesized for use as a negative control. Self-assembly of PEG-antibody and mPEG-SH onto the nanoparticle surface is possible due to dative interactions between sulfur and gold. Following antibody and/or PEG modification, GGS-NPs were centrifuged to remove unbound molecules, aspirated, and suspended in phosphate buffered saline (PBS) at an optical density of 2.0 (~4.2×10^{11} particles/ml) unless otherwise noted.

4.2.2 Quantification of Antibody Bound to Nanoparticles

To verify that antibody and mPEG-SH successfully bound the GGS-NP surface, changes in hydrodynamic diameter were monitored. Using a Malvern ZetaSizer NanoZS, four nanoparticle formulations were studied: (1) Bare GGS-NPs, (2) GGS-NPs coated with mPEG-SH, (3) GGS-NPs coated with mPEG-SH and anti-IgG antibodies, and (4) GGS-NPs coated with mPEG-SH and anti-HER2 antibodies. The mean hydrodynamic diameter was averaged from three sets of nanoparticles, with individual sets also tested in triplicate.

Antibodies present on GGS-NPs were quantified using the modified enzyme-linked immunosorbent assay (ELISA) introduced in Chapter 3. Targeted (coated with mPEG-SH and antibody) and control (only mPEG-SH coated) nanoparticles were incubated with 10 μg/ml horseradish peroxidase (HRP)-labeled goat anti-mouse IgG (for quantification of mouse anti-human HER2) or HRP-labeled rabbit anti-goat IgG (for quantification of goat anti-mouse IgG) (both HRP antibodies from Sigma). Nonspecific reaction sites were blocked with a 3% solution of bovine serum albumin (BSA, Sigma) in PBS. To remove unbound HRP-labeled antibodies, the nanoparticles were centrifuged twice at 1500 g for 8 min and suspended in 3% BSA. The HRP bound to GGS-NPs was

developed with 3,3',5,5'-tetramethylbenzidine dihydrochloride (Sigma) for 15 min and the reaction stopped by addition of 2 M sulfuric acid. Developed HRP was compared to a standard curve of the appropriate HRP-labeled anti-IgG by measuring the absorbance at 450 nm with a spectrophotometer. The number of peroxidase-labeled anti-IgG moieties was divided by the number of GGS-NPs in solution to calculate the number of antibodies per nanoparticle. The number of nanoparticles was derived from the Beer-Lambert law with the extinction coefficient of GGS-NPs obtained from Mie theory as described in the literature (Averitt *et al.* 1999).

4.2.3 Instrumentation

A Zeiss Laser Scanning Microscope (LSM) 510 Meta (Carl Zeiss, Inc., Thornwood, NJ) equipped with a femtosecond-pulsed Ti:sapphire laser source (Chameleon, Coherent, Inc., Santa Clara, CA) was used to perform multiphoton microscopy and photothermal therapy experiments. The wavelength of the output laser beam was tuned to match the peak extinction of the GGS-NPs and operated with a pulse width of 140 fs and repetition rate of 90 MHz. A short-pass dichroic mirror reflected incident NIR light onto the sample through a 20X objective (numerical aperture (NA) = 0.75) or a 63X objective (NA = 1.4) and passed photoluminescence. An infrared-blocking filter reduced background signal and the META detector collected TPL from the GGS-NPs between 451-644 nm. A schematic of the microscope configuration is provided in **Figure 4.2**. For these studies, average excitation power was measured with a power meter placed at the focal plane of the objective.

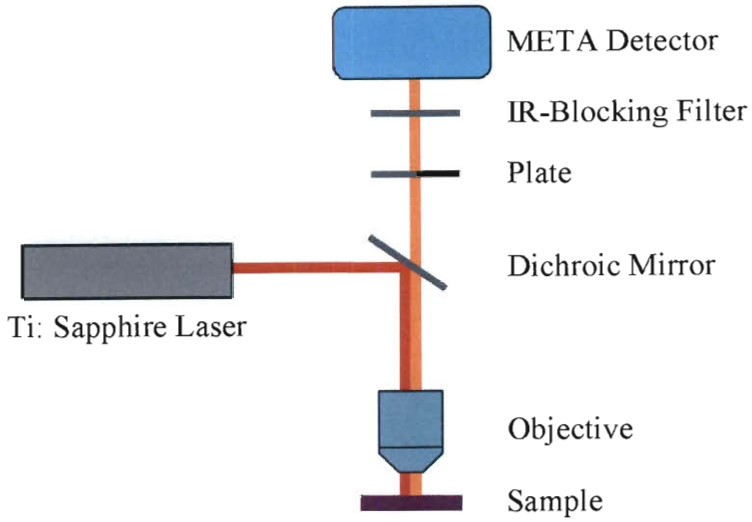

Figure 4.2: Multiphoton system configuration.

4.2.4 Verification of Two-Photon Induced Photoluminescence

The ability of GGS-NPs to produce two-photon induced photoluminescence (TPL) was probed by imaging particles in aqueous solution with the multiphoton microscope excitation power ranging from 1-10 mW. The average emission intensity determined with ImageJ software was plotted versus excitation power to observe any correlation. To aid comparison of the signal from GGS-NPs with luminescence reported in the literature for other nanoparticles, silica-gold nanoshells (149 nm diameter) were also synthesized and imaged. For comparative analysis, 500 µl nanoshells and GGS-NPs in aqueous solution at equal optical density (OD = 10) at 800 nm were loaded in separate chambers on coverglass and imaged with 1 mW and 10 mW excitation. The mean intensity per particle was determined using ImageJ software (NIH) to calculate the ratio of signal intensity between the two particle types.

4.2.5 Cell Culture

For *in vitro* imaging and therapy analysis, SK-BR-3 breast carcinoma cells (American Type Culture Collection, Manassas, VA), which over-express the HER2 receptor, were cultured in McCoy's 5A growth medium (Sigma) containing 10% fetal bovine serum and 1% penicillin-streptomycin at 37°C in a 5% CO_2 environment. Cells transferred to 15 ml conical tubes (6 x 10^5 cells/tube) were centrifuged (115 g, 3 min) to form pellets that were subsequently suspended in 1 ml of one of the four following solutions: (1) GGS-NPs coated with anti-HER2 and mPEG-SH, (2) GGS-NPs coated with anti-IgG and mPEG-SH, (3) GGS-NPs coated with only mPEG-SH, or (4) PBS. Cells incubated in these solutions for 30 min at 37°C in a hybridization chamber (VWR International, West Chester, PA) with constant 7 rpm rotation. Following incubation, the samples were centrifuged (115 g, 3 min), aspirated, and diluted in PBS to remove any particles not bound to the cells. This rinsing procedure was repeated three times followed by suspension in 1 ml growth media. Interestingly, the pellets of cells exposed to anti-HER2 conjugated GGS-NPs appeared dark to the eye while those of cells exposed to control nanoparticles or PBS appeared white, indicating the affinity of these nanoparticles for their targeted cell surface antigens. Cells were cultured on chambered coverglass overnight before experiments were performed.

One advantage of two-photon microscopy in biomedical applications is that high-resolution 3D images can be constructed due to the exceptional optical sectioning. To mimic tissue and determine the imaging depth of multiphoton microscopy with GGS-NP contrast agents, collagen phantom gels were prepared. First, SK-BR-3 cells were exposed to anti-HER2 functionalized GGS-NPs or PBS as described above. Then a gel

precursor was made and aliquoted into chambered coverglass in 5 μl droplets; the precursor consisted of 167 μl cell suspension (1 x 10^6 cells/ml), 83 μl 0.1 N NaOH, 83 μl 10X sterile PBS, and 667 μl collagen. The droplets cured in a 37°C oven to promote gel formation, and cell culture media (500 μl) was added prior to imaging the samples with the multiphoton microscopy system.

4.2.6 Multiphoton Microscopy and Photothermal Ablation

For imaging nanoparticles bound to cells in 2D, incident laser power was 1 mW with a pixel dwell time of 12.8 μsec, and the laser beam was raster-scanned across a 450 μm x 450 μm area through a 20X objective. Calculating laser intensity by dividing power by the area of the Airy disc, this power corresponds to a fluence of 0.96 J/cm^2. For multiphoton microscopy in 3D gels, the power was increased to 2 mW while reducing pixel dwell time to 6.4 μsec, thus maintaining the fluence used in 2D experiments. In these experiments, different focal planes were imaged throughout the entire gel by adjusting the focal height by 5 μm between scans.

The ability of GGS-NPs to act as both imaging and therapy agents was assessed using the 2D system by first imaging SK-BR-3 cells with the laser power of 1 mW. To perform photothermal ablation the samples were repositioned and the laser power was increased to 50 mW with a 12.8 μsec dwell time (thus yielding 48.1 J/cm^2 fluence). Samples were treated with a single pass of the laser for both imaging and therapy. One hour later, cells were labeled with calcein AM (1 μM, Molecular Probes, Eugene, OR), a live cell stain, and ethidium homodimer-1 (4 μM, Molecular Probes), a dead cell stain. Fluorescence microscopy was performed with an inverted Zeiss Axiovert 135 phase contrast microscope (Carl Zeiss) to determine viability.

4.2.7 Determining Effects of Therapy on Cell Membrane Structure

Loss of membrane integrity is one mechanism of cell death induced by localized nanoparticle heating. Therefore, to monitor any changes in membrane structure, another set of 2D experiments was performed in which SK-BR-3 cells were labeled with the lipophilic membrane stain DiI (5 μM, Molecular Probes, Eugene, OR) for 10 min at 37°C prior to incubation with the anti-HER2 nanoparticles or PBS as described in Section 4.2.5. DiI-labeled cells were exposed to 50 mW laser power and imaged with high-resolution (63X, NA = 1.4) time-lapse photography to monitor changes in membrane morphology. For this laser power, pixel dwell time, and numerical aperture, the fluence was calculated to be ~30 J/cm^2. A 543 nm laser excited DiI while GGS-NPs were simultaneously excited with the pulsed 810 nm Ti:Sapphire laser.

4.3 Results and Discussion

4.3.1 Nanoparticle Characterization

A representative TEM and extinction spectrum for the GGS-NPs are displayed in **Figure 4.3**. Successful conjugation of targeting moieties to the GGS-NPs was confirmed by monitoring increases in hydrodynamic diameter and by quantifying the attachment with a solution-based ELISA. Bare GGS-NPs possessed a mean hydrodynamic diameter of 42.2 nm that increased to 58.0 nm upon addition of mPEG-SH. Further increase occurred when either antibody formulation was included, with diameter of 69.8 nm for anti-IgG coated nanoparticles and 63.4 nm for anti-HER2 coated nanoparticles. These results suggested that the antibody and mPEG-SH were able to self-assemble on the nanoparticle surface using the disulfide or thiol therminus, respectively.

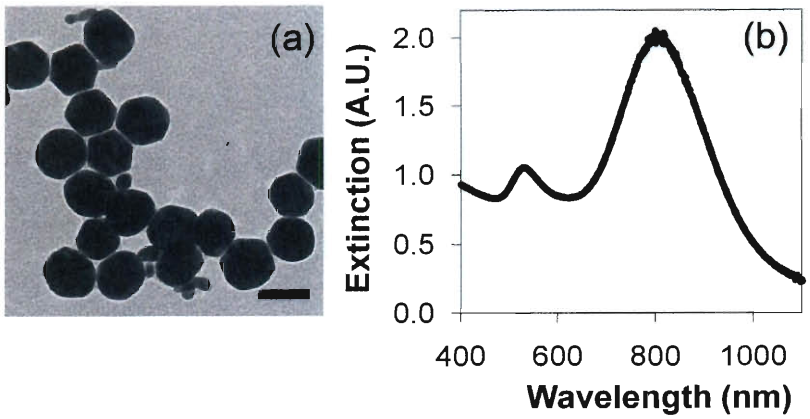

Figure 4.3: Characterization of GGS-NPs. (a) TEM of GGS-NPs. Scale bar = 40 nm. (b) Extinction spectrum of GGS-NPs with peak resonance at 800 nm.

Antibody quantification confirmed that both anti-HER2 and anti-IgG coated GGS-NPs bound significantly more HRP-antibodies than PEG-coated GGS-NPs ($p<0.01$ for both using a student's t-test). The ELISA on anti-HER2 GGS-NPs indicated 55.0 ± 4.0 antibodies per nanoparticle, while control GGS-NPs remained free of antibody (-1.3 ± 2.6 antibodies/nanoparticle). Similar antibody densities were obtained for anti-IgG GGS-NPs compared to control GGS-NPs, with targeted nanoparticles bearing 32.6 ± 3.2 antibodies/nanoparticle and control GGS-NPs showing negligible background (-1.1 ±1.5 antibodies/nanoparticle).

4.3.2 Gold-Gold Sulfide Nanoparticles Exhibit Two-Photon Induced Photoluminescence

The ability of GGS-NPs to produce TPL was probed by imaging nanoparticles in aqueous solution with the multiphoton microscope excitation power ranging from 1-10 mW. A quadratic dependence of nanoparticle emission intensity as a function of incident laser power was observed, with the slope of the fit linear curve being 2.06 ± 0.03, indicating a two-photon absorption process (**Figure 4.4**) (Wang *et al.* 2005; Durr *et al.* 2007;

Bickford *et al.* 2008; Park *et al.* 2008). When the mean luminescence intensity of several hundred GGS-NPs and silica-gold nanoshells was compared, analysis revealed that at 1 mW excitation the brightness ratio of GGS-NPs to nanoshells was 1:1.03, proving that GGS-NPs are on the same order of magnitude brightness as silica-gold nanoshells, which have already demonstrated success as *in vivo* multiphoton contrast agents (Park *et al.* 2008). When excitation power was increased to 10 mW, the brightness ratio of GGS-NPs to nanoshells increased to 2.57:1. The damage threshold for silica-gold nanoshells has been reported as 4.5 mW, and therefore it is possible that the reduced nanoshell luminescence resulted from particle melting (Park *et al.* 2008). The GGS-NPs appear to have a higher damage threshold than nanoshells have, indicating that GGS-NPs may convert more incident multiphoton energy to luminescence than to heat, thereby making them more suitable as combined diagnostic and therapeutic agents. However, it should be noted that this explanation is speculative as experiments confirming/refuting damage were not included in this study.

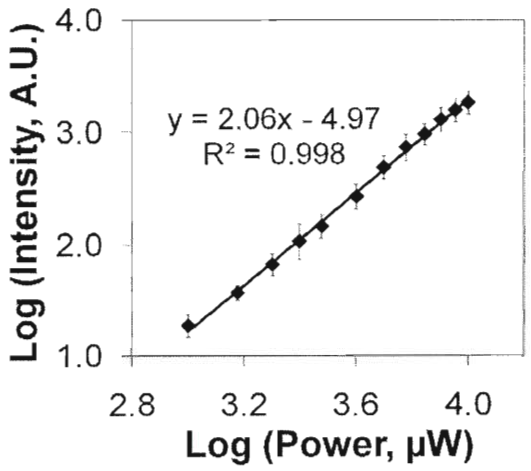

Figure 4.4: GGS-NPs exhibit two-photon induced photoluminescence. GGS-NPs display a quadratic dependence of luminescence intensity on excitation power when exposed to an 800 nm pulsed laser.

4.3.3 Antibody-Conjugated Gold-Gold Sulfide Nanoparticles Enable Imaging and Thermal Ablation of Targeted Breast Cancer Cells

The application of GGS-NPs as dual agents for cancer imaging and treatment was investigated by utilizing low laser powers (1 mW) to image cancerous cells tagged with anti-HER2 targeted nanoparticles and high laser powers (50 mW) to induce cell death via nanoparticle heating. Results of two-photon microscopy performed with 1 mW excitation are displayed in **Figure 4.5**, where **Figure 4.5(a)** displays the TPL signal (observed only for anti-HER2 GGS-NPs attached to SK-BR-3 cells), **Figure 4.5(b)** is a brightfield (BF) image of the same field of view, and **Figure 4.5(c)** is an overlay of the TPL and BF images. Successful targeting of SK-BR-3 cells with anti-HER2 GGS-NPs was demonstrated by the increased TPL signal versus controls as shown in **Figure 4.5(a)**. At this laser power, SK-BR-3 cells alone (samples incubated with PBS) did not exhibit a luminescent signal; thus any luminescence observed can be attributed to the presence of GGS-NPs. Cells incubated with nanoparticles functionalized with nonspecific antibodies or with only mPEG-SH could not be discerned, thereby verifying that these non-targeted nanoparticles were removed during the rinsing process and proving the specific targeting of anti-HER2 functionalized GGS-NPs to SK-BR-3 cells.

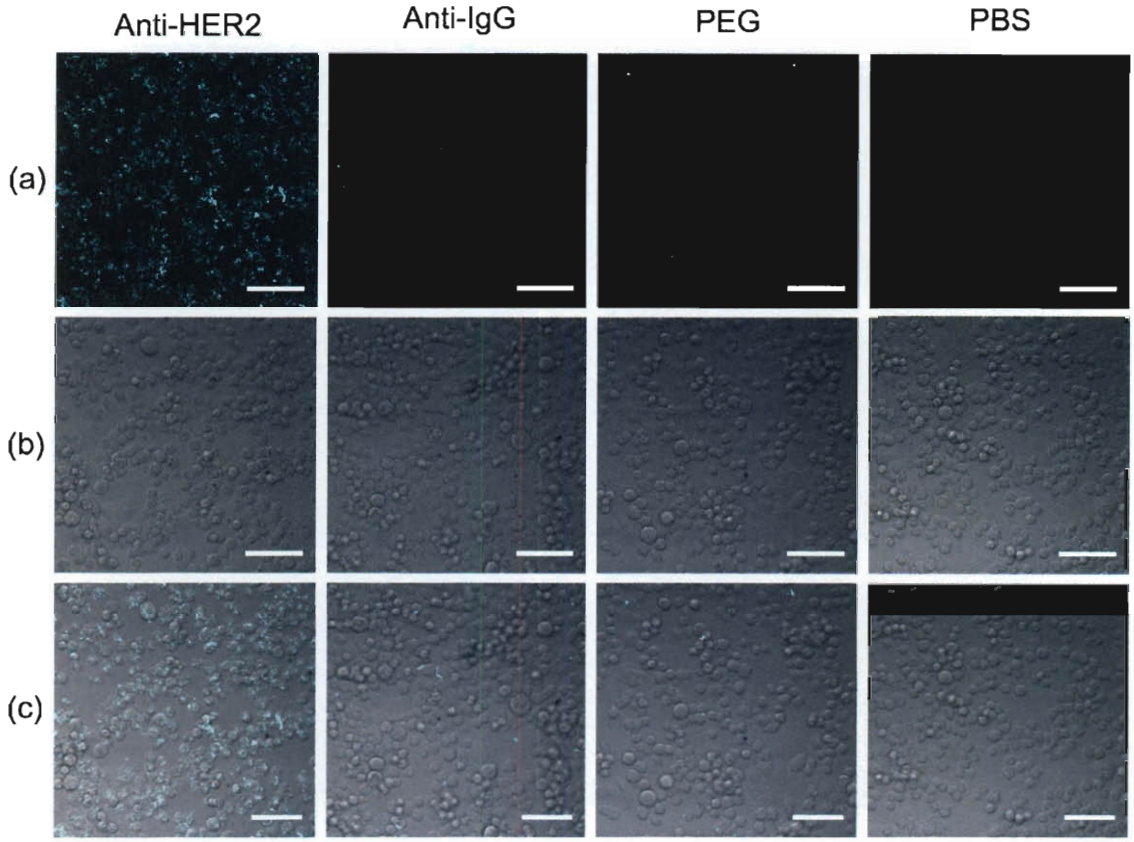

Figure 4.5: Anti-HER2 GGS-NPs provide enhanced contrast of cancer cells. (a) Two-photon photoluminescence images of SK-BR-3 cells exposed to the pulsed laser operating at 1 mW. (b) Brightfield images in the same field-of-view as the luminescence images. (c) Overlay of images (a) and (b), showing that luminescence is confined to cells targeted with anti-HER2 GGS-NPs. Scale bars = 100 μm.

In collagen gels containing SK-BR-3 cells previously exposed to anti-HER2 GGS-NPs, nanoparticle luminescence was observed throughout the entire thickness (~200 μm). **Figure 4.6** shows a 3D reconstruction of the TPL signal rendered in ImageJ; additionally, merged brightfield/TPL images from various depths within the gel verify that the signal co-localized with cells. No luminescence was observed in gels containing cells previously exposed to PBS. The observed imaging depth of 200 μm using GGS-NPs improves upon reported imaging depths of 75 μm for gold nanorods in tissue phantoms (Durr *et al.* 2007) and 130 μm for nanoshells in tumors (Park *et al.* 2008).

Furthermore, it is possible that using GGS-NPs as contrast agents may allow even deeper imaging because the depth of field of the objective used in these experiments prevented imaging further into the samples.

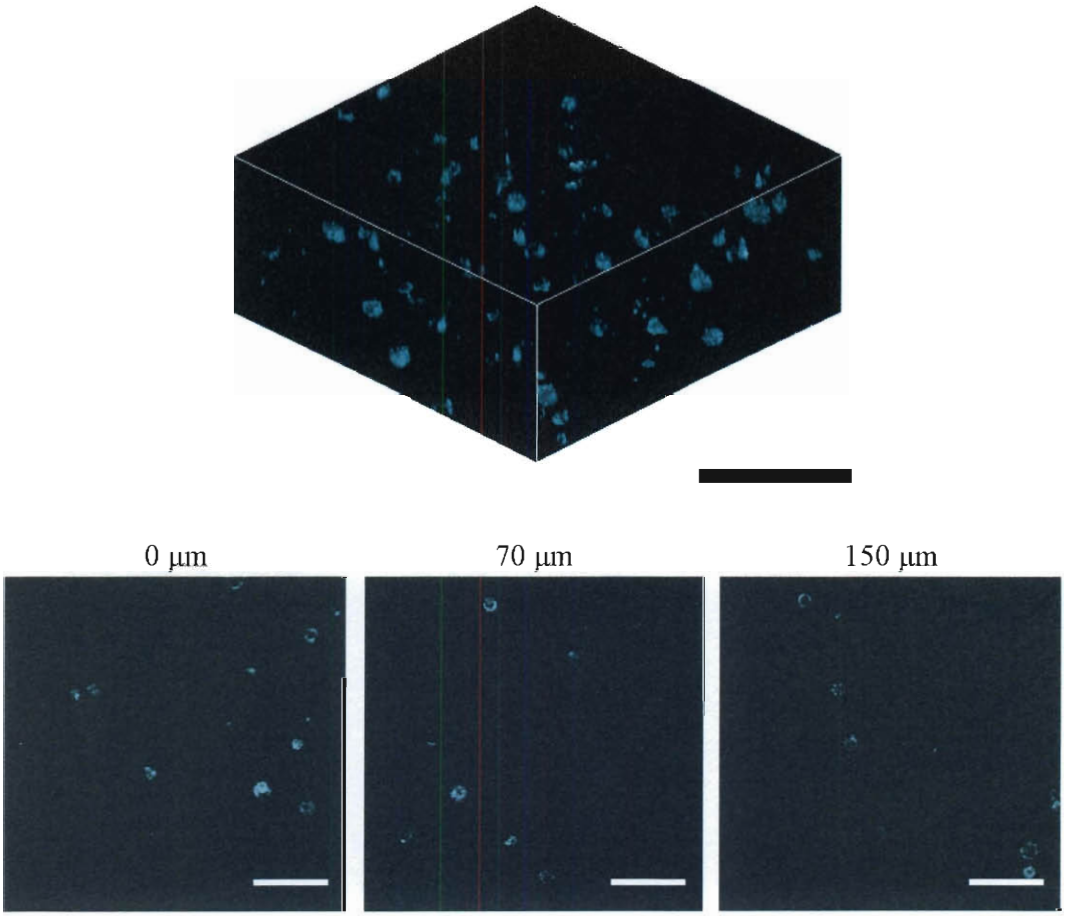

Figure 4.6: Two-photon microscopy of cells in collagen gels. Photoluminescence from anti-HER2 GGS-NPs enabled visualization of cells throughout a 200 μm thick collagen gel (top; scale bar = 200 μm). The bottom row displays a merged TPL and brightfield image from three depths within the gel, verifying that the nanoparticle signal co-localized with cells and was confined to a thin optical section (scale bars = 100 μm).

For nanoparticle-assisted laser therapy, the samples were repositioned and the laser power increased to 50 mW. **Figure 4.7** displays results of the viability/cytotoxicity assay performed after exposing cells to the nanoparticles and laser. No loss in cell viability was observed in regions exposed to 1 mW laser power (0.96 J/cm^2) indicating

that this energy is insufficient to induce localized heating of the GGS-NPs in this time frame and can be safely implemented to image nanoparticle-targeted cells. Using 50 mW laser power (48.1 J/cm^2) samples previously exposed to PBS or control nanoparticles remained viable, while cell death was induced by thermal damage in cells exposed to anti-HER2 GGS-NPs, indicated by the red EthD-1 fluorescence in the square-shaped region where the laser beam was raster-scanned across the sample (**Figure 4.7**). Cells outside the laser path remained viable, implying that anti-HER2 GGS-NPs alone were not toxic. This observation is in keeping with the results of prior studies that have examined and established the biocompatibility of GGS-NPs (Huang *et al.* 2008; Ren *et al.* 2008).

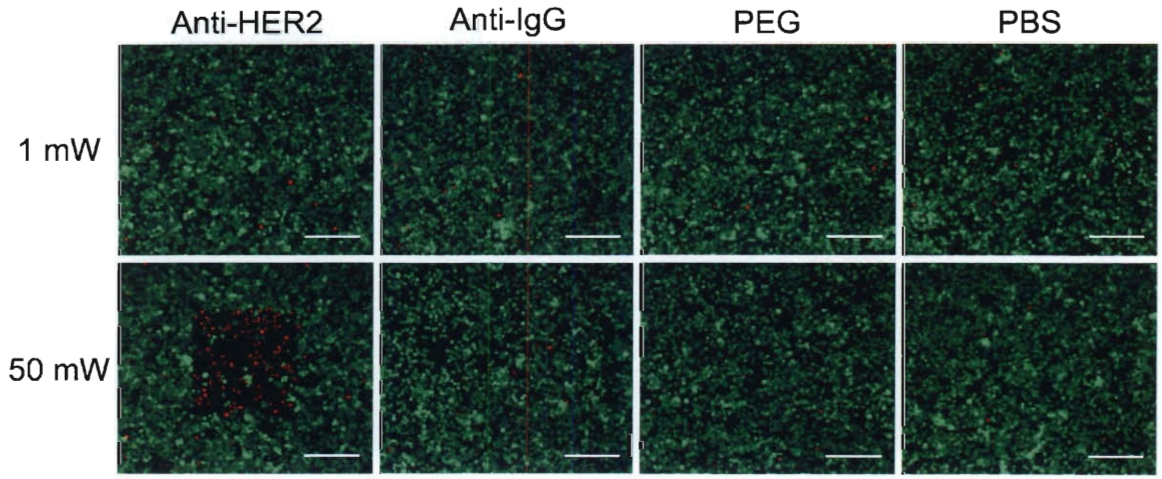

Figure 4.7: GGS-NPs yield targeted cell death with sufficient incident laser power. Cancerous cells remained viable (evidenced by green calcein AM fluorescence) when exposed to 1 mW laser power, regardless of nanoparticle presence. At 50 mW laser power a red fluorescent ethidium homodimer-1 signal indicative of membrane damage was observed in cells exposed to anti-HER2 GGS-NPs only where the laser was applied. Laser exposure alone was harmless to cells, as was laser exposure combined with nonspecifically targeted nanoparticles. Scale bars = 250 μm.

4.3.4 Photothermal Therapy Compromises Cell Membrane Integrity to Induce Cell Death

The results of the calcein AM/ethidium homodimer-1 live/dead stain following sufficient laser exposure suggested that one mechanism of cell death was loss of membrane integrity caused by localized nanoparticle heating. EthD-1 is excluded from cells with an intact membrane; thus, the EthD-1 signal observed in targeted SK-BR-3 cells exposed to the 50 mW laser suggested that structural damage took place during photothermal therapy. To observe these changes, SK-BR-3 cells were labeled with DiI (a lipophilic membrane stain) prior to incubation with anti-HER2 GGS and exposure to the NIR laser. During therapy, changes in membrane morphology were observed using time-lapse photography.

As seen in **Figure 4.8**, membrane morphology of cells exposed to anti-HER2-GGS-NPs appeared normal before the 50 mW laser was applied (t = 0 seconds), initial signs of membrane damage appeared within 10 seconds, and extensive damage due to hyperthermia occurred within 30 seconds. Control cells exposed to only the 50 mW laser did not display signs of membrane injury. During this study it was noted that constant excitation with the 50 mW pulsed laser caused the observed GGS-NP TPL signal to diminish over time, a finding which is consistent with reports of decreased TPL signals for nanorods after prolonged exposure to a continuous wave laser operating between 7.5 and 60 mW (Huff *et al.* 2007) or a pulsed laser above 10 mW (Black *et al.* 2008). This loss in signal is likely due to restructuring/melting of the nanoparticles, although further studies need to be performed to confirm this hypothesis.

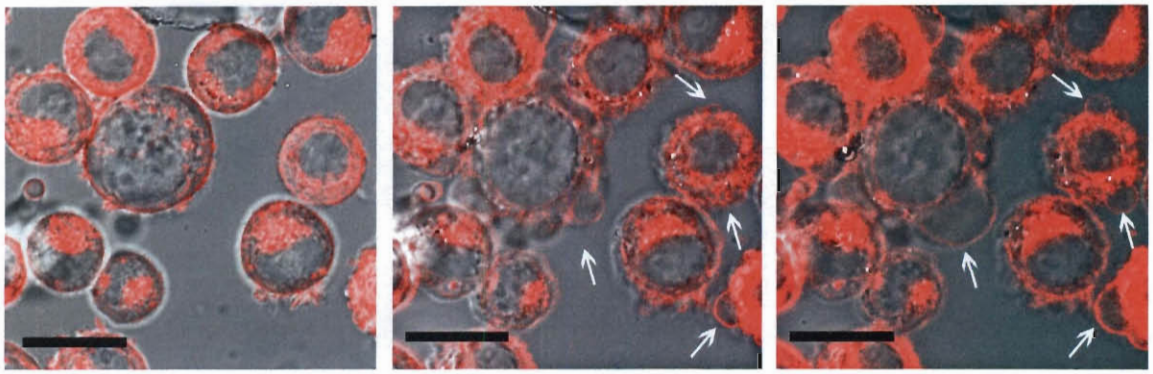

Figure 4.8: Time-lapse photography of cells exposed to anti-HER2 GGS-NPs and 50 mW laser power. The fluorescent red DiI membrane stain indicates regions of membrane blebbing generated by localized hyperthermia, with examples indicated by white arrows. Scale bar = 20 μm.

4.3.5 Discussion

Theranostic nanoparticles have potential to fulfill the need for novel methods to detect and treat neoplasia that thoroughly eliminate disease and improve survival while minimizing side effects since the thermal insult is confined to a small spatial region. The objective of these studies was to demonstrate that GGS-NPs can be used simultaneously as contrast and therapeutic agents using conventional multiphoton microscopy. In the foreseeable future, this technology will be limited to applications where the tumor is easily accessible due to the restricted penetration depth (several hundred microns) of pulsed near-infrared laser light; therefore breast carcinoma was used as a model system. Because epidermal growth factor receptor 2 (HER2) is amplified in approximately 30% of breast cancer cases and is associated with a poor prognosis clinically, it is an excellent target for novel anti-cancer agents (Slamon *et al.* 1987). GGS-NPs can be specifically targeted towards SK-BR-3 breast carcinoma cells that express this receptor *in vitro* by functionalizing the gold surface with anti-HER2 antibodies, and these targeted cells can

be visualized using the two-photon induced luminescence of GGS-NPs under excitation with a low-intensity pulsed NIR laser. Using a higher intensity of the laser caused nanoparticle heating that induced membrane blebbing and yielded photothermal ablation of targeted cancer cells. This study provided a proof-of-concept that GGS-NPs used in conjunction with multiphoton microscopy can provide the ability to "see and treat" tumors in a single setting.

GGS-NPs offer several advantages that render them attractive among the growing list of gold-based nanoparticle regimens for cancer management. As previously mentioned, GGS-NPs are smaller than silica-gold nanoshells and nanorods, two of the most thoroughly studied gold-based nanotherapeutics; this smaller size may correlate with improved stability and enhanced tumor delivery *in vivo* (Zhang *et al.* 2009; Gobin *et al.* 2010). GGS-NPs also do not require capping with surfactants; removing this requirement eliminates toxicity concerns associated with surfactants such as the cetyl-trimethylammonium bromide (CTAB) surfactant used to prepare nanorods (Niidome *et al.* 2006) and it leaves the gold surface available for conjugation to biomolecules. This thesis provided the first demonstration that antibodies can be tethered to GGS-NPs by utilizing the available gold and exploiting the same chemistry used for coating silica-gold nanoshells (see, for example: (Lowery *et al.* 2006) and (Gobin *et al.* 2008)).

Another advantage of GGS-NPs is that they absorb light more efficiently than nanoshells, and this enhanced absorption should yield improved imaging and therapy. Though GGS-NPs have been studied for many years, their application in photothermal cancer therapy has only recently been explored (Gobin *et al.* 2010). In that work, a continuous wave laser was used to excite the GGS-NPs, while in this work a pulsed laser

was employed. Use of a pulsed laser not only provides a new imaging capability by producing TPL from the nanoparticles; it also enables simultaneous therapy and this is the first demonstration that the nanoparticles may be used as a theranostic device. It should be noted that use of a high intensity pulsed laser also allows therapy to be achieved more rapidly and with lower total energy dosages than required for continuous lasers, and using lower laser total energies should cause significantly less heating and damage to surrounding tissue *in vivo*.

The main advantage of two-photon microscopy in medical imaging is the ability to provide sub-cellular resolution at depths of up to several hundred microns in tissue (Zipfel *et al.* 2003). Advancement of this technology to the clinical setting is currently hindered by the cost and size of commercially available multiphoton microscopes; however, the price of femtosecond pulsed lasers should decrease as they become more commonly used, and research to miniaturize two-photon microscopes and reduce their complexity is ongoing. Recent successes in development of two-photon endoscopes were achieved by incorporating microelectromechanical systems (MEMS) scanning mirrors into the microscope design (Hoy *et al.* 2008; Jung *et al.* 2008). Specifically, Piyawattanametha *et al.* have fabricated a lightweight (2.9 g), MEMS-based two-photon microscope and demonstrated its ability to track individual red blood cells flowing in neocortical microvasculature of adult mice, establishing the future potential for two-photon imaging *in vivo* (Piyawattanametha *et al.* 2009). With further development, multiphoton microscopy combined with dual imaging and therapy GGS-NPs could provide an effective method to pinpoint and treat specific sites following initial tumor detection with wide-field imaging modalities. In one potential application, TPL of

targeted nanoparticles could indicate tumor margin status and any suspicious cells could be eliminated with higher intensity photoablation, removing the need for biopsies and additional surgery. This ability to "see and treat" would be particularly beneficial when preservation of normal tissue surrounding neoplastic regions is critical.

4.4 Conclusions

The data presented confirms that NIR-absorbing GGS-NPs have properties that render them suitable as a multifunctional agent for cancer management using multiphoton microscopy. Nanoparticles functionalized with anti-HER2 antibodies bound effectively to SK-BR-3 breast carcinoma cells, while those coated with anti-IgG or mPEG-SH did not attach to cancer cells. Luminescence emitted by GGS-NPs upon excitation with a pulsed laser resulted from a two-photon absorption process and was as bright as luminescence emitted from silica-gold nanoshells. At 1 mW laser excitation, SK-BR-3 cells labeled with anti-HER2 GGS-NPs were safely visualized and upon increasing excitation to 50 mW, cell death was induced following membrane blebbing. Nanoparticle heating and subsequent cell death was confined to the area where the laser beam was raster-scanned across the sample. Irradiation alone at either power did not generate changes in cell morphology or cause loss of viability.

These results indicate that GGS-NPs are an appropriate choice of theranostic agent for use with multiphoton microscopy. GGS-NPs decorated with antibodies can provide enhanced contrast of targeted cancer cells versus non-targeted healthy cells at low incident powers; if imaging results suggest that a region is highly malignant, a higher power can then be applied to induce localized nanoparticle heating and subsequent hyperthermic damage to the suspicious lesion. Having the ability to visualize and treat

tumor cells with high precision will improve cancer management by minimizing damage to normal tissue surrounding neoplastic regions. In addition, removing the waiting period between time of detection and time of treatment will prevent increases in tumor burden that cause eradication of the disease to become more difficult.

Chapter 5: Evaluation of Nanoparticle-Mediated Thermal Therapy Using a Subcutaneous Brain Tumor Model

5.1 Introduction

Primary brain tumors represent one of the most challenging forms of neoplasia to treat. High-grade glioma is the most aggressive type of primary brain tumor and despite medical intervention the median survival is only 12-15 months and 5-year survival is less than 5% (Daumas-Duport *et al.* 1988; Stupp *et al.* 2005; Wen and Kesari 2008; Gladson *et al.* 2010). Surgery is an acceptable treatment option *if* the tumor location is amenable to removal, but often the infiltrative nature of high-grade glioma prevents complete resection. Radiation therapy and chemotherapy are also viable treatment options but they are plagued by side effects that range from minor reactions (e.g. nausea, hair loss) to extreme complications such as personality changes, loss of physical ability, or cognitive dysfunction (Butler *et al.* 2006; Ricard *et al.* 2009). Therefore, there is a significant need for advances in care not only to improve survival but also to improve quality of life post treatment. This chapter evaluates the ability of nanoparticle-mediated photothermal therapy to meet this need using an *in vivo* subcutaneous tumor model.

5.1.1 Transport of Nanoparticles to Brain Tumors for Drug Delivery and Hyperthermia

A major obstacle to successful management of brain tumors is the precise delivery of therapeutic agents, a problem compounded by the blood-brain barrier (BBB). The BBB is a physical barrier, composed of tightly connected brain capillary endothelial cells, that

inhibits transport of molecules into the brain, preventing delivery of potentially useful therapeutic agents. The BBB is often disrupted in high-grade glioma but it remains intact in early stage brain tumors; consequently, researchers have recently begun to investigate nanoparticles as chemotherapeutic delivery vehicles or as exogenous energy absorbers for hyperthermia treatment of glioma. These approaches have found moderate success and the potential of nanobiotechnology in management of glioma has recently been highlighted in an excellent review article (Jain 2010). In cases where the BBB is disrupted, nanoparticle-drug complexes may be delivered to the tumor systemically; however, if the BBB remains intact other delivery methods must be employed. In this section, four methods to enhance nanoparticle accumulation in brain tumors with an intact BBB will be introduced.

One strategy to enhance drug delivery to brain tumors is convection enhanced delivery (CED), a technique that establishes fluid convection in the brain by maintaining a positive pressure gradient during interstitial infusion. In a recent paper, Hadjipanayis *et al.* demonstrated that antiEGFRvIII antibody could be conjugated to 10 nm diameter iron oxide nanoparticles (IONP) and delivered to brain tumors using CED (Hadjipanayis *et al.* 2010). The IONPs served two purposes in this study: (1) to act as a therapeutic agent and (2) to act as a magnetic resonance imaging (MRI) contrast agent, allowing delivery to the tumor to be monitored in real time. *In vitro* the antiEGFRvIII-IONP conjugates induced apoptosis of EGFRvIII-expressing glioblastoma cells but not normal astrocytes. In a subsequent experiment mice bearing malignant glioma tumors in the right striatum were exposed to either serum, IONPs only, antiEGFRvIII only, or antiEGFRvIII-IONP conjugates and all the treatment groups had a significant improvement in survival time

versus the serum control group when data was analyzed with a log-rank test. Median survival was 11 days, 16 days, 17 days, and 19 days, respectively. These results demonstrate the promise of using nanoparticles and CED to enhance drug delivery to brain tumors.

A second technique to improve brain tumor drug delivery involves physically disrupting the blood-brain barrier for a short period of time. Liu *et al.* introduced a two-pronged approach to enhance delivery of the anticancer drug epirubicin to brain tumors using iron oxide nanoparticles as the carrier platform (Liu *et al.* 2010). In this method the permeability of the BBB was increased locally using focused ultrasound (FUS) and then an external magnetic force was applied to attract the magnetic IONPs coated with epirubicin and enhance their deposition at the target site. When tested in mice bearing intracranial tumors, T1-weighted MRI confirmed that FUS disrupted the BBB and T2-weighted MRI showed that magnetic targeting (MT) provided an increase in local accumulation of IONPs. Interestingly, the amount of nanoparticles in the tumor increased with magnetic field strength and correlated with the relaxivity of the nanoparticles. Most importantly, the level of epirubicin delivered to the tumor with combined FUS/MT was sufficient to slow tumor growth (106% volume increase with treatment after 8 days compared with 313% growth for control) and increase survival (18.3 days for control, 20.5 days for epirubicin-IONPs with FUS/MT). To further validate this method a study should be performed that compares tumor response following delivery of free epirubicin with delivery using IONPs and combined FUS/MT.

The modalities described above utilized iron oxide nanoparticles as drug delivery vehicles that simultaneously enable distribution to be monitored in real time, and are just

two examples of a variety of strategies being developed to evade the BBB and enhance delivery of chemotherapeutics to brain tumors. Another way to evade the BBB is to deliver nanoparticles or drugs directly into the tumor, although this increases the invasiveness of therapy and thus is generally undesirable. German researchers demonstrated this approach in a recent Phase II trial of magnetic fluid hyperthermia (Maier-Hauff *et al.* 2010). In that work, IONP solutions were administered into the tumor and treatment consisted of six semi-weekly thermotherapy sessions with adjunct stereotactic beam radiotherapy performed immediately before or after each session. As mentioned in Chapter 4, this paper reported an improvement in survival compared to a historical reference population (Maier-Hauff *et al.* 2010). However, Weller and Wick recently contested these results by identifying several flaws in the study design, including that: (1) comparison to historical populations is an inappropriate method to determine efficacy, (2) efficacy could not be demonstrated since an experimental treatment was combined with an established treatment, and (3) the authors did not collect data on subsequent treatments taken by the patients, making it impossible to estimate the impact of treatment (Weller and Wick 2010). Despite the current controversy surrounding the results, the study does establish the future potential of nanoparticle-mediated thermal therapy for elimination of brain tumors.

Lastly, a fourth approach to enhance nanoparticle deposition within brain tumors possessing an intact BBB is macrophage-mediated delivery. Macrophages have a natural ability to traverse the BBB, so Hirschberg and colleagues investigated whether nanoshell-loaded macrophages could penetrate tumor spheroids composed of human grade IV glioma cells (Baek *et al.* 2011). They found that macrophages containing silica-gold

nanoshells penetrated deeply into the spheroids and upon laser irradiation these spheroids displayed significant growth reduction compared to spheroids that received empty macrophages. This delivery method remains to be validated in future *in vivo* experiments.

A variety of components in the systems described above can be altered to optimize treatment efficacy, including the choice of nanoparticle and drug, the surface chemistry utilized, and the delivery mechanism employed. With further development it is possible that nanoparticle delivery to brain tumors for drug release and hyperthermia may improve the prognosis for patients with primary brain tumors. While the delivery methods discussed in this section focused on evading the blood-brain barrier, it has been demonstrated that the BBB is not fully functional in all brain tumors; in these cases cancer cells may be directly targeted. In the next section, targeting brain tumors via cell surface receptor expression will be discussed.

5.1.2 Targeting Brain Tumors via Anti-IL13Rα2

The blood-brain barrier is preserved in low-grade brain tumors, but most highly malignant gliomas have disrupted BBBs at clinical presentation. Investigations have shown there is an opening of interendothelial tight junctions in human gliomas (Long 1970) that is accompanied by loss or down-regulation of the tight junction molecules claudin-1, claudin-5, and occludin (Liebner *et al.* 2000). In addition, glioma cells secrete factors that actively degrade the intact BBB, but the nature of these factors remains unknown (Schneider *et al.* 2004). As a result of these molecular and morphological changes, the capillaries of highly malignant tumors are more leaky than those in normal brain tissue, thus providing a route for enhanced nanoparticle or drug accumulation in

these tumors. This difference may be further exploited by targeting therapies toward surface receptors expressed on tumor cells, such as interleukin-13 receptor alpha 2.

Interleukin-13 receptor alpha 2 (IL13Rα2) is highly expressed in many adult and pediatric gliomas, while expression in the normal brain is practically non-existent (Joshi *et al.* 2000; Kawakami *et al.* 2004). This receptor, which binds the T-cell derived cytokine interleukin-13, has subsequently emerged as a promising target for novel therapeutics. For example, Madhankumar *et al.* demonstrated that IL13-coated liposomes carrying doxorubicin could specifically bind glioblastoma multiforme tissue specimens but not normal cortex (Madhankumar *et al.* 2006). Furthermore, the IL13-conjugated liposomes demonstrated enhanced therapeutic efficacy compared to non-targeted liposomes *in vivo* using a subcutaneous glioma tumor mouse model. Other IL13Rα2-targeted therapies in development include cytotoxins (Debinski *et al.* 1999), viruses (Zhou and Roizman 2006), and immunotherapies (Eguchi *et al.* 2006).

Similarly, silica-gold nanoshells coated with anti-IL13Rα2 antibodies have been shown to bind and mediate photothermal ablation of glioma cells *in vitro* (Bernardi *et al.* 2008). The first aim of this chapter was to expand upon this *in vitro* success and to evaluate the benefit of this molecular targeting strategy by comparing the distribution of anti-IL13Rα2-coated and PEG-coated nanoshells and gold-gold sulfide nanoparticles in mice bearing subcutaneous U373 glioma tumors. While it was anticipated that antibody targeting would provide increased nanoparticle accumulation in subcutaneous tumors, the results did not indicate such an advantage. Therefore, in the second aim of this chapter, the ability of nanoparticle-mediated photothermal therapy to eradicate high-grade glioma *in vivo* was examined with only PEG-coated nanoparticles. By commencing *in vivo*

experiments of nanoparticle-mediated photothermal therapy with subcutaneous tumors, it was possible to establish the sensitivity of these tumors to hyperthermia before moving forward to the more complicated intracranial tumor model to be discussed in Chapter 6.

5.2 Materials and Methods

5.2.1 Nanoparticle Preparation and Characterization

Nanoshells (NS) and GGS-NPs were prepared using the methods of Chapter 2. PEG-antibody (PEG-Ab) conjugates made by reacting one part 125 μM OPSS-PEG-NHS (Creative PEGWorks) with 9 parts 1 mg/ml mouse anti-human IL13Rα2 (Cell Sciences, Canton, MA) at 4°C overnight were mixed with particles suspended in milli-Q water at an optical density of 1.5 for 1 h. GGS-NPs received 125 PEG-Ab per nanoparticle and NS received 1000 PEG-Ab per nanoparticle. Following antibody coupling, particles incubated with mPEG-SH (5 mM for GGS-NPs/1 mM for NS, 5 kDa, Nektar, Huntsville, AL) overnight at 4°C to passivate any exposed gold surface area. Nanoparticles of each type were also prepared with only mPEG-SH (no antibody). Following antibody and/or PEG modification, nanoparticles were centrifuged to remove unbound molecules, aspirated, and suspended in sterile phosphate buffered saline (PBS) at an optical density of 60. This corresponds to ~1.7×10^{11} particles/ml for NS and ~1.1×10^{13} particles/ml for GGS-NPs. The number of antibodies present on the nanoparticles' surfaces was quantified using the ELISA method introduced in Chapter 3.

5.2.2 Cell Preparation

U373 human high-grade glioma cells (ATCC, Manassas, VA) were engineered to constitutively express the firefly luciferase gene to enable imaging of tumor growth *in*

vivo. An MSCV (murine stem cell virus) retroviral vector with a gene encoding the fusion protein eGFP-Firefly Luciferase (eGFP.FFLuc) was used to generate firefly luciferase expressing cells (Ahmed *et al.* 2007). Cells were seeded at low density in a 6-well plate in a high-titer retroviral supernatant derived from a producer cell line stably transfected to shed these viral particles. Polybrene facilitated viral entry into the U373 cells. This procedure was repeated 2-3 times after which cells were harvested and sorted for eGFP positivity. The intensity of light was tested routinely in a luminometer after addition of 150 mg/kg D-luciferin (Xenogen, Alameda, CA) prior to conducting the animal experiments to ensure the uniformity of light emission from the tumor cells.

5.2.3 Tumor Implantation and Bioluminescent Imaging

Firefly luciferase-expressing U373 cells were maintained in RPMI 1640 medium (Invitrogen Corp., Carlsbad, CA) supplemented with 1% glutamine and 10% fetal bovine serum and cultured at 37°C in a 5% CO_2 environment. Cells were detached from culture flasks with trypsin-EDTA and diluted in culture media for inoculation into mice. All animals were used under an approved protocol of the Institutional Animal Care and Use Committee of Baylor College of Medicine. To induce tumor growth, 10^6 U373 cells were injected subcutaneously in the right hind flank of male IcrTac:ICR-Prkdc^{SCID} mice (Taconic Farms, Hudson, NY). Tumor development was monitored by measurement with calipers and with bioluminescent imaging. When tumor diameter reached 3-5 mm, the mice received intravenous injections of 100 µl PEG-coated or anti-IL13Rα2-coated nanoshells (1.7×10^{11} particles/ml), GGS-NPs (1.1×10^{13} particles/ml), or saline. These concentrations correlate to equal optical densities (OD = 60) of the nanoparticle types.

Isoflurane anesthetized animals were imaged using the Xenogen IVIS 100 system (Caliper Life Sciences, Alameda, CA) 10 min after receiving intraperitoneal injections of 150 mg/kg D-luciferin (Xenogen), which emits light when oxidized in the presence of luciferase and ATP. The photons emitted from luciferase-expressing U373 cells within the animal body and transmitted through the tissue were quantified using "Living Image," a software program provided by the same manufacturer. A pseudo-color image representing light intensity (blue least intense and red most intense) was generated and superimposed over the grayscale reference image. Mice were imaged daily following cell implantation to monitor tumor development.

5.2.4 Assessment of Nanoparticle Distribution and Verification of Target Expression

A biodistribution study determined the time of maximum nanoparticle accumulation in tumors following intravenous delivery (and thus the optimal time for laser application). Three mice per group were euthanized at 6, 24, and 48 h post-tail vein injection of nanoparticles and the blood, brain, tumor, spleen, liver, and muscle were collected for assessment of gold content. Each tissue specimen was divided into three pieces—one for qualitative analysis of nanoshell accumulation by histology and two for quantitative analysis with neutron activation analysis (NAA) and inductively coupled plasma-mass spectrometry (ICP-MS). Blood was only tested by NAA and ICP-MS.

Sample Preparation for Neutron Activation Analysis and Inductively Coupled Plasma-Mass Spectrometry

Samples for NAA were lyophilized, weighed, and shipped to Texas A&M University for analysis as described previously (James *et al.* 2007). Blanks and samples

were irradiated with calibration standards in the Texas A&M University's Nuclear Science Center 1 MW TRIGA research reactor for 4-14 h based on the anticipated gold content. The irradiation position used has an average neutron flux of ~$1x10^{13}$ n/(cm^2s). High purity germanium detectors with nominal resolutions of 1.74 keV or better and efficiencies of 25-47% by industry standard measurement quantified the 412 keV gamma-line from ^{198}Au. Gold concentrations were acquired and computed with Canberra Industries' Open VMS alpha processor-based Genie-ESP software.

ICP-MS samples were lyophilized, weighed, and digested with 0.5 ml aqua regia for 48 h. Trace grade nitric acid and hydrochloric acid were purchased from Sigma-Aldrich (St. Louis, MO) and VWR (West Chester, PA), respectively. Digested samples were further diluted with 1% aqua regia and filtered through a 0.45 μm filter. Standard solutions of known gold concentrations were prepared in 1% aqua regia using certified reference material Gold Standard for ICP (Sigma-Aldrich). The standards and samples were analyzed for ^{197}Au with germanium as an internal standard using the ELAN 9000 ICP-MS from Perkin-Elmer (Waltham, MA).

Preparation of Histological Specimens

Histological specimens were formalin-fixed, paraffin-embedded, and cut into 6 μm sections. To verify expression of the target receptor, tumor sections were stained and compared to muscle and brain. Deparaffinized and hydrated sections incubated with 10 μg/ml proteinase K for 15 min at 37°C to recover antigen. Slides were rinsed with water and PBS containing 0.05% Tween20 (PBST) and blocked with 5% BSA in PBST for 1 h prior to overnight incubation (4°C) with goat anti-human IL13Rα2 (15 μg/ml, R&D Systems). After three rinses with PBST, endogenous peroxidase activity was

quenched by 15 min treatment with 3% H_2O_2 in methanol. Following PBS rinsing, samples were exposed to HRP-conjugated rabbit anti-goat IgG (10 μg/ml, Abcam) for 1 h, rinsed with PBS and developed with AEC substrate for 10 min. Sections were counterstained with hematoxylin (Dako, Carpinteria, CA) for 1 min and blue stained nuclei were developed with 37 mM NH_4OH. Slides were mounted with Faramount media (Dako) and imaged with a Zeiss Axiovert 135 microscope.

To confirm nanoparticle presence, unstained specimens were examined by darkfield microscopy. Darkfield imaging was performed with the Axiovert 135 inverted microscope coupled to a CytoViva high-resolution adaptor (CytoViva, Auburn, AL). With this technique, indirect sample illumination enables image production from light scattered by the samples and nanoparticles are easily detected since they have enhanced scattering properties compared to tissue components (Loo *et al.* 2005; Loo *et al.* 2005; Gobin *et al.* 2008).

Some tumor samples for darkfield microscopy were also stained with FITC-conjugated anti-CD31 and DAPI to show nanoparticle proximity to blood vessels. To retrieve antigen, deparaffinized samples incubated with 10 μg/ml proteinase K for 15 min at room temperature. After blocking non-specific binding sites with 10% goat serum in PBS for 45 min, slides received rat anti-mouse CD31 (5 μg/ml) overnight. Three rinses (5 min each) were performed and then the slides received FITC-conjugated goat anti-rat IgG (20 μg/ml) for 1 h before a final rinsing procedure. A drop of Vectashield mounting medium containing DAPI was placed on each slide and the samples were sealed with coverglass prior to darkfield and fluorescence microscopy.

5.2.5 Assessment of Therapeutic Efficacy

After the biodistribution study confirmed that PEGylated nanoparticles delivered via the tail vein accumulated in subcutaneous U373 tumors, a survival study was carried out to evaluate the effectiveness of nanoparticle-mediated photothermal therapy *in vivo*. Tumor-bearing mice received intravenous injections of 100 µl PEG-coated NS (1.7×10^{11} particles/ml, n = 7 mice), PEG-coated GGS-NPs (1.1×10^{13} particles/ml, n = 7 mice), or saline (n = 8 mice) when tumor diameter reached 3-5 mm. Following a 24 h circulation period, mice were anesthetized with sodium pentobarbital (50 mg/kg, intraperitoneal injections) and tumors were swabbed with glycerol as an index matching agent prior to transdermal irradiation for 3 min with an 800 nm diode laser (Coherent, Inc., Santa Clara, CA) set to an intensity of 4 W/cm^2 (spot diameter = 9 mm). Tumor length and width were measured with digital calipers daily following treatment to track growth or regression. Tumor development was also monitored with bioluminescent imaging. Since photon flux from the tumor is proportional to the number of light emitting cells, the signal intensity indicates response to treatment. Mice were monitored for 90 days or until tumors reached 10 mm in largest diameter, at which point they were euthanized by carbon dioxide asphyxiation.

5.2.6 Statistical Analysis

Survival results were expressed as a Kaplan-Meier curve and survival between treatment and control groups was compared using a log-rank test with calculations performed in MedCalc Software (Mariakerke, Belgium). Differences in survival were considered significant for $p<0.05$.

5.3 Results and Discussion

5.3.1 Nanoparticle Characterization

Nanoparticles had peak plasmon resonance near 800 nm. **Figure 5.1** displays results of the ELISA, which indicated 171.5 antibodies/NS and 22.4 antibodies/GGS-NP; this result correlates to even surface coverage between the particle types when expressed as moles per surface area.

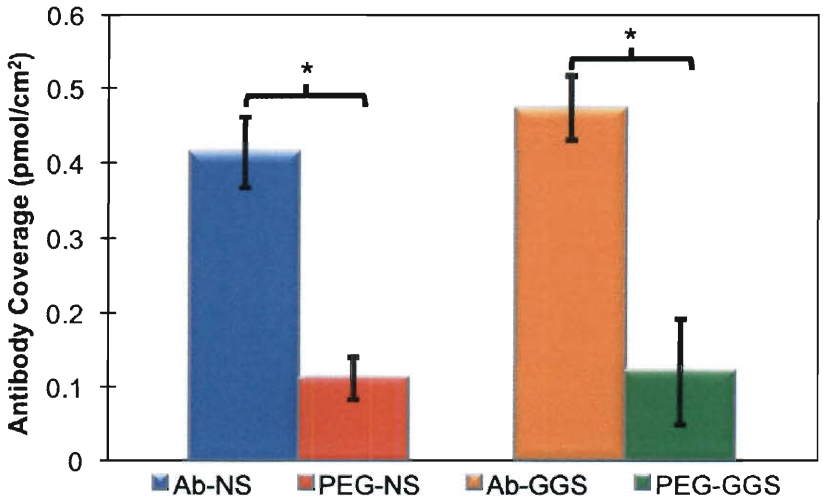

Figure 5.1: Surface coverage of anti-IL13Rα2 on nanoparticles. The antibody groups are significantly different from their PEG counterparts (*$p<0.05$, student's t-test).

5.3.2 Verification of Antigen Expression *In Vivo*

Immunohistochemistry confirmed presence of the target receptor (IL13Rα2) in the tumor tissue with pink staining (**Figure 5.2**). The muscle and normal brain show minimal staining, which is important since successful targeted therapy must be able to distinguish tumors from normal proximal tissue. Thus, the U373 tumor model is valid for studying targeted nanoparticle delivery *in vivo*.

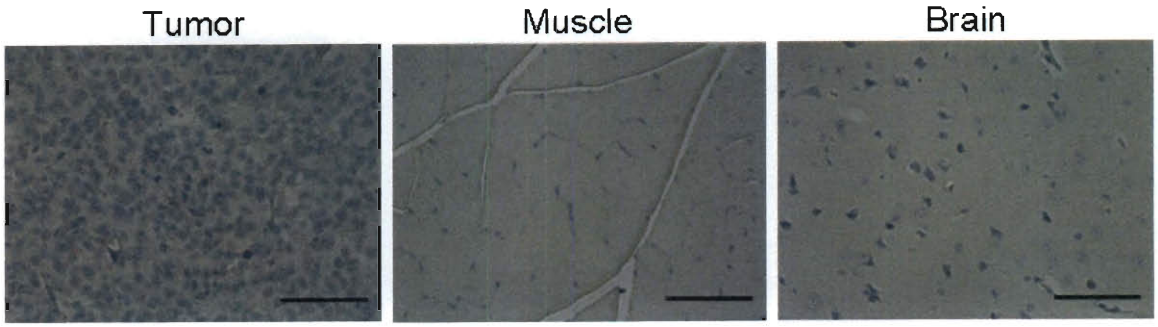

Figure 5.2: Immunohistochemistry verified IL13Rα2 expression in tumors. IL13Rα2 is stained pink (HRP/AEC) and nuclei are stained blue (hematoxylin). The receptor is not expressed in muscle adjacent to tumors or in the brain. Scale bars = 100 μm.

5.3.3. Quantitative and Qualitative Analysis of Nanoparticle Biodistribution in Tumor-Bearing Mice

No adverse effects of nanoparticle injections were observed at the delivery site or systemically in these experiments. Uptake in tumor and other organs was assessed through both quantitative and qualitative techniques and the results were in good agreement.

Analysis of Gold Content Demonstrated Nanoparticle Accumulation in Tumors

Neutron activation analysis (NAA) (James *et al.* 2007) and inductively coupled plasma-mass spectrometry (ICP-MS) (Niidome *et al.* 2006; De Jong *et al.* 2008; Sonavane *et al.* 2008) have been demonstrated as effective methods for determining gold content in tissue specimens. In this study the mean and standard deviation of gold content in each organ were calculated from three mice per nanoparticle group after circulating for 6, 24, and 48 h (ICP-MS results shown in **Figure 5.3**). Generally, the distribution trends observed with NAA and ICP-MS were in good agreement; however, it should be noted that NAA consistently reported higher gold content than ICP-MS. There are two possible explanations for this difference: (1) nanoparticles may be

heterogeneously distributed throughout the tissues; (2) the filtration step necessary to remove biological material from samples before entry into the ICP-MS may remove some gold from the solution. Nevertheless, both techniques are useful to determine trends of accumulation and the best time for laser irradiation. Results of ICP-MS are shown in Figure 5.3 and a table with complete results of ICP-MS and NAA for all particle types is provided in Table 5.1.

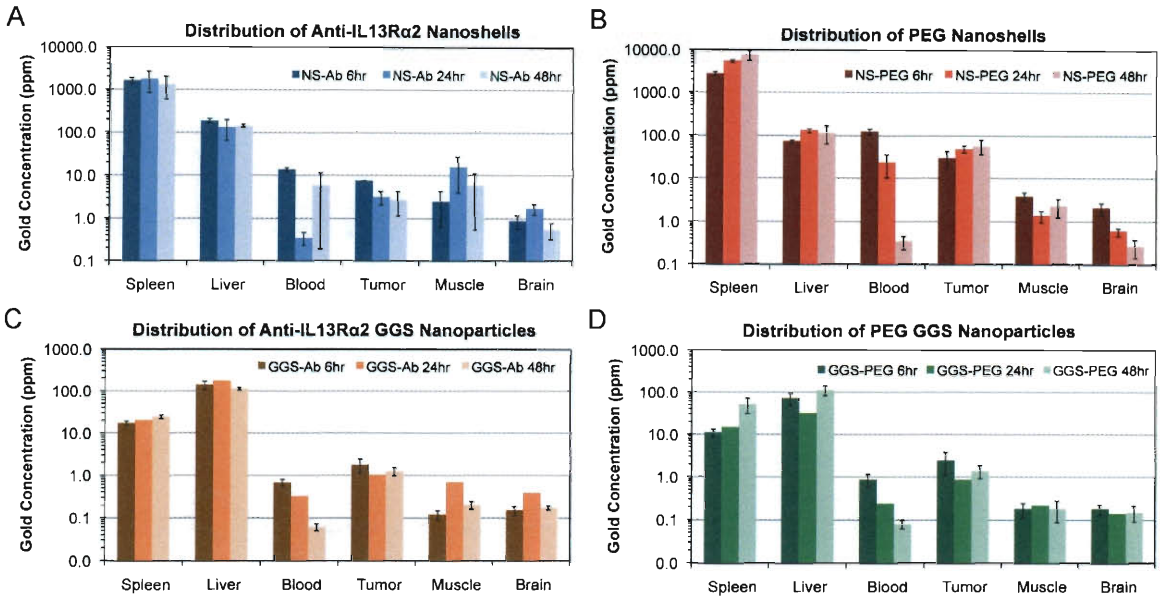

Figure 5.3: Distribution of PEG-coated and anti-IL13Rα2-coated nanoparticles. Gold present in six different organs at 6, 24, and 48 h post tail-vein delivery of antibody-targeted nanoshells (A), PEGylated nanoshells (B), antibody-coated GGS-NPs (C), or PEGylated GGS-NPs (D) determined by ICP-MS. Data depicts mean ± standard error for n=3 samples for all sets except GGS-NPs at 24 h, for which n=1.

For all nanoparticle formulations, as the level of gold decreased in the blood there was a subsequent increase in the spleen and liver, two organs associated with the reticuloendothelial system. Nanoshells cleared preferentially through the spleen, while GGS-NPs cleared mainly via the liver, indicating that nanoparticle size does influence *in vivo* behavior. There was minimal uptake in the muscle and brain at all times. PEG-

nanoshell clearance from the blood followed an exponential decay with a calculated circulation half-life of 4.8 h, comparable to the 4.1 h half-life of nanoshells determined by Xie *et al.* (2007). The circulation half-life of PEGylated GGS-NPs was 12.4 h. For nanoshells, the addition of antibody induced much more rapid removal from the blood, while GGS-NPs maintained a similar circulation half-life. In general, for PEG-NS the gold content measured in each organ followed the trends observed by James *et al.*, who used neutron activation analysis to assess biodistribution of 130 nm diameter nanoshells in healthy and tumor-bearing mice (James *et al.* 2007).

Although the original hypothesis was that molecular targeting via antibodies would yield enhanced tumor uptake, ICP-MS and NAA revealed that the maximum tumor uptake occurred with PEGylated nanoshells. The intratumoral PEG-NS concentration increased for the first 24 h following tail vein delivery and stabilized at ~50 ppm (μg gold/g dry tissue) thereafter; by comparison, the intratumoral gold content was less than 10 ppm for PEG-GGS, Ab-NS, and Ab-GGS (**Table 5.1**). The amount of PEG-NS in the tumor 24 h post-injection was 35 times higher than the concentration in muscle adjacent to the tumor, so collateral damage to normal tissue regions surrounding the tumor was anticipated to be minimal during photothermal therapy. One explanation for why antibody targeting did not promote tumor accumulation is that the Fc portion of the antibody may have accelerated opsonization (coating with blood proteins), marking the particles for more rapid clearance by the immune system. This is supported by the high level of gold observed in the liver for all antibody-conjugated particles at the 6 h timepoint when compared to the PEGylated formulations (Table 5.1).

Gold Content Determined by ICP-MS for Nanoshells Mean ± Standard Deviation (μg gold/g dry tissue)												
Time (hrs)	Spleen		Liver		Blood		Tumor		Muscle		Brain	
	anti-IL13Rα2	*PEG*	*anti-IL13Rα2*	*PEG*	*anti-IL13Rα2*	*PEG*	*anti-IL13Rα2*	*PEG*	*anti-IL13Rα2*	*PEG*	*anti-IL13Rα2*	*PEG*
6	1628.7 ± 379.1	2764.3 ± 482.2	189.5 ± 37.4	73.9 ± 9.2	13.7 ± 2.2	124.8 ± 29.7	7.6 ± --	29.5 ± 23.2	2.5 ± 3.2	3.9 ± 1.4	0.9 ± 0.5	2.1 ± 1.1
24	1758.8 ± 1579.6	5594.9 ± 615.1	133.5 ± 115.0	132.2 ± 24.7	0.3 ± 0.2	22.9 ± 21.7	3.2 ± 1.9	49.3 ± 13.8	15.7 ± 20.3	1.4 ± 0.7	1.7 ± 0.8	0.6 ± 0.2
48	1309.6 ± 1235.6	7645.2 ± 3411.7	141.2 ± 16.0	114.9 ± 85.5	5.8 ± 9.7	0.3 ± 0.2	2.7 ± 2.7	56.6 ± 35.4	5.8 ± 9.1	2.3 ± 1.8	0.6 ± 0.4	0.3 ± 0.2

Gold Content Determined by NAA for Nanoshells Mean ± Standard Deviation (μg gold/g dry tissue)												
Time (hrs)	Spleen		Liver		Blood		Tumor		Muscle		Brain	
	anti-IL13Rα2	*PEG*	*anti-IL13Rα2*	*PEG*	*anti-IL13Rα2*	*PEG*	*anti-IL13Rα2*	*PEG*	*anti-IL13Rα2*	*PEG*	*anti-IL13Rα2*	*PEG*
6	1731.3 ± 456.9	3771.7 ± 1119.4	443.7 ± 0.7	151.9 ± 32.5	25.9 ± 7.1	229.6 ± 57.7	22.2 ± 14.0	28.2 ± 17.5	2.2 ± 1.5	4.5 ± 1.9	2.8 ± 1.9	4.5 ± 3.1
24	1529.5 ± 1331.3	5791.5 ± 950.1	217.2 ± 185.0	251.6 ± 24.1	0.6 ± 0.5	42.6 ± 38.7	5.6 ± 8.2	58.2 ± 17.6	6.8 ± 7.9	2.8 ± 1.1	0.7 ± 0.5	2.0 ± 1.6
48	1370.9 ± 1277.8	7468.3 ± 1648.4	259.9 ± 54.5	221.3 ± 113.3	0.3 ± 0.1	0.6 ± 0.2	7.7 ± 6.5	51.5 ± 15.7	7.2 ± 11.2	1.5 ± 0.7	0.5 ± 0.4	1.4 ± 1.8

Gold Content Determined by ICP-MS for Gold-Gold Sulfide Nanoparticles Mean ± Standard Deviation (μg gold/g dry tissue)												
Time (hrs)	Spleen		Liver		Blood		Tumor		Muscle		Brain	
	anti-IL13Rα2	*PEG*	*anti-IL13Rα2*	*PEG*	*anti-IL13Rα2*	*PEG*	*anti-IL13Rα2*	*PEG*	*anti-IL13Rα2*	*PEG*	*anti-IL13Rα2*	*PEG*
6	17.2 ± 3.4	11.0 ± 3.3	139.5 ± 56.1	71.4 ± 39.8	0.68 ± 0.20	0.87 ± 0.47	1.77 ± 1.07	2.44 ± 2.30	0.12 ± 0.05	0.18 ± 0.11	0.15 ± 0.06	0.18 ± 0.08
24	20.2 ± --	14.6 ± --	173.8 ± --	31.6 ± --	0.32 ± --	0.24 ± --	1.00 ± --	0.86 ± --	0.69 ± --	0.22 ± --	0.38 ± --	0.14 ± --
48	24.2 ± 3.7	51.7 ± 35.0	112.9 ± 15.0	112.4 ± 50.0	0.06 ± 0.02	0.08 ± 0.03	1.24 ± 0.46	1.39 ± 0.80	0.20 ± 0.07	0.18 ± 0.16	0.17 ± 0.03	0.15 ± 0.10

Gold Content Determined by NAA for Gold-Gold Sulfide Nanoparticles Mean ± Standard Deviation (μg gold/g dry tissue)												
Time (hrs)	Spleen		Liver		Blood		Tumor		Muscle		Brain	
	anti-IL13Rα2	*PEG*	*anti-IL13Rα2*	*PEG*	*anti-IL13Rα2*	*PEG*	*anti-IL13Rα2*	*PEG*	*anti-IL13Rα2*	*PEG*	*anti-IL13Rα2*	*PEG*
6	41.2 ± 10.9	32.2 ± 10.0	323.9 ± 62.6	238.3 ± 80.6	1.61 ± 0.43	1.99 ± 1.33	8.12 ± 6.71	8.10 ± 2.36	0.62 ± 0.55	1.98 ± 2.4	0.33 ± 0.16	0.37 ± 0.24
24	52.2 ± --	56.1 ± --	465.8 ± --	72.3 ± --	7.81 ± --	0.61 ± --	5.31 ± --	5.42 ± --	2.68 ± --	0.37 ± --	0.81 ± --	0.37 ± --
48	56.4 ± 5.0	125.0 ± 93.0	329.6 ± 42.3	317.6 ± 53.1	0.14 ± 0.01	0.14 ± 0.04	6.64 ± 2.39	16.08 ± 7.93	0.34 ± 0.10	1.96 ± 0.55	0.23 ± 0.11	0.24 ± 0.24

Table 5.1: Gold concentration in dry tissue measured by ICP-MS and NAA. Data are the mean and standard deviation of gold in each organ determined from samples of three mice; groups without standard deviations reported had less than 3 samples.

Darkfield Microscopy Corroborated ICP-MS and NAA Results

Darkfield microscopy provided a visual confirmation of the ICP-MS and NAA findings. **Figure 5.4** displays sample images from tissue procured 24 h post-nanoparticle injections (except for GGS-Ab Tumor, which is from 48 h because the 24 h tumor was too small to divide between NAA, ICPMS, and histology). Nanoshells and GGS-NPs appear red against the blue-gray tissue background by darkfield microscopy due to their enhanced ability to scatter light, and were present in the spleen, liver, and tumor (Figure 5.4). Nanoparticles were not readily observed in the brain and muscle by darkfield microscopy; this was expected given that quantitative analysis indicated gold content in these tissues was minimal.

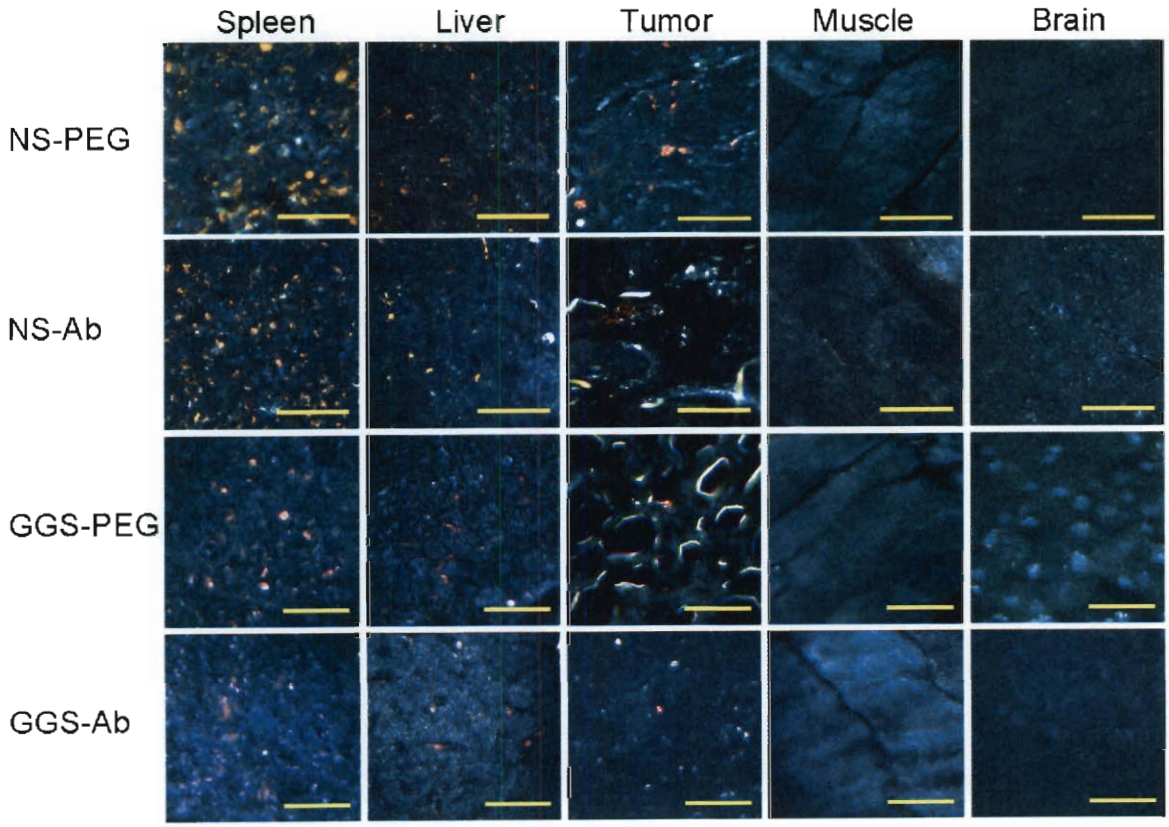

Figure 5.4: Darkfield microscopy visually confirmed nanoparticle biodistribution trends. Nanoparticles are visible in the spleen, liver, and tumor. Scale bars = 50 μm.

Since the PEGylated nanoshells displayed maximum tumor uptake, tumor sections from mice that received these particles were stained with FITC-antiCD31 and DAPI. Analysis with fluorescence and darkfield microscopy revealed that these nanoparticles remained in close proximity to the tumor vessels and can be observed traveling towards the center of the tumor from the highly vascularized periphery by flowing through the vessels (**Figure 5.5**). This supports the results of Perrault *et al.*, who recently demonstrated that nanoparticles with diameter greater than 100 nm have decreased diffusive transport and therefore do not extravasate beyond several cell lengths from tumor vessels (Perrault *et al.* 2009).

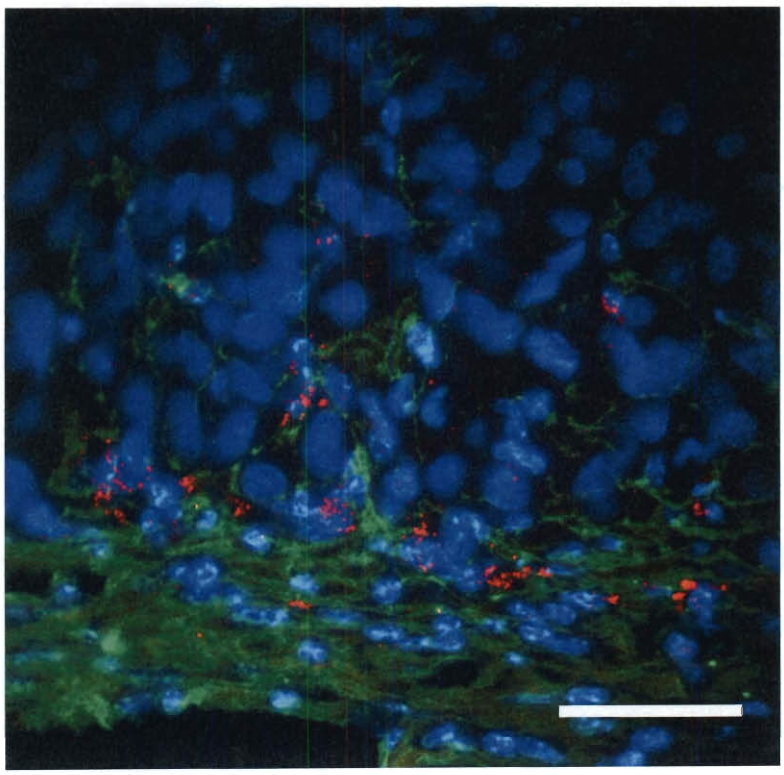

Figure 5.5: PEG-coated nanoshells remain proximal to tumor vessels. Darkfield and fluorescence microscopy show PEGylated nanoshells (pseudo colored red) traveling towards the center of the tumor from the periphery by flowing through the vessels (FITC-antiCD31, green). Nuclei are fluorescently labeled blue (DAPI). Scale bar = 50 μm.

5.3.4 Animal Survival Time Lengthens Following Nanoparticle-Mediated Photothermal Therapy

Based on the conclusions of the biodistribution study, laser exposure was performed 24 h post-tail vein delivery of PEGylated NS or GGS-NPs to give the nanoparticles sufficient time to accumulate in subcutaneous U373 tumors. Following laser irradiation mice were monitored daily to track tumor growth and regression using bioluminescent imaging and caliper measurements to indicate cellular development and changes in size. When the tumor reached 10 mm in largest diameter, the mice were euthanized. Nanoshell-mediated photothermal therapy induced tumor regression and led to improved survival versus control animals, while mice receiving GGS-NPs experienced only a partial response.

Bioluminescent Imaging Indicated Nanoshell-Mediated Photothermal Therapy Induced Tumor Regression

Bioluminescent imaging of tumors following laser irradiation helped distinguish each animal's response to therapy, with some mice experiencing complete response to treatment while others exhibited partial or non-response (**Figure 5.6**). The mouse shown in the first row of Figure 5.6 received nanoshell-assisted laser therapy and displayed complete tumor regression without signs of re-growth for the entire period of study. This mouse had a visible scab and loss of luminescence in the location of the tumor within just three days of treatment. The presence of a scab is indicative of the intense local heat generated by nanoshells within the tumor during laser irradiation; similar blemishes were not seen on mice that received laser irradiation only. The mouse in the second row also received nanoshell-mediated photothermal therapy and is an example of a partial responder, evidenced by initial loss in signal intensity during the first week following

laser irradiation and subsequent reappearance of tumor cell luminescence by day 20 post-irradiation. The third row shows the mouse from the GGS-NP group that experienced the best treatment response (i.e. longest survival time of 24 days) and was a partial responder, and the fourth row shows a mouse from the control group; for mice in the control group the signal intensity and tumor burden increased continually following laser irradiation.

Nanoshell-Mediated Photothermal Therapy Improved Survival

Survival probability was another metric used to evaluate the effectiveness of therapy. **Figure 5.7** is a Kaplan-Meier diagram showing the percentage of mice still alive versus time following laser irradiation for the PEG-NS treatment, PEG-GGS-NP treatment, and laser only control groups. While the mice that received PEG-GGS-NPs did not display improved survival versus the control, the mice that received PEG-NS responded well to treatment. Analysis with a log-rank test revealed that the survival curves for the PEG-NS and laser control groups differed significantly ($p = 0.0155$) and it can be concluded that nanoshell-mediated photothermal therapy significantly improves survival time. Tumors progressed rapidly in the control group and none of the eight mice survived beyond 24 days (mean survival = 13.3 days); similarly, mean survival in the PEG-GGS-NP group was 14.1 days. By comparison, four of seven mice in the nanoshell therapy group survived for the entire 90 day period of study (overall survival = 57%) and each of these mice was completely tumor free without sign of recurrence at that time.

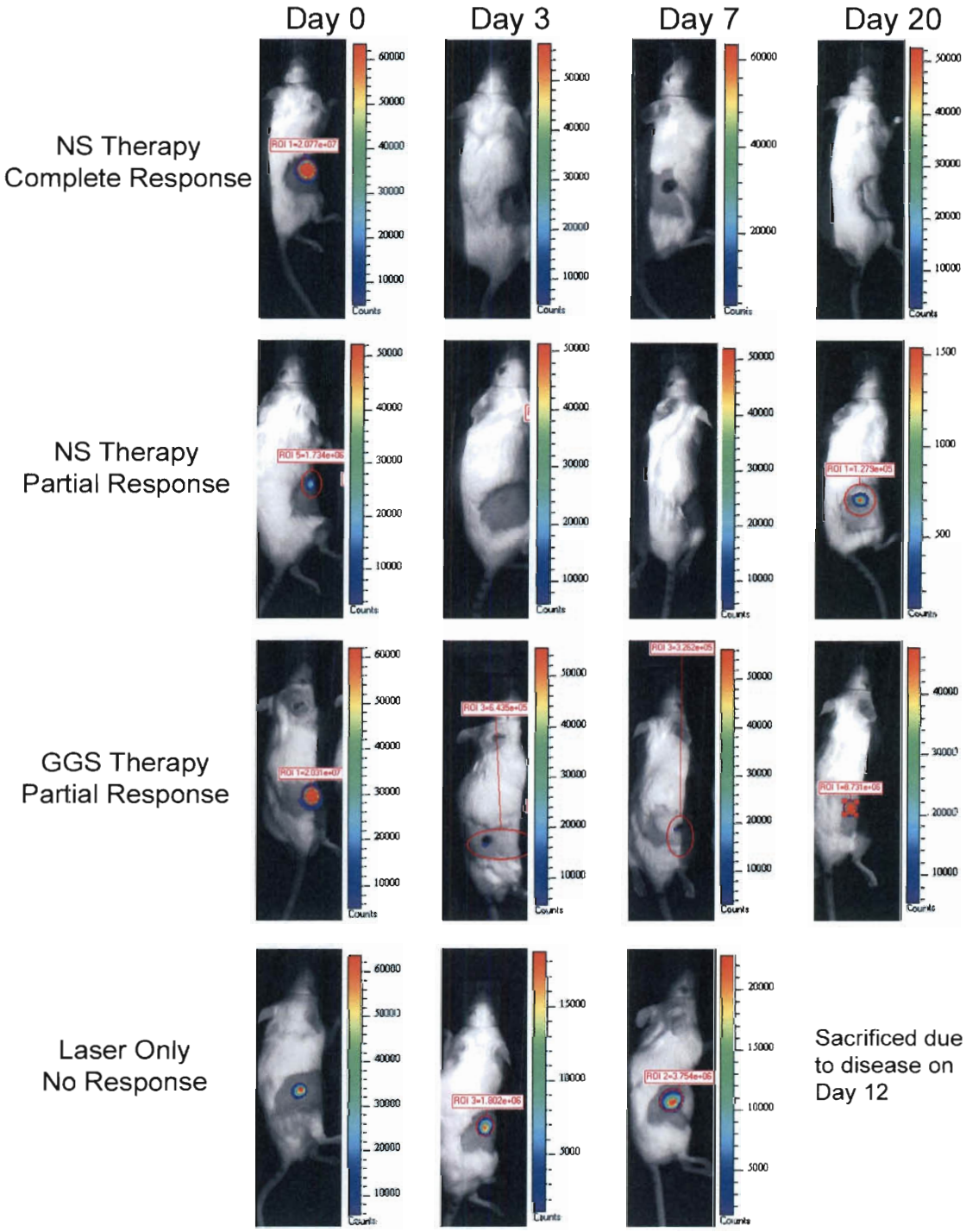

Figure 5.6: Bioluminescent imaging of tumors following laser irradiation. The mouse in the first row displayed loss of luminescence within 3 days of nanoshell therapy and remained tumor-free for the rest of the study. The mice in the second and third rows experienced partial response to therapy with nanoshells or GGS-NPs, respectively, evidenced by initial loss in signal intensity but the tumors later recurred. The fourth row shows a mouse from the control group in which signal intensity and tumor burden increased continually following laser irradiation.

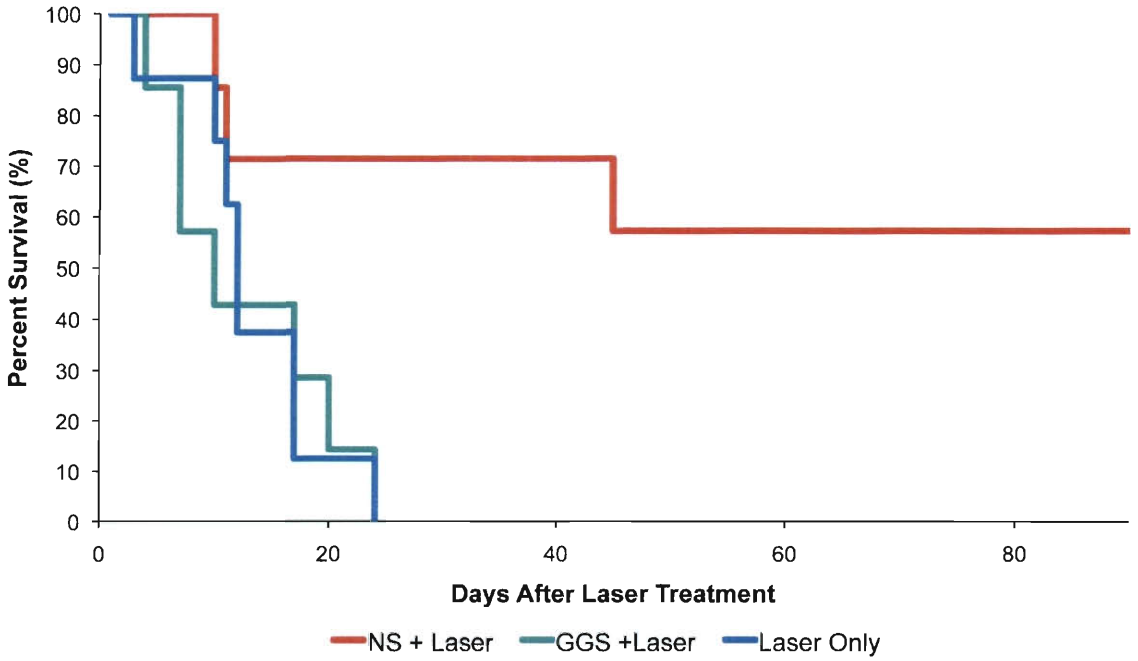

Figure 5.7: Kaplan-Meier survival analysis. Survival versus time for the nanoshell therapy group (red line, n=7), the GGS-NP therapy group (green line, n=7), and the laser control group (blue line, n=8) for the 90 day period of study. None of the mice in the control or GGS-NP group survived beyond 24 days. By comparison, four of seven mice (57%) in the NS treatment group were still alive and tumor-free at day 90 post-laser irradiation. Analysis with a log-rank test revealed a significant improvement in survival with nanoshell-mediated photothermal therapy (p=0.0155).

5.3.5 Discussion

The prognosis for patients with high-grade glioma remains dismal with conventional multi-modality treatment techniques indicating an urgent need for novel therapeutic advances (DeAngelis 2001). Hyperthermia is an attractive therapeutic approach; however, currently available simple heating techniques cannot distinguish normal from diseased tissue. To circumvent this problem, exogenous tumor-targeted heating agents (such as nanoshells, GGS-NPs, nanorods, magnetic nanoparticles, and carbon nanotubes) have been employed to provide specific heating of diseased regions while minimizing

thermal insult to normal tissue. Nanoshell-assisted photothermal therapy has demonstrated effectiveness against a variety of tumors in preclinical studies, with 80–100% survival in murine models of colon carcinoma (O'Neal *et al.* 2004; Gobin *et al.* 2007) and *in vitro* successes against breast (Lowery *et al.* 2006), prostate (Gobin *et al.* 2008), and brain (Bernardi *et al.* 2008) tumor cell lines. The ability to heat nanoshell-laden tumors but not white matter in a canine brain metastasis model has also been reported (Schwartz *et al.* 2009). Gold-gold sulfide nanoparticles have also seen recent *in vitro* (Day *et al.* 2010) and *in vivo* (Gobin *et al.* 2010) success as hyperthermia mediators for breast and prostate tumor lines. The aim of this work was to expand upon previous research by testing these gold-based nanoparticles as a tool for photothermal management of glioma, a highly infiltrative primary brain tumor. The ideal treatment strategy for malignant gliomas is one that produces minimal collateral damage to the surrounding central nervous system structures.

The results shown here suggest that nanoshell-mediated photothermal therapy is an effective method for destruction of glioma *in vivo*. Nanoshell-mediated photothermal therapy resulted in a statistically significant increase in survival, an exciting result given the exceedingly invasive nature of this type of tumor. In addition, it is highly encouraging that more than half of the mice in the nanoshell treatment group displayed complete tumor regression following only one laser treatment, and it is possible that multiple exposures could further increase the therapeutic benefit. Although the GGS-NP group did not display improved overall survival, the IVIS data indicated a partial response so it is likely that optimization of particle dosage and laser parameters could provide a therapeutic benefit with these nanoparticles.

The only side effect to treatment observed in either group was presence of a scab that healed naturally over time, which indicated the extreme heat-producing capability of these nanoparticles. Similar skin changes have been reported during thermal therapy with carbon nanotubes (Moon *et al.* 2009), but this is a relatively minor side effect compared to those from conventional therapy, which can range from chemotherapy-induced nausea to extreme changes in personality or cognitive capacity induced by surgery or radionecrosis. Nevertheless, in the clinical setting it will be necessary to monitor temperature changes during the course of nanoparticle-mediated photothermal therapy in order to prevent unwanted damage to normal brain tissue. This can be accomplished using magnetic resonance thermal imaging, as previously described by Schwartz *et al.* (Schwartz *et al.* 2009). With temperature carefully monitored, magnetic fluid hyperthermia was well-tolerated in a feasibility study reported by Maier-Hauff *et al.* with only minor side effects observed (Maier-Hauff *et al.* 2010), so it is expected that thermal therapy mediated by nanoshells or GGS-NPs would elicit similar responses with minimal side effects.

One advantage of nanoparticles activated by a magnetic field is the ability to treat deeply embedded brain tumors without the need for invasive procedures, as the strength of the applied magnetic field is not attenuated by passage through the body. By comparison, NIR light cannot penetrate the human skull so treatment of human brain tumors with nanoshell-mediated photothermal therapy will likely require use of fiber optic laser probes to deliver the light energy. Very large tumors might require multiple procedures or application of the laser from several directions to ensure damage throughout the tumor volume. While this will increase the invasiveness of the procedure,

it does offer the benefit that laser irradiation (and thus thermal therapy) can be delivered to very specific locations, thereby minimizing off-target effects. Schwartz *et al.* have previously demonstrated the feasibility of using fiber optic probes for nanoshell-mediated thermal therapy of a canine brain tumor model (Schwartz *et al.* 2009). Based on this research, the use of fiber optic probes could feasibly be translated to treatment of glioma. Interstitial light delivery is currently being investigated in an ongoing Phase I clinical trial for treatment of head and neck cancer, and this study will help determine the applicability of this approach (ClinicalTrials.gov 2010). It should be noted that the combined use of directed laser energy and accurate temperature monitoring (such as with magnetic resonance thermal imaging) would help circumvent one of the limitations of hyperthermia, which is lack of control over the vascular environment of the tumor. For example, although increased vessel density would provide enhanced nanoshell deposition, it may also induce more rapid cooling due to blood flow; since effective therapy requires a precise balance of nanoshell dosage and applied laser energy, temperature monitoring during therapy could help guide decisions regarding these parameters to ensure even heat distribution throughout the tumor.

Histology and ICP-MS/NAA revealed that nanoparticles delivered intravenously were selectively located in tumors and not adjacent muscle, which is highly desirable for the minimization of thermal damage to adjacent healthy tissue. Low nanoparticle concentrations were also found in normal brain, which is advantageous since heating of vital areas in this organ should be avoided. Since most highly malignant central nervous system (CNS) tumors have disrupted blood–brain barriers (BBBs) at presentation, nanoparticle penetration into the tumor should be adequate as previously demonstrated by

successful intravenous delivery of PEG-coated nanoshells to intracranial tumors in a canine model (Schwartz *et al.* 2009). In cases where PEG-coated nanoparticles do not extravasate across the BBB at levels sufficient for effective heating, methods to enhance tumor accumulation or to target tumor vasculature will need to be employed.

One goal of these studies was to determine the ability of antibody-coated nanoparticles to target high-grade glioma tumors *in vivo*, since previous *in vitro* work demonstrated that anti-IL13Rα2 coated nanoshells could successfully bind glioma cells and facilitate thermal ablation (Bernardi *et al.* 2008). Contrary to expectations, antibody targeting yielded less nanoparticle accumulation within the tumors than the traditional "stealth" PEG coating. In the future, it would be worthwhile to study whether targeting with antibody fragments without the immunogenic portion would improve these results. The conclusions drawn from this study agree with other recent reports that antibody targeting does not increase nanoparticle concentration within tumors, but it does influence intratumoral localization and cellular internalization of nanoparticles (Kirpotin *et al.* 2006; Choi *et al.* 2010; Huang *et al.* 2010).

A second counter-intuitive result from these studies was that larger silica-gold nanoshells had more tumor accumulation (~50 ppm) than smaller gold-gold sulfide nanoparticles (<10 ppm) (note: for equivalent accumulation, GGS-NPs needed to demonstrate ~35 ppm in the tumor since at equal optical densities a solution of GGS–NPs has ~75% the mass of gold in a solution of NS). However, this result is consistent with a recent paper from Warren Chan's group in which the tumor uptake of gold nanoparticles in the 20-100 nm size regime was elegantly and exhaustively investigated (Perrault *et al.* 2009). They demonstrated that tumor accumulation of 40-100 nm diameter nanoparticles

is exclusively dependent on blood half-life, while for smaller nanoparticles the tumor uptake depends on both half-life and size. Smaller nanoparticles permeate the tumor interstitial space at a higher rate, causing more rapid clearance into surrounding tissue and leading to a lower degree of overall accumulation (Perrault *et al.* 2009). Since the GGS-NPs used in these experiments were roughly 25-35 nm, it is likely that the reduced tumor uptake observed compared to nanoshells is a result of this phenomenon.

No adverse response to nanoshell or GGS-NP presence in the body was observed in the timeframe examined, though the effects of prolonged or repeated exposure remain to be investigated. A few studies have briefly examined safety but the timeframe remains on the order of months. For example, James *et al.* found that nanoshells persist in the body up to 28 days post injection without toxicity (James *et al.* 2007), and O'neal *et al.* reported that mice remain healthy greater than 90 days post therapy (O'Neal *et al.* 2004), consistent with this work. There is currently no evidence that nanoshells or GGS-NPs are degraded by the body and the laser energies used in treatment are much lower than the energy required to break the particles down to their component parts, so it is anticipated that these nanoparticles' long-term compatibility will be largely determined by the surface characteristics and gold has been used clinically for many decades. An initial assessment of nanoshell safety in humans will be gained from the ongoing Phase I clinical trial of nanoshell-mediated photothermal therapy for treatment of head and neck cancer (ClinicalTrials.gov 2010). Given the dismal prognosis and life expectancy for children and adults with high-grade glioma, innovative treatment approaches must be explored and the risk/benefit ratio carefully assessed.

5.4 Conclusions

In summary, the effectiveness of nanoshell-mediated photothermal therapy has been demonstrated against high-grade glioma *in vivo* using a subcutaneous murine tumor model. PEGylated nanoshells delivered intravenously accumulated in subcutaneous tumors at levels sufficient to induce destructive heating of cancerous cells upon transdermal irradiation with a near infrared laser. Treatment led to subsequent tumor regression and improved overall survival versus control mice that received laser irradiation alone. These results warrant further investigation of nanoshell-mediated photothermal therapy for treatment of primary brain tumors and studies using orthotopic tumor models will be discussed in Chapter 6. Since anti-IL13Rα2 targeting proved ineffective using a subcutaneous tumor model, in Chapter 6 the ability of nanoshells to treat intracranial tumors by targeting and disrupting tumor vasculature is investigated. These orthotopic models are critical for validation of the technique not only because of need to verify nanoshell accumulation in intracranial tumors, but also because microenvironment plays a critical role in tumor cell behavior and may influence response to treatment. In addition, these studies help elucidate whether adjustments need to be made to particle concentration or laser parameters to accommodate for attenuation of light as it passes through the normal brain prior to reaching the tumor. In the future, this novel approach to cancer therapy could yield a promising alternative to conventional treatment modalities.

Chapter 6: Treatment of Intracranial Tumors with Vascular-Targeted Nanoparticles

6.1 Introduction

Angiogenesis plays a critical role in tumor development, and high-grade gliomas are among the most densely vascularized tumors. Consequently, there has been a surge in the development of anti-angiogenic therapies for treatment of malignant glioma. Several excellent reviews of vascular-targeted therapy have been published (see (Chamberlain 2008) and (Tuettenberg *et al.* 2006) for discussions of anti-angiogenic glioma therapy, or (Ruoslahti *et al.* 2010) for information about vascular-targeted nanoparticles). While this relatively new approach to treating malignant brain tumors has been greeted with much enthusiasm, a thorough review of the literature shows that anti-angiogenic strategies currently used clinically suffer two major drawbacks. First, most therapies are cytostatic, requiring long-term continuous treatment. Second, as will be discussed in more detail later, many treatments suffer from development of cellular resistance. In this chapter, the ability to disrupt glioma tumor vasculature with nanoparticle-mediated photothermal therapy is investigated as a means to build upon the successes and overcome the limitations of other anti-angiogenic therapies.

The vascular endothelial growth factor (VEGF) signaling pathway has been identified as a key regulator of angiogenesis and VEGF receptor-2 (VEGFR-2) is highly expressed in glioma endothelium (Plate *et al.* 1994). Therefore, in this thesis, nanoshells and gold-gold sulfide nanoparticles were coated with VEGF to facilitate binding with VEGFR-2. *In vitro* experiments confirmed the ability of VEGF-coated nanoparticles to

bind VEGFR-2 expressing endothelial cells and facilitate thermal ablation of these cells. Subsequent *in vivo* studies performed with a clinically relevant intracranial tumor model verified that systemically delivered vascular-targeted nanoparticles accumulate in orthotopic glioma tumors at levels sufficient to disrupt tumor vasculature upon near-infrared laser irradiation.

6.1.1 Advantages of Targeting Brain Tumor Vasculature

The idea that tumors are angiogenesis-dependent was proposed forty years ago (Folkman 1971), and since then a variety of therapies targeted towards tumor vasculature have been developed. The rationale in support of anti-angiogenic therapy is multi-fold. First, areas of increased vascular permeability are spatially non-uniform in tumors, leading to irregular blood flow, edema, and high interstitial pressures. These factors hinder the delivery of therapeutic agents to the tumor interstitial space via the enhanced permeability and retention effect. Targeting markers selective for tumor vessels avoids delivery difficulties since luminal endothelial cells are readily accessible to compounds in circulation and tissue penetration is not required for the therapeutic agent to reach its target (Chamberlain 2008; Ruoslahti *et al.* 2010). This accessibility is particularly important for treatment of brain tumors since difficulty crossing the blood-brain barrier has limited the efficacy of many drugs. A second benefit of targeting tumor vessels is that the genetic and molecular changes that occur in tumor-associated endothelial cells are consistent across multiple tumor lineages, and therefore a single agent may be effective against several different diseases. The final rationale in support of anti-angiogenic therapy is that endothelial cells are relatively genetically stable and therefore less likely to develop resistance than tumor cells; however, recent evidence suggests that

if only one angiogenic pathway is inhibited, cells may compensate by signaling through an alternative pathway or by invading farther into the normal brain (Tuettenberg *et al.* 2006; Keunen *et al.* 2011). Thus, new therapeutics must be carefully evaluated to confirm complete disruption of targeted cells.

Most anti-angiogenic therapies aim to disrupt tumor vasculature so that subsequent reduction in nutrient and oxygen transport will result in tumor necrosis. Another therapeutic approach is vascular "normalization", which aims to correct the structure and function of tumor vessels (Jain 2005). Normalization is predicted to improve chemotherapy by reducing interstitial pressure, thereby increasing overall drug content within the tumor and equalizing drug distribution throughout the tumor. Normalization should also heighten tumor oxygenation, sensitizing cells to both chemotherapy and radiation therapy. However, a recent study investigating the effect of Bevacizumab, an antibody against vascular endothelial growth factor (VEGF) approved by the Food and Drug Administration for second-line treatment of glioblastomas, on intracranial tumors in rats found that "a 'morphological' normalization of the vascular bed is not necessarily accompanied by a 'functional' normalization of the vascular supply" (Keunen *et al.* 2011). In fact, contrary to the hypothesis of normalization, it was observed that Bevacizumab treatment resulted in a more hypoxic tumor environment. Furthermore, this hypoxia promoted a metabolic change in tumor cells toward glycolysis that led to increased tumor cell invasion into the normal brain (Keunen *et al.* 2011). From the results of this study, it is apparent that vascular normalization needs to be more carefully assessed to determine its utility in treatment of brain tumors.

There are several potential targets for vascular-focused therapies, including α_v integrins and angiogenic growth factor receptors and their ligands (Choudhury *et al.* 2010). In preliminary studies in tumor-bearing mice, conjugating doxorubicin to peptides with integrin-binding motifs, such as RGD, increased efficacy and decreased toxicity versus mice treated with non-targeted doxorubicin (Arap *et al.* 1998). In a separate study reported by the Cheresh group, when doxorubicin was encapsulated in liposomes coated with cyclic RGD peptides there was a marked reduction in tumor metastasis (Murphy *et al.* 2008). Additional targets for anti-angiogenic therapy include the growth factor receptors EGFR (epidermal growth factor receptor), PDGFR (platelet-derived growth factor receptor), and VEGFR (vascular endothelial growth factor receptor), and these have been targeted primarily with antibodies or small molecule inhibitors (Choudhury *et al.* 2010). In the next section, utilizing VEGF and VEGFR as a targeting strategy will be discussed in detail since this ligand/receptor pair is the most important for glioma angiogenesis and has thus received the most focus amongst developing therapeutics (Reardon *et al.* 2008; Miletic *et al.* 2009).

6.1.2 Vascular Endothelial Growth Factor as a Targeting Strategy

Vascular endothelial growth factor (VEGF) and its receptors are key regulators in the development and progression of glioma. VEGF is a tumor-secreted cytokine that exerts its effect by interacting with the transmembrane tyrosine kinase receptors VEGF receptor-1 (VEGFR-1; also known as Flt-1) and VEGFR-2 (also known as Flk-1 or KDR), expressed on vascular endothelial cells, and the neuropilin receptor expressed on vascular endothelium and neurons. When VEGF binds the extracellular domain of VEGFR-2, the main receptor involved in tumor angiogenesis, it leads to receptor

dimerization and intracellular receptor autophosphorylation that promotes downstream signaling in favor of endothelial cell proliferation, migration, and survival (**Figure 6.1**) (Rini and Small 2005). For a more thorough discussion of the biology of VEGF and its receptors, the following review articles are recommended: (Dvorak 2002; Cross *et al.* 2003; Ferrara *et al.* 2003).

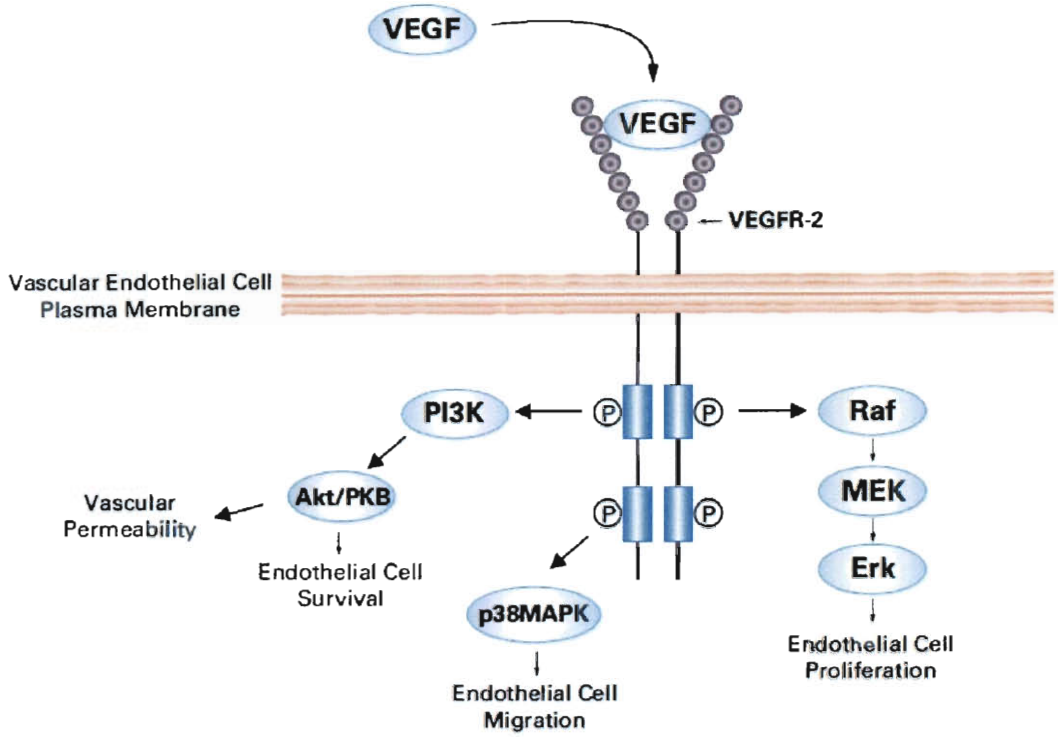

Figure 6.1: A simplified schematic of the VEGF signaling cascade. Binding of VEGF to VEGFR-2 results in dimerization and autophosphorylation of the intracellular receptor tyrosine kinases. This activates several pathways that promote endothelial cell survival, proliferation, and migration, resulting in increased angiogenesis. Figure from Rini and Small 2005.

VEGF's paracrine effects between a brain tumor mass and its vasculature have been known for some time, but recently an additional autocrine effect of VEGF has been reported (Knizetova *et al.* 2008). In their paper, Knizetova *et al.* used RT-PCR to demonstrate that VEGF and its receptors are co-expressed in a variety of human brain

tumor cell lines (2008). Then, through a series of experiments it was shown that this co-expression yields autocrine signaling that enhances tumor cell growth and viability; furthermore, inhibition of VEGFR-2 with a small molecule led to the conclusion that VEGFR-2 is the major mediator of these effects (Knizetova *et al.* 2008). Thus, novel therapeutics could aim to disrupt both paracrine and autocrine signaling pathways.

Currently, monoclonal antibodies are the main form of anti-VEGF/VEGFR therapy. While some groups have attempted immunotherapy of glioma with only a single antibody targeting VEGFR-2 (Kunkel *et al.* 2001) or VEGF (Keunen *et al.* 2011), most have focused on using antibodies against multiple targets in combination. These include antibodies against VEGFR-2 and EGFR (Yi *et al.* 2010); against VEGF and VEGFR-1 (Stefanik *et al.* 2001); and against VEGFR-2, EGFR, and cadherin (Lamszus *et al.* 2005). The advantage of using multiple targets, as mentioned above, is that it minimizes potential for cells to compensate through alternative angiogenic pathways.

This chapter introduces a novel approach to anti-angiogenic cancer therapy with vascular-targeted nanoparticles. Here, nanoparticle-mediated photothermal therapy is used to disrupt tumor vasculature; this physical disruption should be less susceptible to the cellular escape mechanisms that have troubled other anti-angiogenic therapies. Nanoshells and gold-gold sulfide nanoparticles were coated with $VEGF_{165}$, the most common isoform of VEGF, and *in vitro* studies demonstrated these nanoparticles can bind to VEGFR-2 positive endothelial cells. Then, distribution and survival studies were performed using intracerebral U373 tumors. It was critical to assess therapeutic efficacy using an intracerebral tumor model for a number of reasons. First, microenvironment influences cancer cell behavior, so studying the effect of therapy on tumors in their

natural setting is more clinically relevant than the subcutaneous model used in Chapter 5. Second, the intracranial model allows effects of therapy on the normal brain to be assessed; any new treatment for brain tumors must minimize damage to the normal brain to ensure the best possible quality of life for patients following therapy.

The ability of VEGF-coated and PEG-coated nanoparticles to be systemically delivered to intracranial U373 tumors was confirmed with ICP-MS. Interestingly, this cell line is one of the glioma types found by Knizetova *et al.* to express VEGFR-2 (Knizetova *et al.* 2008), so VEGF-coated nanoparticles could potentially bind both tumor-associated endothelial cells and the tumor cells themselves. Although this dual-targeting ability was not directly evaluated in this thesis it does provide potential for multimodal therapy in which the photothermal effect could be exerted on both the tumor mass and on the tumor vasculature simultaneously.

Based on the distribution data, photothermal therapy experiments were performed using nanoshells but not gold-gold sulfide nanoparticles. For these experiments, tumor implantation was performed using the method of Gaber *et al.* in which a cranial window was placed over the tumor (2004). This glass window served two purposes: (1) it allowed laser light to be delivered to the tumor, and (2) it allowed changes in tumor vasculature following therapy to be monitored with intravital microscopy. Analysis of intravital microscopy images taken just prior to laser exposure and again three days later revealed that vessel density decreased over time in mice treated with VEGF-coated nanoshells but increased in mice treated with saline. Additionally, histology of mice sacrificed immediately following laser exposure showed regions of vascular damage in

the tumor but not in the normal brain of mice that received VEGF-coated nanoshells. Ultimately, vascular-targeted therapy led to a slight improvement in animal survival.

6.2 Materials and Methods

6.2.1 Nanoparticle Preparation and Characterization

Nanoshells and gold-gold sulfide nanoparticles prepared by the methods introduced in Chapter 2 were coated with mPEG-SH +/- OPSS-PEG-VEGF. OPSS-PEG-VEGF was synthesized via the same chemistry for antibody-PEG coupling shown in Figure 3.2, where "R" is now VEGF with available primary amines. OPSS-PEG-NHS (Creative PEGWorks, Winston Salem, NC) reacted at a 10:1 molar ratio with murine $VEGF_{165}$ (PeproTech, Rocky Hill, NJ) at 4°C overnight. Conjugation was confirmed via silver staining on proteins separated by polyacrylamide gel electrophoresis (SDS-PAGE; 4-15% Tris-HCl precast gels and silver stain from Bio-Rad, Hercules, CA).

VEGF-coated nanoparticles were prepared by reacting nanoparticles suspended in milli-Q water (OD=1.5) with OPSS-PEG-VEGF for 1 h at 4°C. GGS-NPs received 100 OPSS-PEG-VEGF per nanoparticle and NS received 1500 OPSS-PEG-VEGF per nanoparticle. Following coupling, nanoparticles incubated with mPEG-SH (5 kDa, Laysan Bio, Arab, AL) overnight at 4°C; GGS-NPs received 1 part 250 μM mPEG-SH to 9 parts nanoparticles and NS received 1 part 25 μM mPEG-SH to 9 parts nanoparticles. Control nanoparticles were also prepared with only mPEG-SH (no VEGF). Following VEGF and/or PEG modification, nanoparticles were purified and concentrated with cross flow filtration using 11 cm^2 polysulfone filters with 0.05 μm MWCO (MicroKros

Modules, Spectrum Laboratories, Inc., Rancho Dominguez, CA). Following concentration, samples were suspended in sterile phosphate buffered saline (PBS).

To confirm and quantify the presence the VEGF on nanoparticles, dynamic light scattering, Zeta potential measurements, and the modified ELISA were performed as described in earlier sections of this thesis. For the ELISA, nanoparticles were first incubated with 100 μg/ml rabbit anti-murine VEGF (PeproTech), then with 200 μg/ml HRP-conjugated anti-rabbit IgG (Sigma). All other aspects of the analysis remain the same as described in Chapters 3, 4, and 5. Salt stability tests were also performed to confirm adequate PEG-SH coverage.

6.2.2 *In Vitro* Assessment of Vascular-Targeted Photothermal Therapy

Initial *in vitro* experiments were performed to confirm that VEGF-coated nanoparticles could bind VEGFR-2 positive cells and facilitate thermal therapy of these targeted cells. MS1 (Mile Sven 1) murine endothelial cells, which express VEGFR-2, were obtained from ATCC and cultured in Dulbeco's Minimum Essential Medium (DMEM) supplemented with 10% fetal bovine serum and 1% GPS (L-glutamine, penicillin, and streptomycin). Cells grown in chambered coverglass were exposed to 1 ml saline, 1 ml PEG-coated nanoparticles (OD=4), or 1 ml VEGF-coated nanoparticles (OD=4). After rinsing three times to remove unbound particles, an 808 nm laser was applied at 60 W/cm^2 for 3 min. Following a 1 h incubation period, samples were stained with 1 μM calcein AM and 4 μM ethidium homodimer-1 (Live/Dead staining kit, Molecular Probes) and fluorescence microscopy was performed with an inverted Zeiss Axiovert 135 phase contrast microscope to investigate cell viability. Samples were also imaged with

darkfield microscopy using a Cytoviva adaptor on the same microscope to assess nanoparticle binding to the cells.

6.2.3 Tumor Inoculation and Cranial Window Placement

Following the *in vitro* assessment of vascular-targeted photothermal therapy, *in vivo* models were used to study nanoparticle accumulation in intracranial tumors and to evaluate the ability of these nanoparticles to facilitate disruption of tumor vasculature with photothermal therapy. All animals were used under an approved protocol of the Institutional Animal Care and Use Committee of Baylor College of Medicine. These *in vivo* experiments used the same U373 human high-grade glioma cell line discussed in Chapter 5. The cells were engineered to constitutively express both the firefly luciferase gene (FFLuc) and green fluorescent protein (GFP) as previously described (Ahmed *et al.* 2007). This dual expression enabled tumor growth to be monitored *in vivo* with intravital microscopy to observe the GFP signal or with the Xenogen IVIS 100 bioluminescence imaging system (Caliper Life Sciences) to observe the luciferase activity.

U373 cells were maintained in RPMI 1640 medium (Invitrogen Corp., Carlsbad, CA) supplemented with 1% glutamine and 10% fetal bovine serum and cultured at 37°C in a 5% CO_2 environment. Cells were detached from culture flasks with trypsin-EDTA and diluted in culture media to 5×10^7 cells/ml for inoculation into mice. For the nanoparticle distribution study, mice were anesthetized with 50 mg/kg Nembutal (sodium pentobarbital) solution delivered intraperitoneally. The fur over the scalp was removed with a razor and the surgical area cleaned with alcohol. An incision was cut in the skin 1 mm lateral right to the middle sagittal suture and 2 mm anterior of the lambdoid suture, then a microsurgical drill was used to create an 0.8 mm diameter Burr hole in the skull.

Using a Hamilton syringe, 2 µl cell suspension was injected 3 mm deep into the right cerebrum of male IcrTac:ICR-Prkdc^{SCID} mice (Taconic Farms, Hudson, NY) for a total injection of 10^5 U373 cells. The wound was closed with surgical glue and tumor development was monitored daily with bioluminescent imaging.

For treatment studies, tumors were implanted using the cranial window procedure described by Gaber *et al.* (2004). The day before surgery, the fur over the scalp was removed with hair removal cream. For surgery, each mouse was anesthetized with sodium pentobarbital (50 mg/kg, i.p. delivery), the animal's head placed in a sterotaxic frame and its body placed on a heating mat to maintain body temperature throughout the procedure. The surgical area was cleaned with alcohol and Betadine, and eye ointment was applied to the eyes with a sterile cotton swab. Using fine scissors, the scalp over the parietal cortex was removed to reveal the sagittal and lambdoid sutures and the fascia was removed from the skull with forceps to leave a dry surface for drilling. With a microsurgical drill, a rectangular cranial window (approximately 4-5 mm width and length) was made; final breakthrough of the skull was accomplished with fine forceps. Once the brain was exposed, artificial cerebral spinal fluid (aCSF) was applied frequently. The aCSF is composed of 0.22 g KCl, 0.305 g $MgCl_2 \bullet 6H_2O$, 0.264 g $CaCl_2$, 7.71 g NaCl, 0.402 g urea, 0.665 g dextrose, and 2.066 g $NaHCO_3$ in one liter of Millipore H_2O. Using a Hamilton syringe, 2 µl cell suspension (10^5 cells total) was slowly injected 3 mm deep into the right cerebrum, 1 mm lateral of the middle sagittal suture and 2 mm anterior of the lambdoid suture. Then, a glass cranial window was placed over the exposed cerebral cortex and fixed to the surrounding skull with cyanoacrylate glue. The tumor implantation site (red dot) and cranial window are

depicted schematically in **Figure 6.2**. After surgery, mice received intraperitoneal injections of 0.2 mg/kg buprenorphine (Buprenex) every 12 hours for 2 days to minimize pain. In addition, the mice were given antibiotics in their water for 5 days following surgery to prevent onset of infection (1.7 ml Baytril 100 (enrofloxacin, 100 mg/ml stock solution) per 400 ml H_2O).

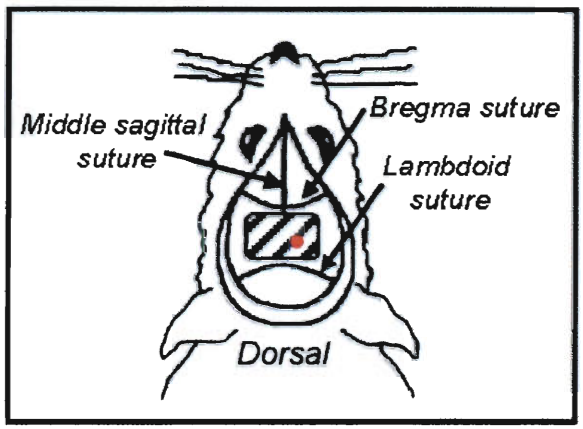

Figure 6.2: Tumor inoculation and cranial window placement. Tumor cells are implanted 3 mm below the surface of the brain at the position 2 mm anterior to the lambdoid suture and 1 mm lateral to the middle sagittal suture, as indicated by the red circle. Then a glass cranial window (depicted as a black and white box) is sealed over the opening. Image modifed from Gaber 2004.

6.2.4 Analysis of Nanoparticle Accumulation in Intracranial Tumors

It was necessary to determine whether intravenously administered nanoparticles could accumulate in orthotopic tumors. As discussed in Chapter 5, tumor size correlates with bioluminescence signal intensity and preliminary studies demonstrated that tumor diameter was 3-5 mm when tumor signal was above 10^6 units for 3 days. Based on these criteria, when tumor diameter reached 3-5 mm, mice received intravenous injections of 100 µl PEG-coated or VEGF-coated nanoshells (1.7×10^{11} particles/ml) or GGS-NPs (1.1×10^{13} particles/ml). These concentrations correlate to equal optical densities (OD=60) of the nanoparticle formulations. After waiting 6, 24, or 48 h the mice were

euthanized and tissue was collected for analysis of gold content by ICP-MS. Tissue studied included spleen, liver, blood, kidney, heart, tumor, and normal brain. Three mice were used per group per timepoint, for a total of 36 mice.

6.2.5 Verification of VEGF Receptor Expression in Orthotopic Tumors

VEGFR-2 expression in tumor tissue was confirmed with immunofluorescent staining. Paraffin-embedded tissue cut into 6 μm sections incubated in xylene twice for 10 min before hydrating through a series of alcohol (100%, 90%, 70%, 50%) and water. Slides incubated in proteinase K (10 μg/ml, 37°C, 15 min) and were cooled with running water for 3 min. After rinsing with PBS containing 0.05% Tween20 (PBST), non-specific binding sites were blocked with 10% donkey serum in PBS for 45 min. Samples then reacted with rat anti-mouse VEGFR-2 (15 μg/ml, R&D Systems) and goat anti-mouse CD31 (15 μg/ml, R&D Systems) overnight at 4°C. Three rinses with PBST were performed and then samples were exposed to AlexaFluor 594-conjugated donkey anti-rat IgG (10 μg/ml, Invitrogen) and AlexaFluor 488-conjugated donkey anti-goat IgG (10 μg/ml, Invitrogen) for 1 h. Rinsed sections were mounted with Vectashield containing DAPI and imaged.

6.2.6 Photothermal Therapy of Intracranial Brain Tumors

Photothermal therapy of intracranial glioma tumors was attempted using nanoshells but not gold-gold sulfide nanoparticles since nanoshells demonstrated higher intratumoral gold content according to ICP-MS. Mice received intravenous injections of 150 μl nanoshells and after 24 h the near-infrared laser was applied for 3 min through the cranial window. Response to treatment was monitored with intravital microscopy and

bioluminescence imaging, and mice were euthanized by carbon dioxide asphyxiation when one of the following two criteria was reached: (1) if mouse weight reduced by 20% from the day of tumor implantation; (2) if the animal was moribund, unable to eat or move, or showing other signs of neurologic deficits (such as limb paralysis, huddled posture, etc.). For the survival study, mice received 150 μl nanoshells at OD=100 (2.9×10^{11} particles/ml) and the laser fluence was 6 W/cm^2 (power = 1 W, ~4.5 mm beam diameter). Three mice received PEG-NS, three mice received VEGF-NS, and three mice received saline.

To quantify changes in vasculature induced by treatment, intravital microscopy images acquired on the day of laser application (Day 0) and three days later were analyzed for three mice that received VEGF-coated nanoshells and three mice that received saline. Mice that received PEG-coated nanoshells could not be included in the analysis since only 1 mouse survived to three days; it remains to be investigated in future studies why the mice that were treated with PEG-coated nanoshells did not survive longer. For the analysis, vessels within 1.5 mm from the tumor center were traced in ImageJ software (NIH), filled, and the image was binarized; this process is shown in **Figure 6.3** for a sample image acquired on Day 0. Vessel density was calculated as the area of positive pixels divided by the total area and the density on Day 3 was normalized to the density on Day 0 to quantify treatment effect. Lastly, treatment effect was also monitored with histology. A subset of mice was euthanized immediately following laser exposure and brain tissue was excised for hematoxylin and eosin (H&E) staining. These tissue samples were carefully evaluated to determine the effects of therapy on both the tumor and the normal brain. Additional sections from two of these mice were also

stained to detect CD31 as described above and imaged by fluorescence and darkfield microscopy to determine the proximity of nanoshells to tumor vessels.

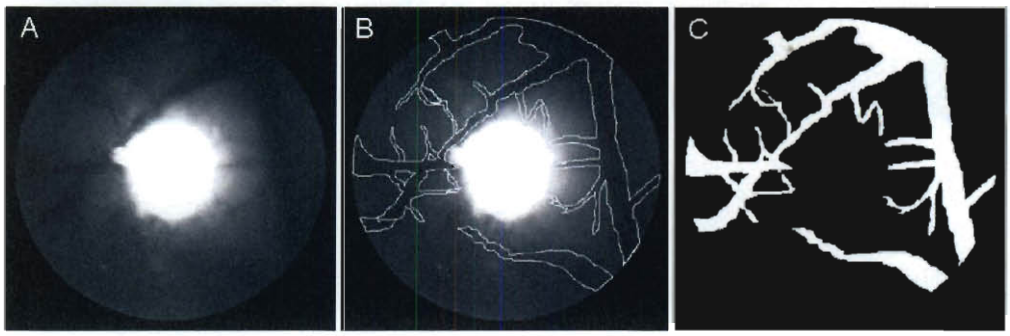

Figure 6.3: Preparing intravital microscopy images for vessel density analysis. (A) A region of interest (ROI) within 1.5 mm from the tumor center is encircled. (B) Vessels within the ROI are outlined. (C) Outlined vessels are filled and the image is binarized. The tumor signal is removed so all that remains is a trace of vessels.

6.3 Results and Discussion

6.3.1 Nanoparticle Characterization

Silver staining of PEG-VEGF protein samples separated by SDS-PAGE confirmed the conjugation of VEGF to OPSS-PEG-NHS. As shown in **Figure 6.4**, addition of OPSS-PEG-NHS caused an increase in observed molecular weight, with several bands appearing based on the number PEG chains added. VEGF appears as a 19 kDa monomer due to the reducing conditions used to prepare the gel.

For the biodistribution study, nanoparticles were characterized with the ELISA: GGS-NPs were coated with 62.7 ± 7.6 VEGF per nanoparticle and nanoshells were coated with 100.9 ± 14.3 VEGF per nanoparticle. For the survival study, only nanoshells were used and these were characterized even further with DLS, Zeta potential, and the ELISA, which indicated 332.1 ± 112.1 VEGF per nanoparticle. DLS and Zeta potential

measurements showed increased hydrodynamic diameter and neutralized surface charge upon functionalization, respectively (**Table 6.1**).

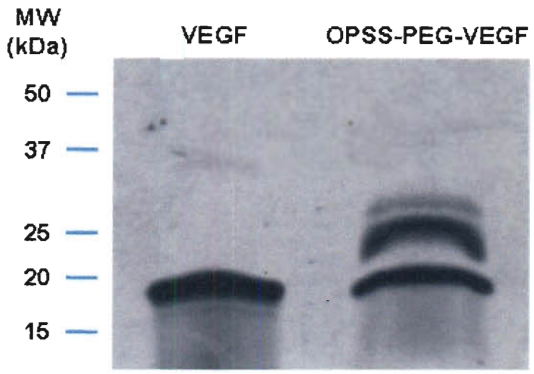

Figure 6.4: SDS/PAGE confirms OPSS-PEG-NHS conjugation to VEGF. Silver staining showed that molecular weight of the product increased upon conjugation of VEGF to OPSS-PEG-NHS (2000 Da), with separate bands appearing based on the number of PEG chains attached. The reaction included a 10:1 PEG to VEGF molar ratio.

Sample Type	Hydrodynamic Diameter (nm)	Zeta Potential (mV)
Bare NS	162.4 ± 2.0	-57.9 ± 0.6
PEG NS	188.0 ± 1.2	-33.4 ± 0.4
VEGF NS	196.8 ± 7.0	-32.7 ± 1.3

Table 6.1: Characterization of VEGF-coated nanoshells. DLS and Zeta potential measurements demonstrated that hydrodynamic diameter increased and Zeta potential magnitude decreased upon functionalization with PEG or VEGF.

6.3.2 VEGF-Coated Nanoparticles Bind Murine Endothelial Cells *In Vitro* to Facilitate Thermal Therapy

The ability of VEGF-coated nanoparticles to bind murine endothelial cells that over-express VEGFR-2 and facilitate thermal therapy was first tested *in vitro*. Darkfield microscopy confirmed the hypothesis that VEGF-coated GGS-NPs and NS could bind MS1 cells, while PEG-coated nanoparticles could not bind the cells and were removed during the rinsing steps (**Figure 6.5**). GGS-NPs and NS appear red under darkfield microscopy due to their light-scattering properties. Upon NIR-irradiation, only MS1

cells that had been exposed to targeted (VEGF-coated) nanoparticles experienced loss in viability, indicated by red EthD-1 fluorescence (**Figure 6.5**). Comparatively, cells previously exposed to saline or PEG-coated nanoparticles remained viable (green calcein AM fluorescence). These results suggested that VEGF-coated nanoparticles are a promising agent for vascular-targeted therapy worthy of further *in vivo* assessment.

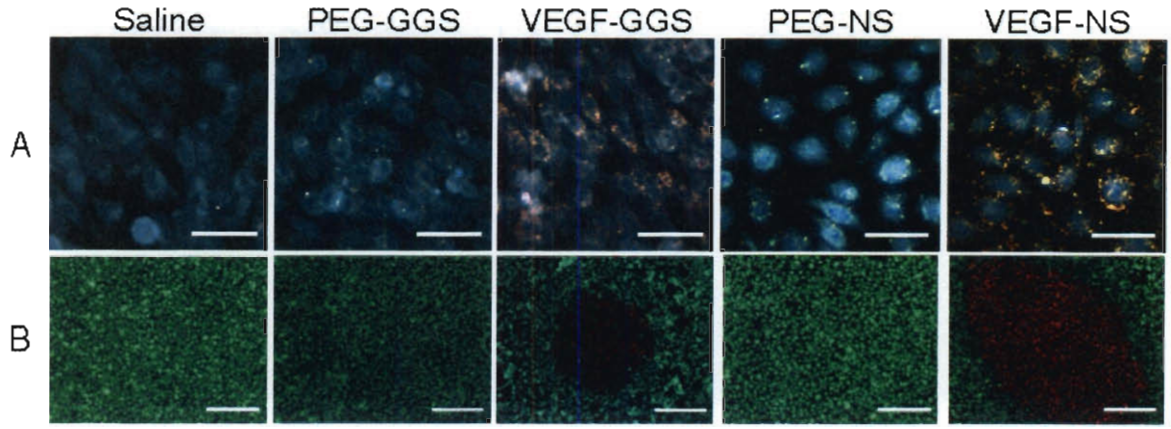

Figure 6.5: VEGF-coated nanoparticles bind MS1 cells *in vitro* to mediate thermal ablation. (A) Darkfield microscopy proves that VEGF-coated nanoparticles bind MS1 cells that express VEGFR-2, while PEG-coated nanoparticles do not. Nanoparticles are red against the blue cell background. Scale bars = 50 μm. (B) Fluorescence microscopy reveals that only cells treated with VEGF-coated nanoparticles experience loss in viability upon laser irradiation. Live cells fluoresce green (calcein AM) and dead cells fluoresce red (EthD-1). Scale bars = 400 μm.

6.3.3 VEGF Receptor Expression in Orthotopic U373 Tumors

Immunofluorescence confirmed presence of the target receptor (VEGFR-2) in the tumor vasculature (**Figure 6.6**). VEGFR-2 (red fluorescence) was present on endothelial cells, which also stained positively for CD31 (green fluorescence). Hence, based on the *in vitro* binding assessment, VEGF-coated nanoparticles should be able to target tumor-associated vessels *in vivo.*

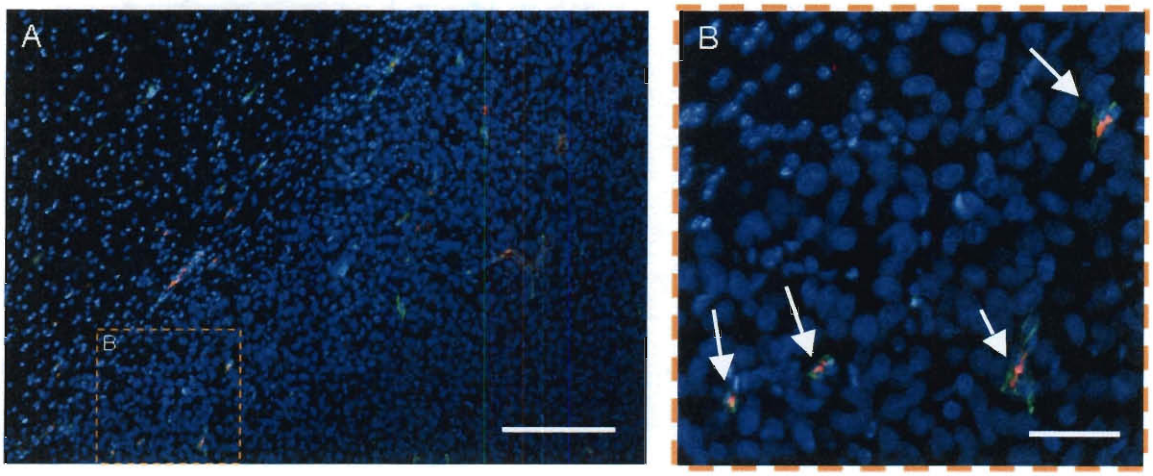

Figure 6.6: Fluorescence microscopy confirms VEGFR-2 expression in intracranial U373 tumors. This tissue section was stained to show CD31 (green), VEGFR-2 (red), and nuclei (blue). The border between the tumor and the normal brain is shown in (A) and a higher magnification of a region in the tumor (orange outline) is shown in (B) to demonstrate that VEGFR-2 co-localizes with CD31 (indicated by white arrows). Scale bar = 200 μm in (A) and 50 μm in (B).

6.3.4 VEGF-Coated and PEG-Coated Nanoparticles Accumulate in Intracranial Tumors

Using inductively coupled plasma-mass spectrometry (ICP-MS), the mean and standard deviation of gold content in each organ was calculated from three mice per group after nanoparticles circulated for 6, 24, and 48 hours, and the distribution trends for PEG-coated nanoparticles agreed with those observed in Chapter 5 (**Figure 6.7**). The organs analyzed included spleen, liver, kidney, blood, heart, tumor, and normal brain. Kidney and heart were added to the analysis since anti-vascular therapies such as Bevacizumab have been linked to proteinuria and hypertension (Zhu *et al.* 2007). Coating (PEG or VEGF) did not influence nanoparticle accumulation in the kidney, but more gold was found in the heart for both gold-gold sulfide nanoparticles and nanoshells when the particles were coated with VEGF. This finding underscores the need to carefully monitor the effects of VEGF-coated nanoparticles on the heart as this therapy is developed.

Addition of VEGF to nanoparticles reduced gold accumulation in the spleen and increased gold accumulation in the liver, likely because the liver is highly vascularized; this effect was more pronounced for NS than for GGS-NPs. Finally, nanoparticles with VEGF coatings were more rapidly removed from the blood than those with PEG coatings, perhaps because of increased adherence to vessel walls.

Figure 6.8 shows expanded graphs for the tumor and normal brain samples. Importantly, for both GGS-NPs and NS, more nanoparticles were found within the tumor than in the normal brain at all times. These differences were tested for significance using a student's t-test and samples with $p<0.05$ are marked. It is critical to apply the laser when the difference in nanoparticle content between the tumor and the normal brain is maximized so the potential for off-target effects is minimized. Based on this criterion, it was decided that the survival study would include only nanoshells since they showed a more consistent pattern of tumor accumulation than the GGS-NPs. In addition, nanoshells require much less VEGF to constitute an equal surface coverage on GGS-NPs, reducing the overall cost of the treatment. In the survival study, a higher dose of nanoshells was delivered through the tail vein (4.35×10^{10} nanoshells per mouse), with the prediction that more particles would accumulate in the tumor, and the NIR laser was applied 24 h post-intravenous injection.

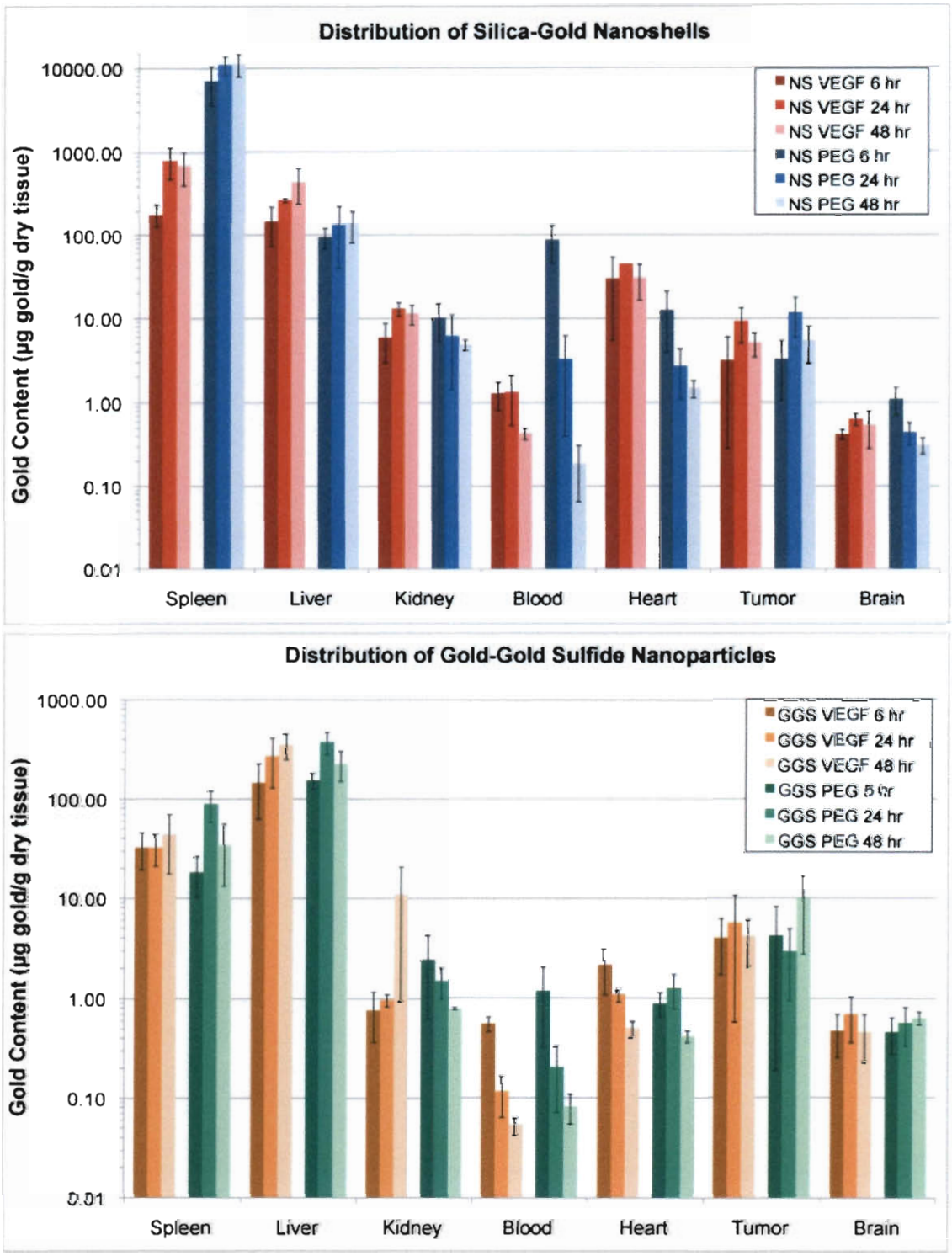

Figure 6.7: Distribution of VEGF-coated and PEG-coated nanoparticles. The accumulation of nanoparticles in several organs was determined by ICP-MS. In the top chart VEGF-NS are red and PEG-NS are blue. Similarly, in the bottom chart VEGF-GGS-NPs are orange and PEG-GGS-NPs are green. Color intensities are lighter for later times. Data depicts mean ± standard deviation for n=3 samples for all sets.

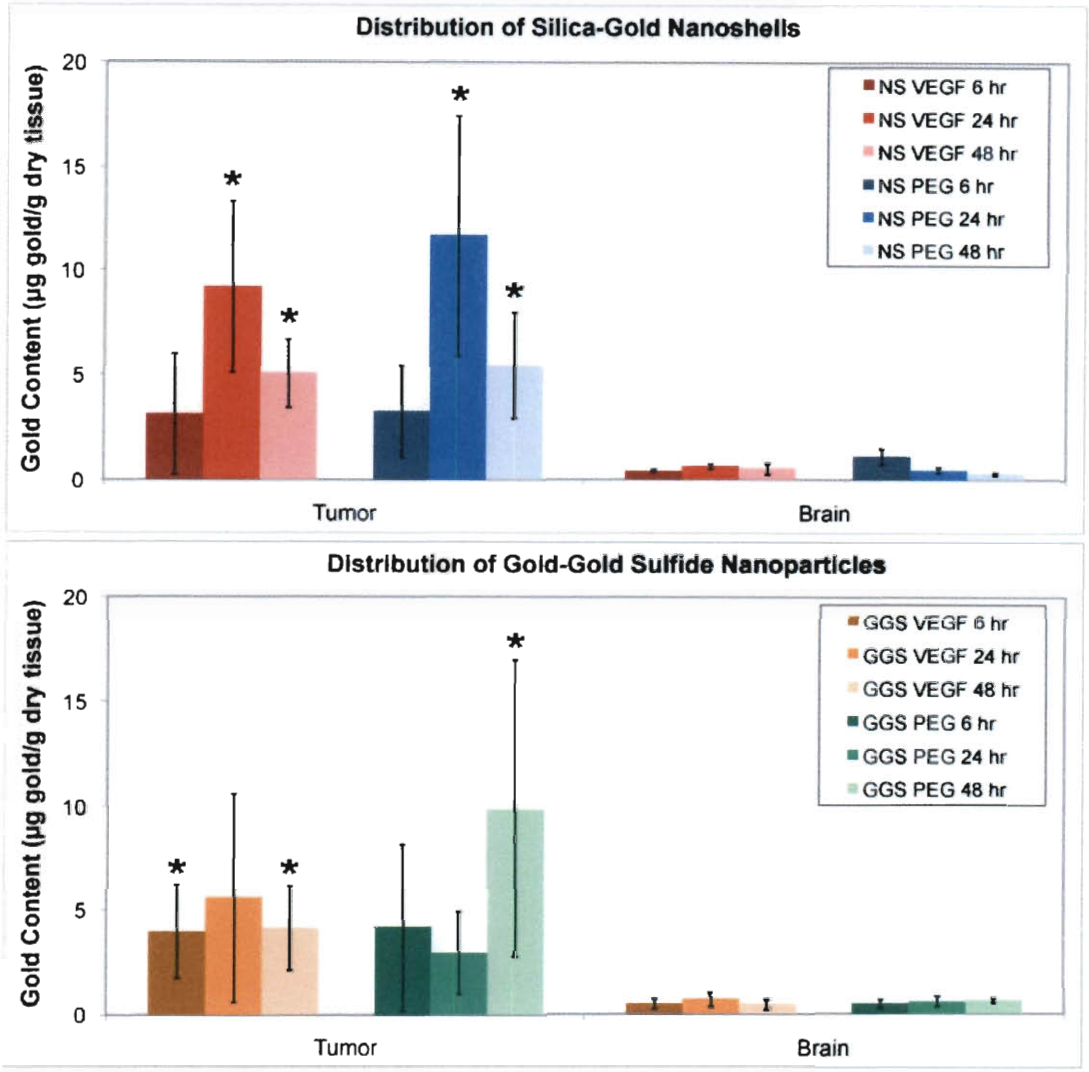

Figure 6.8: Nanoparticle accumulation in intracranial tumors. This chart shows an expansion of the y-axis from Figure 6.7 to more clearly identify differences in nanoparticle accumulation between the tumor and the normal brain. Times at which gold found in the tumor was significantly increased from gold content in the normal brain for the same nanoparticle type are marked (*$p<0.05$, student's t-test).

6.3.5 Intravital Microscopy Indicates that Thermal Therapy with VEGF-Coated Nanoshells Disrupts Tumor Vasculature

With intravital microscopy the superficial layer of the tumor appears as a bright central region due to the GFP signal emitting from the tumor cells and the tumor-associated vessels are observed as shadows. This allows changes in vasculature induced by therapy

to be monitored both qualitatively and quantitatively by calculating vessel density.

Figure 6.9 shows intravital microscopy images acquired for a mouse that received saline and for a mouse that received VEGF nanoshells one day prior to laser treatment. The left column displays an image acquired immediately before the laser was applied and the right column displays the same region 6 days later. In the saline control mouse, the tumor signal continues to grow over time and the vessels appear to be maturing. In contrast, the vessels appear to be disrupted following treatment for the VEGF-NS treated mouse and the tumor signal remains stable over this timeframe.

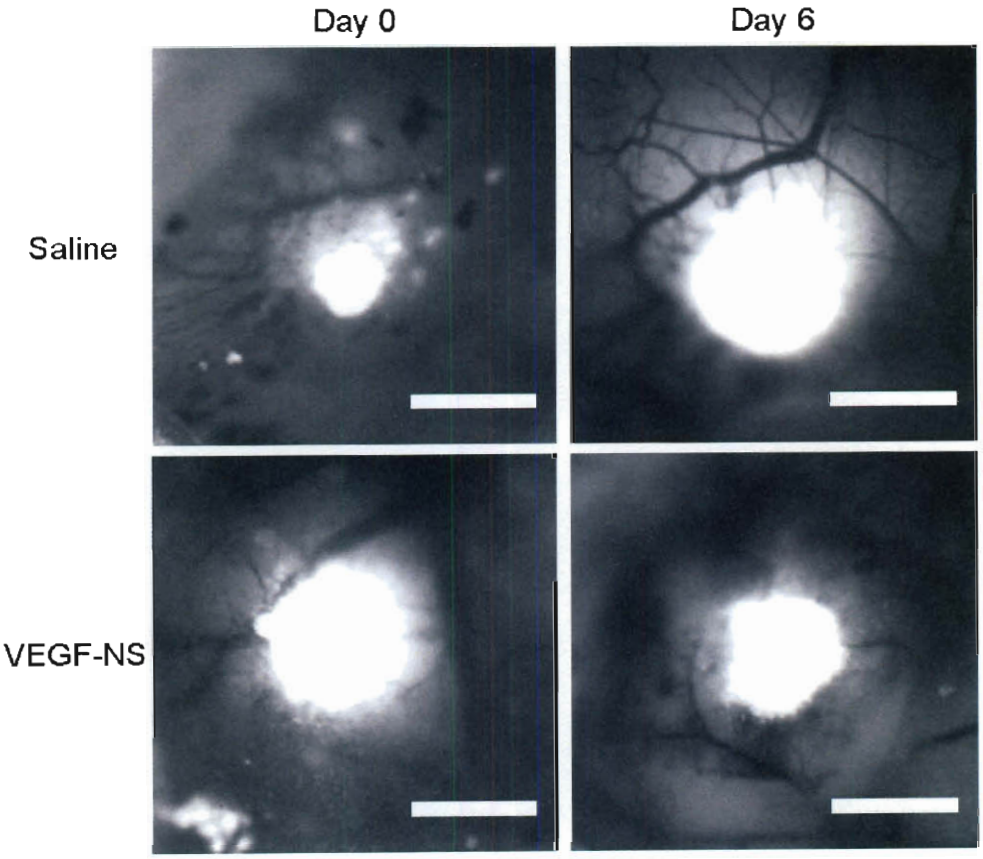

Figure 6.9: Intravital microscopy reveals changes in tumor vasculature following treatment. Changes in tumor size and vessel morphology were qualitatively evaluated by comparing intravital microscopy images acquired the day the laser was applied and six days later. The mouse treated with saline shows increasing tumor signal and signs of vessel maturation, while the mouse treated with VEGF-NS shows a stable tumor signal and signs of vessel disruption. Scale bars = 1 mm.

Changes in vasculature were quantified for the three mice that received saline and for the three mice that received VEGF-NS using intravital microscopy images acquired on Day 0 and Day 3. As shown below in **Figure 6.10**, vessel density increased by 18% for the saline group but decreased by 24% for the VEGF-NS treatment group over these three days; this difference was significant at the 95% confidence level by a student's t-test. Data in the figure represent the mean and standard error for each group.

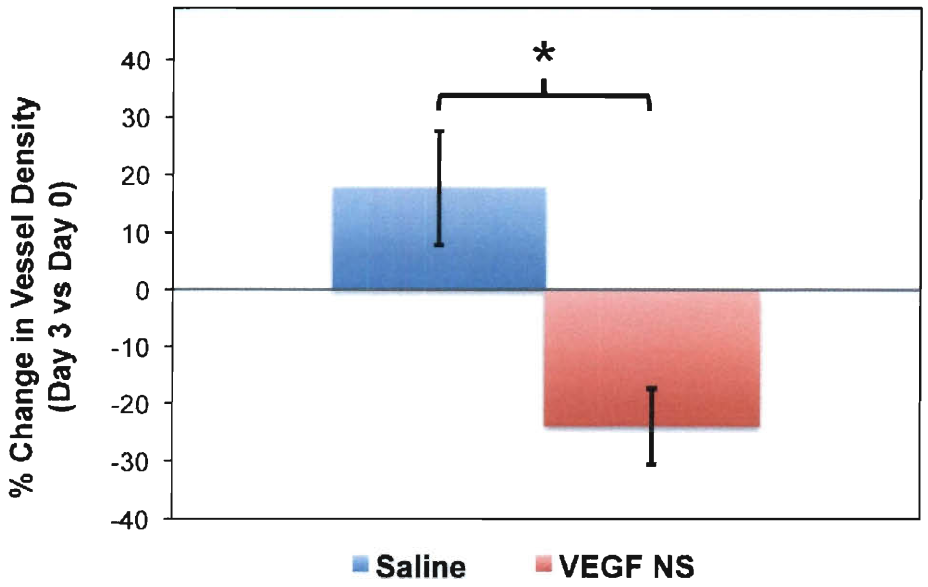

Figure 6.10: Quantification of vessel density highlights treatment effect. Mice that received saline exhibited a mean increase in vessel density of 18% over three days after laser treatment (blue bar) while mice that received VEGF-coated nanoshells experienced a 24% decrease in vessel density (red bar) (*$p<0.05$, student's t-test).

6.3.5 Histology Supports Intravital Microscopy Data and Indicates that VEGF-Coated Nanoshells Remain Proximal to Tumor Vessels

A subset of mice was euthanized immediately following laser application to further investigate the effects of therapy on the vasculature within the tumor and the normal brain since the laser application area covered both regions after it passed through the cranial window. **Figure 6.11** displays images of H&E stained sections of the tumor and

the normal brain for mice exposed to saline, VEGF-NS, and PEG-NS. There appear to be no changes to vasculature within the normal brain for any of the groups, indicating that both the laser power and the particle concentration are low enough to prevent thermal damage. By contrast, there are very extreme changes in the tumor vasculature for both PEG-NS and VEGF-NS treated mice, but not for saline control mice. Signs of vessel congestion, dilation, and hemorrhaging observed in the treatment arms were confirmed by a trained pathologist.

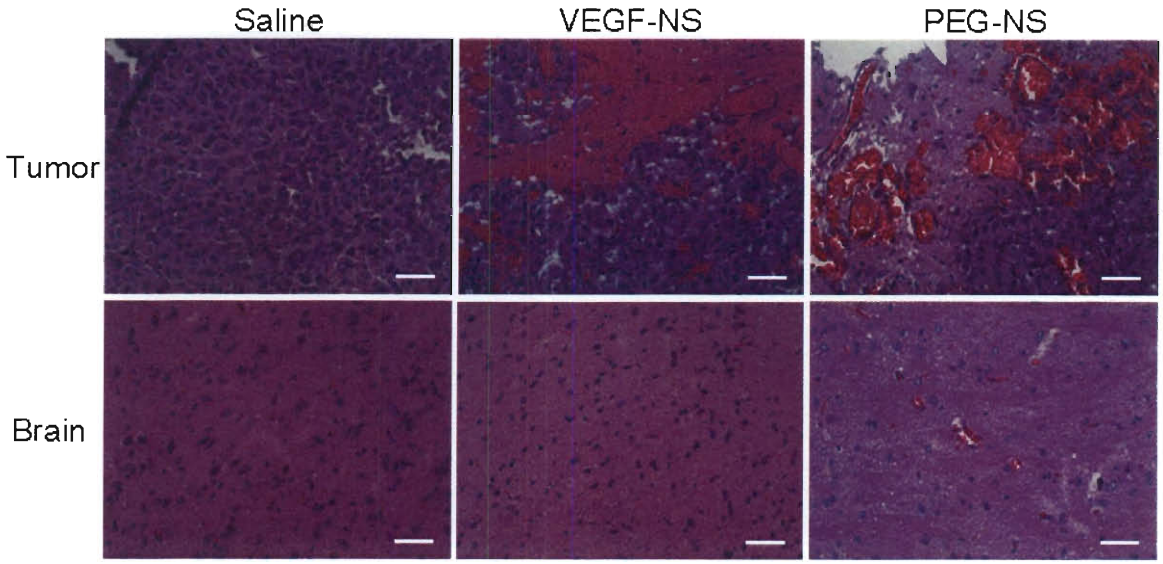

Figure 6.11: Histological evaluation of vascular-targeted photothermal therapy. Mice that received saline, VEGF-coated nanoshells, or PEG-coated nanoshells were sacrificed immediately after laser exposure to evaluate the effects of vascular-targeted photothermal therapy on the tumor and the normal brain with H&E staining. Minimal vascular disruption was observed in the normal brain for all groups and in the tumor for mice exposed to saline. Comparatively, mice exposed to VEGF-NS and PEG-NS showed signs of vessel dilation and hemorrhaging within the tumor. Scale bars = 50 μm.

Tissue sections from the same PEG-NS and VEGF-NS treated mice shown in Figure 6.11 were also stained for CD31 and imaged by fluorescence and darkfield microscopy to assess nanoparticle proximity to tumor vessels. Results of this analysis are displayed in **Figure 6.12**, where nuclei appear blue (DAPI), CD31 appears green (AF488

antibody), and nanoshells appear red (pseudo-colored from a darkfield image with background subtracted and merged with the fluorescence image). Red blood cells may also be observed as faint red due to tissue autofluorescence. Generally, the VEGF-coated nanoshells remained proximal to or within tumor vessels; interestingly, while many PEG-coated nanoshells are near vessels, many are also seen farther from the vessels. Thus, it appears that the VEGF coating is limiting the particle distribution to tumor vessels, as desired. It should be noted that a limitation of the analysis here is that it accounts for only one sample of each particle type; a more thorough study of multiple tissue samples needs to be performed to ensure this finding is not coincidental. Furthermore, it would be better to perform this analysis on tissue samples that have not been previously exposed to the laser since it is possible that the PEG-coated nanoparticles may have leaked out of the vessels after they were disrupted rather than extravasating out of the vessels while they remained intact.

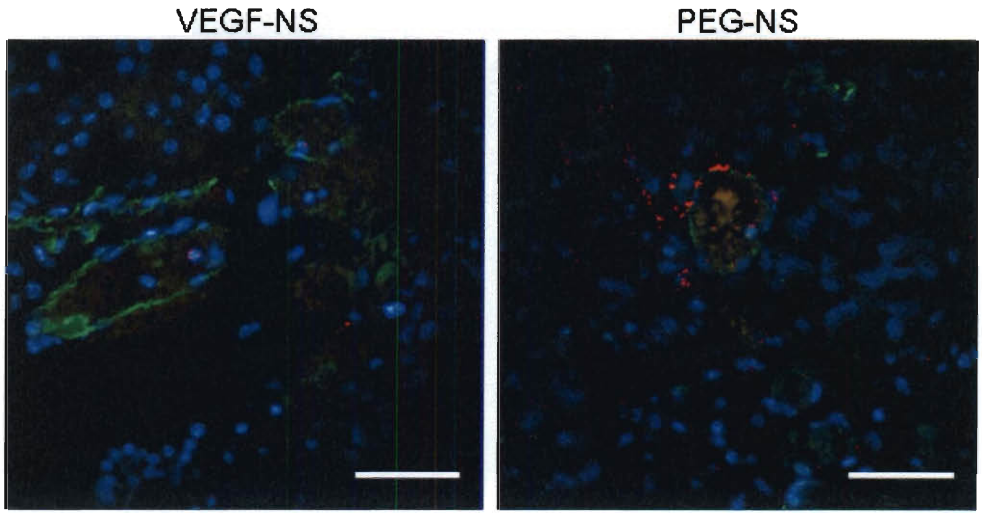

Figure 6.12: Microscopy shows nanoparticles remain proximal to tumor vessels. Darkfield and fluorescence microscopy reveal that both VEGF-coated and PEG-coated nanoshells remain proximal to tumor vessels. Vessels appear green (anti-CD31 antibody), nuclei appear blue (DAPI), and nanoparticles appear red. Scale bars = 50 μm.

6.3.8 Discussion

Since the concept that tumors are angiogenesis-dependent was introduced in the 1970s (Folkman 1971), there has been explosive growth in development of vascular-targeted cancer therapies. Anti-angiogenic therapy seems particularly well suited for high-grade gliomas because they are among the most densely vascularized tumors. Unfortunately, approaches that utilize antibodies or small molecule inhibitors to disrupt tumor vasculature have faced clinical setbacks, including both toxicities and the inability to prevent vascular endothelial cells from developing resistance mechanisms such as signaling through alternative pathways. To overcome these limitations, nanoparticle-mediated therapies are now being investigated. Here, VEGF-coated nanoparticles were evaluated for the ability to target intracranial glioma tumors and to facilitate subsequent vascular-focused photothermal therapy since the VEGF-receptor pathway is critical in glioma angiogenesis.

Both *in vitro* and *in vivo* assessment of vascular-targeted photothermal therapy was performed. Gold-gold sulfide nanoparticles and nanoshells coated with VEGF bound to VEGFR-2 expressing endothelial cells *in vitro*, marking these cells for photothermal ablation. Based on these data, it was decided to study the treatment further in intracranial tumor experiments. *In vivo*, both PEG-coated and VEGF-coated nanoparticles accumulated at higher levels in intracranial tumors than in the normal brain, and this delineation is necessary for therapy to be both effective *and* safe. Studies of therapeutic effect with nanoshells indicated that this difference allowed vessel disruption to be achieved selectively in and around the tumor but not in the normal brain of mice treated with a single 3 min laser exposure. Interestingly, although both PEG-coated and

6.3.7 Animal Survival Time Increases Moderately Following Vascular-Targeted Photothermal Therapy of Intracranial Glioma Tumors

Animal survival time following treatment was monitored to evaluate therapeutic efficacy. **Figure 6.13** is a Kaplan-Meier diagram showing the percentage of mice alive versus days following laser exposure for the saline control group (blue), the PEG-NS treatment group (green), and the VEGF-NS treatment group (red). Mice that received PEG-coated nanoshells did not display a survival benefit compared to mice that received saline, but mice that received VEGF-coated nanoshells had a moderate, though not statistically significant ($p=0.15$ with log-rank test), improvement in survival. The median survival for mice exposed to saline was 5 days compared to 3 days for mice exposed to PEG-coated nanoshells and 11 days for mice exposed to VEGF-coated nanoshells.

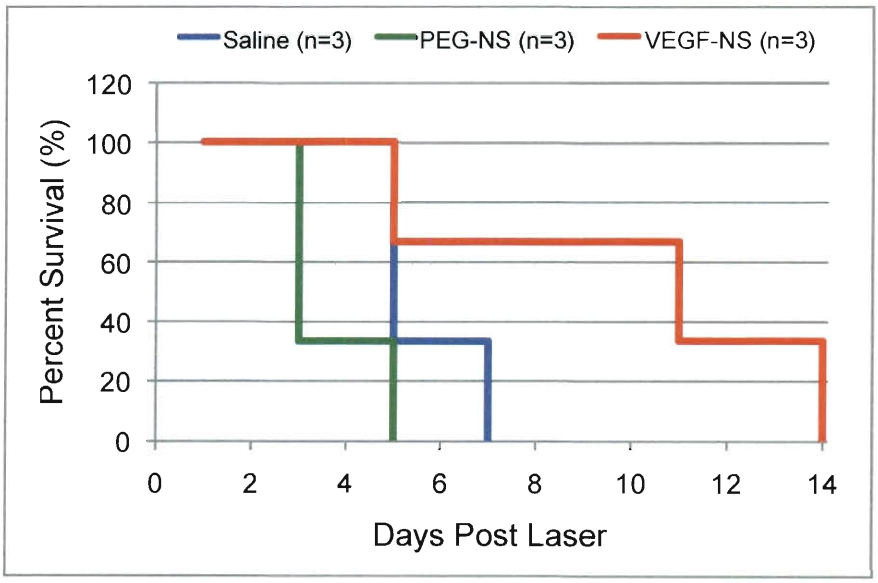

Figure 6.13: Kaplan-Meier survival analysis of vascular-targeted photothermal therapy. The percentage of mice alive versus days following laser treatment is shown for the saline control group (blue line, n=3), the PEG-NS non-targeted therapy group (green line, n=3), and the VEGF-NS vascular-targeted therapy group (red line, n=3). Vascular-targeted therapy prolonged median survival 2.2-fold compared to the saline control group (11 days versus 5 days).

VEGF-coated nanoshells induced vascular changes, there was a moderate survival benefit only for the targeted nanoparticle group compared to mice that received laser exposure alone. Although the median survival time doubled, this improvement was not statistically significant. Considered together, these results suggest that with further development vascular-focused photothermal therapy could be an effective strategy for elimination of brain tumors.

To improve vascular-targeted photothermal therapy of brain tumors, it may be necessary to use a more direct mode of light delivery such as a fiber-optic probe. The rationale in support of fiber-optic light delivery is two-fold: first, it would ensure more even distribution of light energy throughout the tumor and avoid energy loss that occurs with external delivery as light traverses the normal brain before reaching the tumor; second, it would prevent off-target heating of nanoparticles that may accumulate in the normal brain. The feasibility of fiber-optic light delivery has already been demonstrated in two studies of nanoparticle-mediated therapy of brain tumors (Reddy *et al.* 2006; Schwartz *et al.* 2009). In the first, a probe delivered light for vascular-targeted photodynamic therapy mediated by F3-conjugated polymeric nanoparticles containing Photofrin (Reddy *et al.* 2006). The F3-targeting peptide binds nucleolin, a shuttle protein specifically expressed on angiogenic endothelial cells within tumor vasculature. In this study, rats with 9L glioma were exposed to a 750 mW for 7.5 min and median survival for mice treated with the targeted nanoparticles increased to 33 days compared to just 8.5 days for mice treated with only the laser. It should be noted that, to date, this is the most successful vascular-targeted nanoparticle-mediated therapy reported in the literature (Reddy *et al.* 2006).

The second study to demonstrate the utility of fiber-optic light delivery was reported more recently (Schwartz *et al.* 2009). In a canine brain tumor model, a fiber-optic probe was used to deliver light for non-targeted nanoshell-mediated thermal therapy. Intracranial tumor temperatures of 65.8 ± 4.1°C were achieved in the presence of nanoshells compared to 53.1°C for a tumor infused with vehicle. Within the normal brain, the maximum recorded temperature was 48.6 ± 1.1°C, below the damage threshold. This paper did not include survival data, however, so it was impossible to gauge treatment response (Schwartz *et al.* 2009). The work reported in this chapter was thus the first attempt to assess survival benefit from nanoshell-mediated photothermal therapy of intracranial brain tumors. A similar approach to brain tumor therapy is magnetic fluid hyperthermia (MFH), which has been introduced in previous chapters. When non-targeted MFH with aminosilane-coated iron-oxide nanoparticles was tested in rats bearing 3-4 mm tumors, the animals experienced 1.7-4.5-fold prolongation of survival, with higher temperatures achieved in the tumor yielding better response (Jordan *et al.* 2006). One complication of comparing the studies in this chapter to the MFH studies is that a 3-5 mm tumor in a mouse accounts for a larger total brain volume than a 3-4 mm tumor in a rat. In addition, the nanoshells and GGS-NPs used in this thesis were intravenously delivered while the iron-oxide nanoparticles were directly injected into the tumor. Nevertheless, it is promising that vascular-targeted nanoshell therapy yielded a similar 2-fold increase in median survival following only a single dose of nanoparticles and laser exposure.

Although the data reported here are exciting for an initial attempt at vascular-focused hyperthermia, parameters of the photothermal therapy will need to be adjusted in

future studies since a clinically relevant improvement in survival has not yet been achieved. For example, possible changes could include increasing the nanoparticle dosage or using a different nanoparticle delivery method. Several groups have utilized either direct intratumoral delivery or convection-enhanced delivery of nanoparticles for brain tumor therapy (Jordan *et al.* 2006; Hadjipanayis *et al.* 2010). Similarly, as already mentioned, the light delivery technique should be improved since in the clinical setting a cranial window would not be feasible. Additionally, multiple doses of the laser could be applied to improve the treatment response. Here, the laser was applied from only one direction but it is likely that repeated application from multiple directions would improve outcome by capturing any outlying cells missed by the initial treatment. Since infiltrative glioma cells beyond the main tumor mass missed by conventional therapies are often responsible for patient relapse (DeAngelis 2001), it is critical to develop photothermal therapy with the goal of eliminating these evasive cells. Once these improvements have been incorporated, vascular-targeted photothermal therapy should be able to elicit a better therapeutic response.

6.4 Conclusions

Overall, the results of these studies indicate that VEGF-coated nanoshells have potential as a novel mediator of anti-angiogenic glioma therapy. Vascular-targeted nanoshells can bind vessels associated with intracranial tumors and subsequent application of a near-infrared laser induces hyperthermia to disrupt the tumor vessels. In turn, this disruption slows tumor growth and improves survival compared to mice treated with non-targeted nanoshells or with saline. Importantly, the normal brain appears unaffected by treatment based on histological assessment. As this therapy is further developed it will be critical

to continually evaluate the safety margin since brain tumor treatments are often plagued by long-term side effects.

Vascular-targeting confers several advantages to nanoparticles for photothermal therapy. First, because the receptor for the targeting agent is expressed on the luminal endothelium, nanoparticles do not need to extravasate out of blood vessels for therapy to be effective. Furthermore, the nanoparticles do not need to evade the blood-brain barrier, which is disrupted in high-grade glioma but may not be disrupted in early stage tumors. Second, although glioma was studied here, the surface markers expressed by endothelial cells involved in tumor angiogenesis are consistent across multiple tumor types. As a result, VEGF-coated nanoshells or GGS-NPs could be used for photothermal therapy of a wide-variety of tumors, increasing the applicability of this new therapy. A final advantage of vascular targeting that is specific to the VEGF ligand used in this work is based on the aforementioned discovery that the VEGF-signaling pathway regulates both paracrine and autocrine promotion of glioma tumorigenesis (Knizetova *et al.* 2008). Since VEGFR-2 is expressed on both endothelial cells and some brain tumor cells, VEGF-coated nanoshells or GGS-NPs could potentially inhibit tumor growth by enabling thermal ablation of both targets.

To conclude, vascular-targeted nanoparticle-mediated photothermal therapy offers an intriguing alternative to conventional treatment for brain tumors. As mentioned earlier, vascular endothelial cells are highly resistant to chemotherapeutics, but it has already been shown in a breast tumor model that some drug-resistant cells are less resistant to nanoshell-mediated photothermal therapy (Carpin *et al.* 2011). Similarly, for brain tumors it is expected that vascular-targeted photothermal therapy should remain

effective even when chemotherapy fails, assuming the target receptor expression is maintained. Photothermal therapy offers the advantage over both chemotherapy and radiation therapy that it is relatively quick, and should prevent patients from enduring weeks or months of treatment. Finally, the procedures are much simpler to perform and therefore less risk is involved than with surgery. Even with the use of a fiber-optic probe to deliver light, it is likely that the normal brain will be affected to a much lesser extent, although the treatment margins around tumors following photothermal therapy remain to be defined. In the future, vascular-targeted nanoparticle-mediated photothermal therapy could be an excellent treatment not only for primary brain tumors, but also for a multitude of tumor types.

Chapter 7: Conclusions and Future Directions

7.1 Introduction

This thesis has attempted to advance the field of photothermal cancer therapy by developing silica-gold nanoshells and gold-gold sulfide nanoparticles as multifunctional agents for molecularly targeted imaging and treatment of cancer. Here, the significance of the results of this thesis will be summarized and then the impact of these results on the future of photothermal therapy will be discussed.

7.2 Developing Molecularly-Targeted Gold-Based Nanoparticles for Cancer Imaging and Near-Infrared Photothermal Therapy

Photothermal therapy incorporates nanoparticles as exogenous absorbers of near-infrared light to selectively delivery heat capable of inducing cell death to tumors. The benefits of photothermal therapy over surgical resection, chemotherapy, and radiation therapy are numerous; this approach is minimally invasive, simple to perform, has a low risk of side effects, and has the potential to treat embedded tumors in vital regions where surgical resection is not feasible. Additionally, the unique optical properties of nanoparticles allow them to act simultaneously as contrast agents for a variety of imaging modalities. Previously, PEG-coated nanoshells and gold-gold sulfide nanoparticles were used for photothermal cancer therapy *in vivo* using passive accumulation (O'Neal *et al.* 2004; Gobin *et al.* 2010); but, as increasing evidence showed that molecular alterations play a critical role in tumor development, approaches to combat the disease at this scale were developed. Specifically, nanoshells have been coated with antibodies (Loo *et al.* 2005;

Bernardi *et al.* 2008), proteins (Gobin *et al.* 2008), and peptides (Liu *et al.* 2010) to facilitate binding with tumor cell-specific antigens. While this advancement was met with great enthusiasm, it remained to be validated *in vivo.* Therefore, the overall goal of this thesis was to evaluate molecularly targeted cancer therapy *in vivo.*

To begin, antibody-coated nanoshells were shown to have tumor cell-specific targeting *in vitro* using both monoculture and co-culture experiments. When nanoshells were coated with anti-HER2 antibodies, they specifically bound breast carcinoma cells that over-express the HER2 receptor even when these cells were adjacent to HER2-negative endothelial cells. Furthermore, these functionalized nanoshells were able to bind ovarian tumor tissue *ex vivo* at levels that corresponded to the HER2 receptor status. This suggests that, in the future, biopsy specimens could be exposed to antibody-coated nanoshells to determine a patient's receptor level status and predict whether they would benefit from targeted photothermal therapy.

In the following chapter, it was proven that the conjugation chemistry used to functionalize silica-gold nanoshells is also acceptable for gold-gold sulfide nanoparticles. This was the first demonstration that GGS-NPs can be molecularly addressed. It was also shown that the light-absorbing properties of GGS-NPs facilitate their use as dual imaging and therapeutic agents when used in conjunction with femtosecond-pulsed NIR lasers. At low laser intensities antibody-coated gold-gold sulfide nanoparticles can be used to image cancerous cells, and then at higher laser intensities the particles can mediate thermal ablation. This capability renders GGS-NPs a truly "theranostic" nanoparticle capable of targeting, imaging, and therapy all in a single platform.

Chapter 5 investigated, for the first time, the distribution profile of antibody-coated and PEG-coated nanoshells and gold-gold sulfide nanoparticles. For these studies, a subcutaneous high-grade glioma tumor model was used. These studies provided insight into how nanoparticle size and surface coating dictate *in vivo* organ distribution. Contrary to predictions, coating these nanoparticles with antibodies did not improve their overall uptake into the tumor. Since these studies have been completed, however, more publications have appeared with similar data that suggests molecular targeting of nanoparticles does not increase their uptake into tumors, but rather improves their cellular internalization (Choi *et al.* 2010; Huang *et al.* 2010). Following the distribution study, PEG-coated nanoparticles were used to establish the sensitivity of these aggressive primary brain tumors to photothermal therapy. Intravenously delivered nanoshells accumulated in the tumor at levels sufficient to induce tumor regression when the laser was applied 24 h post-intravenous delivery; mice that received gold-gold sulfide nanoparticles displayed only a partial tumor response. This data established that primary brain tumors are sensitive to photothermal therapy and warranted further investigation using an intracranial tumor model.

Since brain tumors are highly vascularized, for the intracranial tumor studies the nanoshells and gold-gold sulfide nanoparticles were coated with vascular endothelial growth factor (VEGF). It was hypothesized that VEGF-coated nanoparticles would bind tumor vessels, which over-express VEGF receptor-2 (VEGFR-2), and that the tumor vessels could then be disrupted upon application of the NIR laser. Following disruption of tumor vasculature the level of oxygen and nutrients in the tumor should decrease, leading to tumor regression. First, the ability of VEGF-coated nanoparticles to bind

VEGFR-2 positive endothelial cells and facilitate thermal ablation of these cells was demonstrated *in vitro.* Then, a distribution study in mice bearing intracranial glioma tumors proved that VEGF-coated nanoparticles could accumulate in these tumors. In subsequent treatment studies, it was shown that VEGF-coated nanoshells could induce vascular damage within the tumor but not the normal brain, and that this vascular-targeted therapy could prolong median survival by 2.2-fold versus mice that received only laser exposure. This was the first attempt to treat an orthotopically-implanted tumor using nanoshell-mediated photothermal therapy, an important advancement since tissue environment can play a critical role in tumor behavior.

7.3 Future Directions

Molecular targeting is anticipated to improve the future of cancer nanomedicine by enhancing specificity, prolonging nanoparticle retention in the tumor, and decreasing off-target effects. As demonstrated by the results of this thesis research, there is still much work to be performed and knowledge to be gained before this potential will be fully realized. Several groups have tested targeting schemes *in vitro,* but *in vivo* validation is lacking. It is critical to evaluate these systems in animal models because, as shown with antibodies in this thesis, in a complex biological setting it is more difficult to reach the target site. In these studies, whole antibodies were used and it is believed that the Fc portion induced immune recognition and more rapid elimination of the nanoparticles from the body. Comparatively, recognition and rapid clearance did not appear to be a significant problem for the VEGF-coated nanoparticles. In the future, it would be interesting to evaluate targeting with antibody fragments that do not contain the Fc fragment. Alternatively, aptamers could be a good option because they have no toxicity

or immunogenicity but exhibit high affinity (Blank and Blind 2005). More recently, Ruoslahti and colleagues have developed "tissue-penetrating peptides" that display remarkable tumor uptake (Sugahara *et al.* 2009). While some groups have demonstrated the ability to encapsulate nanoshells within macrophages for cell-mediated delivery (Choi *et al.* 2007; Baek *et al.* 2011), this approach lacks the ability to provide functional information and would not therefore be suitable as a molecular targeting strategy.

In addition to optimizing the targeting strategy used to bind nanoshells and GGS-NPs to specific cells, photothermal therapy could be further improved by capitalizing on the ability of these nanoparticles to provide dual imaging and therapy. In Chapter 4, it was shown that two-photon microscopy could be used with nanoparticles to "see and treat" tumors in a single setting. Future work should continue to develop this approach for *in vivo* application. Systems that offer dual imaging and therapy will be critical to successful elimination of tumors, particularly high-grade brain tumors in which many of the cells are infiltrative and may be found several centimeters away from the main tumor mass. Often these cells are left behind during surgical resection, so it will be important to determine whether these cells can be (1) targeted by nanoshells or GGS-NPs delivered systemically, (2) identified using inherent nanoparticle contrast, and (3) safely eliminated with photothermal therapy without inducing damage to normal brain in the laser field.

To further enhance the dual imaging and therapy capabilities of nanoshells and gold-gold sulfide nanoparticles, it may be beneficial to add moieties to the nanoparticle surface that enable contrast with currently used clinical imaging systems. For example, since MRI is one of the most powerful imaging techniques available it would be valuable to add MRI contrast-enhancing capability to the nanoparticles; this has recently been

realized for silica-gold nanoshells. Bardhan *et al.* coated nanoshells with amine-terminated iron-oxide nanoparticles and surrounded them with a silica layer doped with the fluorophore indocyanine green (ICG) (2009). After adding anti-HER2 antibodies to the surface, the complex was able to target cells *in vitro*, provide enhanced contrast for MR and fluorescence microscopy, and mediate photothermal therapy (Bardhan *et al.* 2009). To improve this system, one might use gadolinium chelates instead of iron-oxide nanoparticles. This offers the advantage that the overall system could be reduced in size, enabling better penetration into tumors via the EPR effect. Futhermore, gadolinium chelates are FDA approved and are the most commonly used contrast agent clinically; as such, it is likely that approval of systems that use gadolinium chelates would be more streamlined. It is important to note that gadolinium chelates provide positive MR contrast (brightened signal) while iron oxide nanoparticles provide negative MR contrast (darkened signal), and so the choice of appropriate coating may depend partly upon the end application.

Lastly, photothermal therapy could be improved by developing gold-gold sulfide nanoparticles and nanoshells that release both silencing RNA and chemotherapeutic drugs upon heating with exposure to NIR light. It has previously been shown that cisplatin can be loaded onto gold-gold sulfide nanoparticles and released on-demand with light exposure (Tan *et al.* 2009), and it is possible that combining drug delivery with gene therapy may enhance transfection efficiency or achieve a synergistic effect. While systems that combine gene therapy and drug delivery have been created (Zhang *et al.* 2010), none have been able to elicit on-demand release. By utilizing NIR-absorbing nanoparticles to provide this capability, drug and siRNA content within tumors could be

maximized and the tumor could be attacked by three mechanisms (photothermal therapy, drug delivery, and gene therapy) in one platform. In addition, the nanoparticles' optical properties could yield the ability to monitor delivery with two-photon microscopy, optical coherence tomography, or photoacoustic tomography, as desired.

The overarching goal of cancer nanomedicine is to produce multifunctional materials capable of molecular targeting, imaging, and treatment, and this thesis has demonstrated that nanoshells and gold-gold sulfide nanoparticles have potential to meet this goal. These nanoparticles can be functionalized with targeting moieties through well-established chemistry, and their inherent optical properties render them suitable as optical contrast agents and mediators of photothermal therapy. Improvements could include (1) optimizing the targeting ligands to reduce immune recognition and improve tumor internalization, (2) endowing the nanoparticles with properties that enable contrast enhancement for multiple imaging modalities, and (3) incorporating on-demand release of chemotherapeutics and silencing RNA to provide a synergistic anti-tumor effect. In the future, nanoparticle-mediated photothermal therapy could offer a minimally invasive and highly effective alternative to imaging and treatment strategies used in conventional cancer management.

References

Abdullah B (2006). "Molecular imaging: spawning a new melting-pot for biomedical imaging." Biomedical Imaging and Intervention Journal **2**(4): e28.

Ahmed N, Ratnayake M, Savoldo B, et al. (2007). "Regression of Experimental Medulloblastoma following Transfer of HER2-Specific T Cells." Cancer Res **67**(12): 5957-5964.

Albanell J and Baselga J (1999). "Trastuzumab, a humanized anti-HER2 monoclonal antibody, for the treatment of breast cancer." Drugs Today **35**: 931-946.

Alison M and Sarraf C (1997). Understanding cancer: From basic science to clinical practice. Cambridge, Cambridge University Press.

Arap W, Pasqualini R and Ruoslahti E (1998). "Cancer Treatment by Targeted Drug Delivery to Tumor Vasculature in a Mouse Model." Science **279**: 377-380.

Averitt RD, Westcott SL and Halas NJ (1999). "Linear optical properties of gold nanoshells." Journal of the Optical Society of America B **16**(10): 1824-1832.

Baek S-K, Makkouk A, Krasieva T, et al. (2011). "Photothermal treatment of glioma; an in vitro study of macrophage-mediated delivery of gold nanoshells." Journal of Neuro-Oncology: 1-10.

Bardhan R, Chen W, Perez-Torrez C, et al. (2009). "Nanoshells with Targeted Simultaneous Enhancement of Magnetic and Optical Imaging and Photothermal Therapeutic Response." Advanced Functional Materials **19**: 1-9.

Barentsz J, Takahashi S, Oyen W, et al. (2006). "Commonly Used Imaging Techniques for Diagnosis and Staging." Journal of Clinical Oncology **24**(20): 3234-3244.

Batist G, Ramakrishnan G, Rao CS, et al. (2001). "Reduced Cardiotoxicity and Preserved Antitumor Efficacy of Liposome-Encapsulated Doxorubicin and Cyclophosphamide Compared With Conventional Doxorubicin and Cyclophosphamide in a Randomized, Multicenter Trial of Metastatic Breast Cancer." Journal of Clinical Oncology **19**(5): 1444-1454.

Benjamin LE, Golijanin D, Itin A, et al. (1999). "Selective ablation of immature blood vessels in established human tumors follows vascular endothelial growth factor withdrawal." Journal of Clinical Investigation **103**(2): 159-165.

Bernardi RJ, Lowery AR, Thompson PA, et al. (2008). "Immunonanoshells for targeted photothermal ablation in medulloblastoma and glioma: an in vitro evaluation using human cell lines." J Neurooncol **86**(2): 165-172.

Bickford L, Agollah G, Drezek R, et al. (2010). "Silica-gold nanoshells as potential intraoperative molecular probes for HER2-overexpression in ex vivo breast tissue using near-infrared reflectance confocal microscopy." Breast Cancer Research and Treatment **120**(3): 547-555.

Bickford L, Sun J, Fu K, et al. (2008). "Enhanced multi-spectral imaging of live breast cancer cells using immunotargeted gold nanoshells and two-photon excitation microscopy." Nanotechnology **19**(31): 315102-315200.

Bickford LR, Day ES, Hu Y, et al. (2010). Biomedical Applications of Multifunctional Silica-Based Gold Nanoshells. Handbook of Materials for Nanomedicine. MM Amiji and VP Torchilin, Pan Stanford Publishing.

Bikram M, Gobin AM, Whitmire RE, et al. (2007). "Temperature-sensitive hydrogels with SiO2-Au nanoshells for controlled drug delivery." J Control Release **123**(3): 219-227.

Black KC, Kirkpatrick ND, Troutman TS, et al. (2008). "Gold nanorods targeted to delta opioid receptor: Plasmon-resonant contrast and photothermal agents." Molecular Imaging **7**(1): 50-57.

Blank M and Blind M (2005). "Aptamers as tools for target validation." Current Opinion in Chemical Biology **9**(4): 336-342.

Boyd GT, Yu ZH and Shen YR (1986). "Photoinduced luminescence from the noble metals and its enhancement on roughened surfaces." Physical Review B **33**(12): 7923-7936.

Braun GB, Pallaoro A, Wu G, et al. (2009). "Laser-Activated Gene Silencing via Gold Nanoshell-siRNA Conjugates." ACS Nano **3**(7): 2007-2015.

Butler JM, Rapp SR and Shaw EG (2006). "Managing the cognitive effects of brain tumor radiation therapy." Curr Treat Options Oncol **7**(6): 517-523.

Cang H, Sun T, Li Z-Y, et al. (2005). "Gold nanocages as contrast agents for spectroscopic optical coherence tomography." Optics Letters **30**(22): 3048-3050.

Cardinal J, Klune JR, Chory E, et al. (2008). "Noninvasive radiofrequency ablation of cancer targeted by gold nanoparticles." Surgery **144**(2): 125-132.

Carmeliet P and Jain RK (2000). "Angiogenesis in cancer and other diseases." Nature **407**(6801): 249-257.

Carpin L, Bickford L, Agollah G, et al. (2011). "Immunoconjugated gold nanoshell-mediated photothermal ablation of trastuzumab-resistant breast cancer cells." Breast Cancer Research and Treatment **125**(1): 27-34.

Chamberlain MC (2008). "Antiangiogenesis: biology and utility in the treatment of gliomas." Expert Review of Neurotherapeutics **8**(10): 1419-1423.

Chau Y, Padera RF, Dang NM, et al. (2006). "Antitumor efficacy of a novel polymer–peptide–drug conjugate in human tumor xenograft models." International Journal of Cancer **118**(6): 1519-1526.

Chen J, Glaus C, Laforest R, et al. (2010). "Gold Nanocages as Photothermal Transducers for Cancer Treatment." Small **6**(7): 811-817.

Chen J, Wang D, Xi J, et al. (2007). "Immuno gold nanocages with tailored optical properties for targeted photothermal destruction of cancer cells." Nano Letters **7**(5): 1318.

Choi CHJ, Alabi CA, Webster P, et al. (2010). "Mechanism of active targeting in solid tumors with transferrin-containing gold nanoparticles." Proceedings of the National Academy of Sciences **107**(3): 1235-1240.

Choi M-R, Stanton-Maxey KJ, Stanley JK, et al. (2007). "A Cellular Trojan Horse for Delivery of Therapeutic Nanoparticles into Tumors." Nano Letters **7**(12): 3759-3765.

Choudhury SR, Karmakar S, Banik NL, et al. (2010). Role of Angiogenesis in the Pathogenesis of Glioblastoma and Antiangiogenic Therapies for Controlling Glioblastoma. Glioblastoma: Molecular Mechanisms of Pathogenesis and Current Therapeutic Strategies. SK Ray, Springer Science+Business Media, LLC.

ClinicalTrials.gov (2010). Pilot study of AuroLase therapy in refractory and/or recurrent tumors of the head and neck: 4.

Cole JR, Mirin NA, Knight MW, et al. (2009). "Photothermal Efficiencies of Nanoshells and Nanorods for Clinical Therapeutic Applications." The Journal of Physical Chemistry C **113**(28): 12090-12094.

Colotta F, Allavena P, Sica A, et al. (2009). "Cancer-related inflammation, the seventh hallmark of cancer." Carcinogenesis **30**(7): 1073-1081.

Couvreur P and Vauthier C (2006). "Nanotechnology: Intelligent Design to Treat Complex Disease." Pharmaceutical Research **23**(7): 1417-1450.

Cross MJ, Dixelius J, Matsumoto T, et al. (2003). "VEGF-receptor signal transduction." Trends in Biochemical Sciences **28**(9): 488-494.

Curley SA (2001). "Radiofrequency Ablation of Malignant Liver Tumors." Oncologist **6**(1): 14-23.

Daumas-Duport C, Scheithauer B, Ofallon J, et al. (1988). "Grading of Astrocytomas-A Simple and Reproducible Method." Cancer **62**(10): 2152-2165.

Day ES, Bickford LR, Slater JH, et al. (2010). "Antibody-conjugated gold-gold sulfide nanoparticles as multifunctional agents for imaging and therapy of breast cancer." Int J Nanomedicine **5**: 445-454.

Day ES, Morton JG and West JL (2009). "Nanoparticles for Thermal Cancer Therapy." Journal of Biomechanical Engineering **131**(7): 074001-074005.

De Jong WH, Hagens WI, Krystek P, et al. (2008). "Particle size-dependent organ distribution of gold nanoparticles after intravenous administration." Biomaterials **29**(12): 1912-1919.

DeAngelis LM (2001). "Brain Tumors." N Engl J Med **344**(2): 114-123.

Debinski W, Gibo DM, Hulet SW, et al. (1999). "Receptor for Interleukin 13 is a Marker and Therapeutic Target for Human High-Grade Gliomas." Clinical Cancer Research **5**: 985-990.

Dickerson EB, Dreaden EC, Huang XH, et al. (2008). "Gold nanorod assisted near-infrared plasmonic photothermal therapy (PPTT) of squamous cell carcinoma in mice." Cancer Letters **269**(1): 57-66.

Ding H, Inoue S, Ljubimov AV, et al. (2010). "Inhibition of brain tumor growth by intravenous poly(β-l-malic acid) nanobioconjugate with pH-dependent drug release." Proceedings of the National Academy of Sciences **107**(42): 18143-18148.

Dong X and Mumper RJ (2010). "Nanomedicinal strategies to treat multidrug-resistant tumors: current progress." Nanomedicine **5**(4): 597-615.

Duff DG, Baiker A and Edwards PP (1993). "A New Hydrosol of Gold Clusters.1. Formation and Particle-Size Variation." Langmuir **9**(9): 2301-2309.

Durr NJ, Larson T, Smith DK, et al. (2007). "Two-photon luminescence imaging of cancer cells using molecularly targeted gold nanorods." Nano Letters **7**(4): 941-945.

Dvorak HF (2002). "Vascular Permeability Factor/Vascular Endothelial Growth Factor: A Critical Cytokine in Tumor Angiogenesis and a Potential Target for Diagnosis and Therapy." Journal of Clinical Oncology **20**(21): 4368-4380.

Eguchi J, Hatano M, Nishimura F, et al. (2006). "Identification of interleukin-13 receptor alpha2 peptide analogues capable of inducing improved antiglioma CTL responses." Cancer Research **66**: 5883-5891.

Fantin VR, Berardi MJ, Babbe H, et al. (2005). "A Bifunctional Targeted Peptide that Blocks HER-2 Tyrosine Kinase and Disables Mitochondrial Function in HER-2-Positive Carcinoma Cells." Cancer Research **65**(15): 6891-6900.

Ferrara N, Gerber HP and LeCouter J (2003). "The biology of VEGF and its receptors." Nature Medicine **9**(6): 669-676.

Ferrari M (2005). "Cancer nanotechnology: opportunities and challenges." Nat. Rev. Cancer **5**(3): 161-171.

Fidler IJ (1990). "Critical Factors in the Biology of Human Cancer Metastasis: Twenty-Eighth G. H. A. Clowes Memorial Award Lecture." Cancer Research **50**(19): 6130-6138.

Fidler IJ (2003). "The pathogenesis of cancer metastasis: the 'seed and soil' hypothesis revisited." Nat Rev Cancer **3**(6): 453-458.

Folkman J (1971). "Tumor angiogenesis: therapeutic implications." N Engl J Med **285**(21): 1182-1186.

Frangioni JV (2008). "New Technologies for Human Cancer Imaging." Journal of Clinical Oncology **26**(24): 4012-4021.

Gaber MW, Yuan H, Killmar JT, et al. (2004). "An intravital microscopy study of radiation-induced changes in permeability and leukocyte-endothelial cell interactions in the microvessels of the rat pia mater and cremaster muscle." Brain Research Protocols **13**: 1-10.

Gannon CJ, Cherukuri P, Yakobson BI, et al. (2007). "Carbon nanotube-enhanced thermal destruction of cancer cells in a noninvasive radiofrequency field." Cancer **110**(12): 2654-2665.

Gannon CJ, Patra CR, Bhattacharya R, et al. (2008). "Intracellular gold nanoparticles enhance non-invasive radiofrequency thermal destruction of human gastrointestinal cancer cells." Journal of Nanobiotechnology **6**(2).

Gao X, Cui Y, Levenson RM, et al. (2004). "In vivo cancer targeting and imaging with semiconductor quantum dots." Nature Biotechnology **22**(8): 969-976.

Gilchrist RK, Medal R, Shorey WD, et al. (1957). "Selective Inductive Heating of Lymph Nodes." Annals of Surgery **146**(4): 596-606.

Gladson CL, Prayson RA and Liu WM (2010). "The Pathobiology of Glioma Tumors." Annual Review of Pathology: Mechanisms of Disease **5**(1): 33-50.

Gobin AM, Lee MH, Halas NJ, et al. (2007). "Near-infrared resonant nanoshells for combined optical imaging and photothermal cancer therapy." Nano Letters **7**(7): 1929-1934.

Gobin AM, Moon JJ and West JL (2008). "EphrinA I-targeted nanoshells for photothermal ablation of prostate cancer cells." Int J Nanomedicine **3**(3): 351-358.

Gobin AM, Watkins EM, Quevedo E, et al. (2010). "Near-Infrared-Resonant Gold/Gold Sulfide Nanoparticles as a Photothermal Cancer Therapeutic Agent." Small **6**(6): 745-752.

Goodman LS, Wintrobe MM, Dameshek W, et al. (1946). "Nitrogen Mustard Therapy: Use of Methyl-Bis(Beta-Chloroethyl)amine Hydrochloride and Tris(Beta-Chloroethyl)amine Hydrochloride for Hodgkin's Disease, Lymphosarcoma, Leukemia and Certain Allied and Miscellaneous Disorders." JAMA **132**: 126-132.

Hadjipanayis CG, Machaidze R, Kaluzova M, et al. (2010). "EGFRvIII Antibody-Conjugated Iron Oxide Nanoparticles for Magnetic Resonance Imaging-Guided Convection-Enhanced Delivery and Targeted Therapy of Glioblastoma." Cancer Research **70**(15): 6303-6312.

Hanahan D and Weinberg RA (2000). "The Hallmarks of Cancer." Cell **100**(1): 57-70.

Hashizume H, Baluk P, Morikawa S, et al. (2000). "Openings between Defective Endothelial Cells Explain Tumor Vessel Leakiness." American Journal of Pathology **156**(4): 1363-1380.

Hatakeyama H, Akita H, Kogure K, et al. (2007). "Development of a novel systemic gene delivery system for cancer therapy with a tumor-specific cleavable PEG-lipid." Gene Therapy **14**: 68-77.

Hirsch LR, Gobin AM, Lowery AR, et al. (2006). "Metal nanoshells." Ann Biomed Eng **34**(1): 15-22.

Hirsch LR, Stafford RJ, Bankson JA, et al. (2003). "Nanoshell-mediated near-infrared thermal therapy of tumors under magnetic resonance guidance." Proc Natl Acad Sci USA **100**(23): 13549-13554.

Hoy CL, Durr NJ, Chen P, et al. (2008). "Miniaturized probe for femtosecond laser microsurgery and two-photon imaging." Opt. Express **16**(13): 9996-10005.

Huang X, Peng X, Wang Y, et al. (2010). "A Reexamination of Active and Passive Tumor Targeting by Using Rod-Shaped Gold Nanocrystals and Covalently Conjugated Peptide Ligands." ACS Nano **4**(10): 5887-5896.

Huang XL, Zhang B, Ren L, et al. (2008). "In vivo toxic studies and biodistribution of near infrared sensitive Au-Au2S nanoparticles as potential drug delivery carriers." Journal of Materials Science-Materials in Medicine **19**(7): 2581-2588.

Huff TB, Tong L, Zhao Y, et al. (2007). "Hyperthermic effects of gold nanorods on tumor cells." Nanomedicine (Lond) **2**(1): 125-132.

Hung M-C, Matin A, Zhang Y, et al. (1995). "HER-2/neu-targeting gene therapy-a review." Gene **159**(1): 65-71.

Huynh NT, Roger E, Lautram N, et al. (2010). "The rise and rise of stealth nanocarriers for cancer therapy: passive versus active targeting." Nanomedicine **5**(9): 1415-1433.

Imura K, Nagahara T and Okamoto H (2005). "Near-field two-photon-induced photoluminescence from single gold nanorods and imaging of plasmon modes." Journal of Physical Chemistry B **109**(27): 13214-13220.

Jain KK (2010). Potential of Nanobiotechnology in the Management of Glioblastoma Multiforme. Glioblastoma. SK Ray, Springer New York**:** 399-419.

Jain RK (2005). "Normalization of Tumor Vasculature: An Emerging Concept in Antiangiogenic Therapy." Science **307**(5706): 58-62.

James WD, Hirsch LR, West JL, et al. (2007). "Application of INAA to the build-up and clearance of gold nanoshells in clinical studies in mice." Journal of Radioanalytical and Nuclear Chemistry **271**(2): 455-459.

Janib SM, Moses AS and MacKay JA (2010). "Imaging and drug delivery using theranostic nanoparticles." Advanced Drug Delivery Reviews **62**(11): 1052-1063.

Jeanmaire DL and Van Duyne RP (1977). "Surface raman spectroelectrochemistry: Part I. Heterocyclic, aromatic, and aliphatic amines adsorbed on the anodized silver

electrode." Journal of Electroanalytical Chemistry and Interfacial Electrochemistry **84**(1): 1-20.

Johannsen M, Gneveckow U, Eckelt L, et al. (2005). "Clinical hyperthermia of prostate cancer using magnetic nanoparticles: Presentation of a new interstitial technique." International Journal of Hyperthermia **21**(7): 637-647.

Johannsen M, Gneveckow U, Thiesen B, et al. (2007). "Thermotherapy of Prostate Cancer Using Magnetic Nanoparticles: Feasibility, Imaging, and Three-Dimensional Temperature Distribution." European Urology **52**(6): 1653-1662.

Jordan A, Scholz R, Maier-Hauff K, et al. (2006). "The effect of thermotherapy using magnetic nanoparticles on rat malignant glioma." Journal of Neuro-Oncology **78**(1): 7-14.

Joshi BH, Plautz GE and Puri RK (2000). "Interleukin-13 Receptor α Chain: A Novel Tumor-associated Transmembrane Protein in Primary Explants of Human Malignant Gliomas." Cancer Research **60**(5): 1168-1172.

Jung WY, Tang S, McCormic DT, et al. (2008). "Miniaturized probe based on a microelectromechanical system mirror for multiphoton microscopy." Optics Letters **33**(12): 1324-1326.

Kawakami M, Kawakami K, Takahashi S, et al. (2004). "Analysis of interleukin-13 receptor α2 expression in human pediatric brain tumors." Cancer **101**(5): 1036-1042.

Kelloff GJ, Hoffman JM, Johnson B, et al. (2005). "Progress and Promise of FDG-PET Imaging for Cancer Patient Management and Oncologic Drug Development." Clinical Cancer Research **11**(8): 2785-2808.

Kennedy LC, Bickford LR, Lewinski NA, et al. (2010). "A New Era for Cancer Treatment: Gold-Nanoparticle-Mediated Thermal Therapies." Small: n/a-n/a.

Keren S, Zavaleta C, Cheng Z, et al. (2008). "Noninvasive molecular imaging of small living subjects using Raman spectroscopy." Proceedings of the National Academy of Sciences **105**(15): 5844-5849.

Keunen O, Johansson M, Oudin AØ, et al. (2011). "Anti-VEGF treatment reduces blood supply and increases tumor cell invasion in glioblastoma." Proceedings of the National Academy of Sciences **108**(9): 3749-3754.

Kirpotin DB, Drummond DC, Shao Y, et al. (2006). "Antibody Targeting of Long-Circulating Lipidic Nanoparticles Does Not Increase Tumor Localization but Does Increase Internalization in Animal Models." Cancer Research **66**(13): 6732-6740.

Knizetova P, Ehrmann J, Hlobilkova A, et al. (2008). "Autocrine regulation of glioblastoma cell cycle progression, viability and radioresistance through VEGF-VEGFR2 (KDR) interplay." Cell Cycle **7**(16): 2553-2561.

Kogelnik HD (1997). "Inauguration of radiotherapy as a new scientific specialty by Leopold Freund 100 years ago." Radiotherapy and Oncology **42**: 203-211.

Kraus MH, Popescu NC, Amsbaugh SC, et al. (1987). "Overexpression of the EGF Receptor-Related Proto-Oncogene erbB-2 in Human Mammary Tumor Cell Lines by Different Molecular Mechanisms." Embo Journal **6**(3): 605-610.

Kumar M, Yigit M, Dai G, et al. (2010). "Image-Guided Breast Tumor Therapy Using a Small Interfering RNA Nanodrug." Cancer Research **70**(19): 7553-7561.

Kunkel P, Ulbricht U, Bohlen P, et al. (2001). "Inhibition of Glioma Angiogenesis and Growth in Vivo by Systemic Treatment with a Monoclonal Antibody against Vascular Endothelial Growth Factor Receptor-2." Cancer Research **61**(18): 6624-6628.

Kunz C, Borghouts C, Buerger C, et al. (2006). "Peptide Aptamers with Binding Specificity for the Intracellular Domain of the ErbB2 Receptor Interfere with AKT Signaling and Sensitize Breast Cancer Cells to Taxol." Molecular Cancer Research **4**(12): 983-998.

Lamszus K, Brockmann MA, Eckerich C, et al. (2005). "Inhibition of Glioblastoma Angiogenesis and Invasion by Combined Treatments Directed Against Vascular Endothelial Growth Factor Receptor-2, Epidermal Growth Factor Receptor, and Vascular Endothelial-Cadherin." Clinical Cancer Research **11**(13): 4934-4940.

Lee H-Y, Li Z, Chen K, et al. (2008). "PET/MRI Dual-Modality Tumor Imaging Using Arginine-Glycine-Aspartic (RGD)-Conjugated Radiolabeled Iron Oxide Nanoparticles." The Journal of Nuclear Medicine **49**(8): 1371-1379.

Lewis GD, Figari I, Fendly B, et al. (1993). "Differential responses of human tumor cell lines to anti-p185^{HER2} monoclonal antibodies." Cancer Immunology, Immunotherapy **37**(4): 255-263.

Li ML, Wang JC, Schwartz JA, et al. (2009). "In-vivo photoacoustic microscopy of nanoshell extravasation from solid tumor vasculature." Journal of Biomedical Optics **14**(1): 3.

Liebner S, Fischmann A, Rascher G, et al. (2000). "Claudin-1 and claudin-5 expression and tight junction morphology are altered in blood vessels of human glioblastoma multiforme." Acta Neuropathologica **100**(3): 323-331.

Liu H-L, Hua M-Y, Yang H-W, et al. (2010). "Magnetic resonance monitoring of focused ultrasound/magnetic nanoparticle targeting delivery of therapeutic agents to the brain." Proceedings of the National Academy of Sciences **107**(34): 15205-15210.

Liu S-Y, Liang Z-S, Gao F, et al. (2010). "In vitro photothermal study of gold nanoshells functionalized with small targeting peptides to liver cancer cells." Journal of Materials Science-Materials in Medicine **21**: 665-674.

Long D (1970). "Capillary ultrastructure and the blood-brain barrier in human malignant brain tumors." J Neurosurg **32**(2): 127-144.

Loo C, Hirsch L, Lee MH, et al. (2005). "Gold nanoshell bioconjugates for molecular imaging in living cells." Opt Letters **30**(9): 1012-1014.

Loo C, Lowery A, Halas N, et al. (2005). "Immunotargeted nanoshells for integrated cancer imaging and therapy." Nano Letters **5**(4): 709-711.

Lowery AR, Gobin AM, Day ES, et al. (2006). "Immunonanoshells for targeted photothermal ablation of tumor cells." Int J Nanomedicine **1**(2): 149-154.

Lu W, Huang Q, Ku G, et al. (2010). "Photoacoustic imaging of living mouse brain vasculature using hollow gold nanospheres." Biomaterials **31**(9): 2617-2626.

Lu W, Xiong C, Zhang G, et al. (2009). "Targeted Photothermal Ablation of Murine Melanomas with Melanocyte-Stimulating Hormone Analog-Conjugated Hollow Gold Nanospheres." Clinical Cancer Research **15**(3): 876-886.

Lukianova-Hleb EY, Hanna EY, Hafner JH, et al. (2010). "Tunable plasmonic nanobubbles for cell theranostics." Nanotechnology **21**(8): 085102.

Lukianova-Hleb EY, Santiago C, Wagner DS, et al. (2010). "Generation and detection of plasmonic nanobubbles in zebrafish." Nanotechnology **21**(22): 225102.

Madhankumar AB, Slagle-Webb B, Mintz A, et al. (2006). "Interleukin-13 receptor–targeted nanovesicles are a potential therapy for glioblastoma multiforme." Molecular Cancer Therapeutics **5**(12): 3162-3169.

Maier-Hauff K, Rothe R, Scholz R, et al. (2007). "Intracranial thermotherapy using magnetic nanoparticles combined with external beam radiotherapy: Results of a feasibility study on patients with glioblastoma multiforme." Journal of Neuro-Oncology **81**(1): 53-60.

Maier-Hauff K, Ulrich F, Nestler D, et al. (2010). "Efficacy and safety of intratumoral thermotherapy using magnetic iron-oxide nanoparticles combined with external beam radiotherapy on patients with recurrent glioblastoma multiforme." Journal of Neuro-Oncology: 1-8.

Marth C, Lang T, Cronauer MV, et al. (1992). "Epidermal growth factor reduces HER-2 protein level in human ovarian carcinoma cells." International Journal of Cancer **52**(2): 311-316.

Mathers CD and Loncar D (2006). "Projections of Global Mortality and Burden of Disease from 2002 to 2030." PLoS Medicine **3**(11): 2011-2030.

Matsumura Y and Maeda H (1986). "A New Concept for Macromolecular Therapeutics in Cancer Chemotherapy: Mechanism of Tumoritropic Accumulation of Proteins and the Antitumor Agent Smancs." Cancer Research **46**(12 Part 1): 6387-6392.

McKinnell RG, RParchment RE, Perantoni AO, et al. (1998). The Biological Basis of Cancer. New York, Cambridge University Press.

Medarova Z, Pham W, Farrar C, et al. (2007). "In vivo imaging of siRNA delivery and silencing in tumors." Nature Medicine **13**(3): 372-377.

Menard S, Pupa SM, Campiglio M, et al. (2003). "Biologic and therapeutic role of HER2 in cancer." Oncogene **22**(42): 6570-6578.

Michalet X, Pinaud FF, Bentolila LA, et al. (2005). "Quantum Dots for Live Cells, in Vivo Imaging, and Diagnostics." Science **307**(5709): 538-544.

Miletic H, Niclou SP, Johansson M, et al. (2009). "Anti-VEGF therapies for malignant glioma: treatment effects and escape mechanisms." Expert Opinion on Therapeutic Targets **13**(4): 455-468.

Minchin RF and Martin DJ (2010). "Minireview: Nanoparticles for Molecular Imaging--An Overview." Endocrinology **151**(2): 474-481.

Moon HK, Lee SH and Choi HC (2009). "In Vivo Near-Infrared Mediated Tumor Destruction by Photothermal Effect of Carbon Nanotubes." ACS Nano **3**(11): 3707-3713.

Morton JG, Day ES, Halas NJ, et al. (2010). Nanoshells for Photothermal Cancer Therapy. Cancer Nanotechnology: Methods and Protocols. SR Grobmyer and BM Moudgil. New York, Humana Press: 101-117.

Murphy EA, Majeti BK, Barnes LA, et al. (2008). "Nanoparticle-mediated drug delivery to tumor vasculature suppresses metastasis." Proceedings of the National Academy of Sciences **105**(27): 9343-9348.

Nasongkla N, Bey E, Ren J, et al. (2006). "Multifunctional Polymeric Micelles as Cancer-Targeted, MRI-Ultrasensitive Drug Delivery Systems." Nano Letters **6**(11): 2427-2430.

National Cancer Institute (2010). SEER Cancer Statistics Review, 1975-2007. Bethesda, MD.

Needham D, Anyarambhatla G, Kong G, et al. (2000). "A New Temperature-sensitive Liposome for Use with Mild Hyperthermia: Characterization and Testing in a Human Tumor Xenograft Model." Cancer Research **60**(5): 1197-1201.

Neuwelt EA, Várallyay P, Bagó AG, et al. (2004). "Imaging of iron oxide nanoparticles by MR and light microscopy in patients with malignant brain tumours." Neuropathology and Applied Neurobiology **30**(5): 456-471.

Niidome T, Yamagata M, Okamoto Y, et al. (2006). "PEG-modified gold nanorods with a stealth character for in vivo applications." J Control Release **114**(3): 343-347.

Norman TJ, Grant CD, Magana D, et al. (2002). "Near infrared optical absorption of gold nanoparticle aggregates." Journal of Physical Chemistry B **106**(28): 7005-7012.

O'Neal DP, Hirsch LR, Halas NJ, et al. (2004). "Photo-thermal tumor ablation in mice using near infrared-absorbing nanoparticles." Cancer Letters **209**(2): 171-176.

Oldenburg SJ, Averitt RD, Westcott SL, et al. (1998). "Nanoengineering of optical resonances." Chemical Physics Letters **288**(2-4): 243-247.

Paget S (1889). "The Distribution of Secondary Growths in Cancer of the Breast." Lancet **1**: 571-573.

Park H, Yang J, Lee J, et al. (2009). "Multifunctional Nanoparticles for Combined Doxorubicin and Photothermal Treatments." ACS Nano **3**(10): 2919-2926.

Park J, Estrada A, Sharp K, et al. (2008). "Two-photon-induced photoluminescence imaging of tumors using near-infrared excited gold nanoshells." Optics Express **16**(3): 1590-1599.

Park JH, von Maltzahn G, Xu MJ, et al. (2010). "Cooperative nanomaterial system to sensitize, target, and treat tumors." Proceedings of the National Academy of Sciences of the United States of America **107**(3): 981-986.

Park JW, Hong K, Kirpotin DB, et al. (2002). "Anti-HER2 Immunoliposomes." Clinical Cancer Research **8**(4): 1172-1181.

Peer D, Karp JM, Hong S, et al. (2007). "Nanocarriers as an emerging platform for cancer therapy." Nature Nanotechnology **2**(12): 751-760.

Peles E, Ben-Levy R, Tzahar E, et al. (1993). "Cell-type specific interaction of Neu differentiation factor (NDF/heregulin) with Neu/HER-2 suggests complex ligand-receptor relationships." The EMBO Journal **12**(3): 961-971.

Perrault SD, Walkey C, Jennings T, et al. (2009). "Mediating Tumor Targeting Efficiency of Nanoparticles Through Design." Nano Letters **9**(5): 1909-1915.

Piyawattanametha W, Cocker ED, Burns LD, et al. (2009). "In vivo brain imaging using a portable 2.9 g two-photon microscope based on a microelectromechanical systems scanning mirror." Optics Letters **34**(15): 2309-2311.

Plate KH, Breier G, Weich HA, et al. (1994). "Vascular Endothelial Growth Factor and Glioma Angiogenesis: Coordinate Induction of VEGF Receptors, Distribution of VEGF Protein and Possible *In Vivo* Regulatory Mechanisms." Int J Cancer **59**: 520-529.

Pollock RE (2008). Surgical Oncology in Multimodality Cancer Care: History and Scope. Advanced Therapy in Surgical Oncology. RE Pollock, SA Curley, MI Ross and NE Perrier. Hamilton, Ontario, BC Decker, Inc.

Qian X, Peng X-H, Ansari DO, et al. (2008). "In vivo tumor targeting and spectroscopic detection with surface-enhanced Raman nanoparticle tags." Nat Biotechnol **26**(1): 83-90.

Raschke G, Brogl S, Susha AS, et al. (2004). "Gold Nanoshells Improve Single Nanoparticle Molecular Sensors." Nano Letters **4**(10): 1853-1857.

Raschke G, Brogl S, Susha AS, et al. (2005). "Reply to "Comment on 'Gold Nanoshells Improve Single Nanoparticle Molecular Sensors'"." Nano Letters **5**(4): 811-812.

Reardon DA, Wen PY, Desjardins A, et al. (2008). "Glioblastoma multiforme: an emerging paradigm of anti-VEGF therapy." Expert Opinion on Biological Therapy **8**(4): 541-553.

Reddy GR, Bhojani MS, McConville P, et al. (2006). "Vascular targeted nanoparticles for imaging and treatment of brain tumors." Clinical Cancer Research **12**(22): 6677-6686.

Ren L, Huang XL, Zhang B, et al. (2008). "Cisplatin-loaded Au-Au2S noparticles for potential cancer therapy: Cytotoxicity, in vitro carcinogenicity, and cellular uptake." Journal of Biomedical Materials Research Part A **85A**(3): 787-796.

Rhyner MN, Smith AM, Gao X, et al. (2006). "Quantum dots and multifunctional nanoparticles: new contrast agents for tumor imaging." Nanomedicine **1**(2): 209-217.

Ricard D, Taillia H and Renard JL (2009). "Brain damage from anticancer treatments in adults." Current Opinion in Oncology **21**(6): 559-565.

Rini BI and Small EJ (2005). "Biology and Clinical Development of Vascular Endothelial Growth Factor – Targeted Therapy in Renal Cell Carcinoma." Journal of Clinical Oncology **23**(5): 1028-1043.

Ron E (2003). "Cancer Risks from Medical Radiation." Health Physics **85**(1): 47-59.

Rundhaug JE (2003). "Matrix Metalloproteinases, Angiogenesis, and Cancer." Clinical Cancer Research **9**: 551-554.

Ruoslahti E, Bhatia SN and Sailor MJ (2010). "Targeting of drugs and nanoparticles to tumors." Journal of Cell Biology **188**(6): 759-768.

Schneider S, Ludwig T, Tatenhorst L, et al. (2004). "Glioblastoma cells release factors that disrupt blood-brain barrier features." Acta Neuropathologica **107**(3): 272-276.

Schwartz JA, Shetty AM, Price RE, et al. (2009). "Feasibility Study of Particle-Assisted Laser Ablation of Brain Tumors in Orthotopic Canine Model." Cancer Research **69**(4): 1659-1667.

Schwartzberg AM, Grant CD, van Buuren T, et al. (2007). "Reduction of HAuCl4 by Na2S revisited: The case for Au nanoparticle aggregates and against Au2S/Au Core/Shell particles." Journal of Physical Chemistry C **111**(25): 8892-8901.

Sershen SR, Westcott SL, Halas NJ, et al. (2000). "Temperature-sensitive polymer-nanoshell composites for photothermally modulated drug delivery." J Biomed Mater Res **51**(3): 293-298.

Slamon DJ, Clark GM, Wong SG, et al. (1987). "Human Breast Cancer: Correlation of Relapse and Survival with Amplification of the HER-2/neu Oncogene." Science **235**(4785): 177-182.

Smith-Bindman R, Lipson J, Marcus R, et al. (2009). "Radiation Dose Associated With Common Computed Tomography Examinations and the Associated Lifetime Attributable Risk of Cancer." Archives of Internal Medicine **169**(22): 2078-2086.

Soeller C and Cannell MB (1999). "Two-photon microscopy: imaging in scattering samples and three-dimensionally resolved flash photolysis." Microscopy research and technique **47**(3).

Sonavane G, Tomoda K and Makino K (2008). "Biodistribution of colloidal gold nanoparticles after intravenous administration: Effect of particle size." Colloids and Surfaces B: Biointerfaces **66**(2): 274-280.

Song KH, Kim CH, Cobley CM, et al. (2009). "Near-Infrared Gold Nanocages as a New Class of Tracers for Photoacoustic Sentinel Lymph Node Mapping on a Rat Model." Nano Letters **9**(1): 183-188.

Stefanik DF, Fellows WK, Rizkalla LR, et al. (2001). "Monoclonal Antibodies to Vascular Endothelial Growth Factor (VEGF) And the VEGF Receptor, FLT-1, Inhibit the Growth of C6 Glioma in a Mouse Xenograft." Journal of Neuro-Oncology **55**(2): 91-100.

Stern JM, Stanfield J, Lotan Y, et al. (2007). "Efficacy of Laser-Activated Gold Nanoshells in Ablating Prostate Cancer Cells *in Vitro*." Journal of Endourology **21**(8): 939-943.

Stöber W, Fink A and Bohn E (1968). "Controlled growth of monodisperse silica spheres in the micron size range." Journal of Colloid and Interface Science **26**: 62-69.

Stupp R, Mason WP, van den Bent MJ, et al. (2005). "Radiotherapy plus concomitant and adjuvant temozolomide for glioblastoma." New England Journal of Medicine **352**(10): 987-996.

Sugahara KN, Teesalu T, Karmali PP, et al. (2009). "Tissue-Penetrating Delivery of Compounds and Nanoparticles into Tumors." Cancer Cell **16**(6): 510-520.

Tan M, Ying J and Chow G (2009). "Interfacial properties and in vitro cytotoxic effects of surface-modified near infrared absorbing Au-Au_2S nanoparticles." Journal of Materials Science: Materials in Medicine **20**(10): 2091-2103.

Tuettenberg J, Friedel C and Vajkoczy P (2006). "Angiogenesis in malignant glioma--A target for antitumor therapy?" Critical Reviews in Oncology/Hematology **59**(3): 181-193.

van Vlerken LE, Vyas TK and Amiji MM (2007). "Poly(ethylene glycol)-modified Nanocarriers for Tumor-targeted and Intracellular Delivery." Pharmaceutical Research **24**: 1405-1414.

Wang H, Huff TB, Zweifel DA, et al. (2005). "In vitro and in vivo two-photon luminescence imaging of single gold nanorods." Proc Natl Acad Sci USA **102**(44): 15752-15756.

Wang M and Thanou M (2010). "Targeting nanoparticles to cancer." Pharmacological Research **62**(2): 90-99.

Wang YW, Xie XY, Wang XD, et al. (2004). "Photoacoustic tomography of a nanoshell contrast agent in the in vivo rat brain." Nano Letters **4**(9): 1689-1692.

Wei Q, Ji J and Shen J (2008). "Synthesis of Near-Infrared Responsive Gold Nanorod/PNIPAAm Core/Shell Nanohybrids via Surface Initiated ATRP for Smart Drug Delivery." Macromolecular Rapid Communications **29**(8): 645-650.

Weissleder R (2001). "A clearer vision for in vivo imaging." Nat Biotechnol **19**(4): 316-317.

Weissleder R (2006). "Molecular Imaging in Cancer." Science **312**(5777): 1168-1171.

Weller M and Wick W (2010). "'"Nanomania" *ante portas* of neurooncology?" Journal of Neuro-Oncology: 1-2.

Wen PY and Kesari S (2008). "Malignant gliomas in adults." New England Journal of Medicine **359**(5): 492-507.

Wust P, Hildebrandt B, Sreenivasa G, et al. (2002). "Hyperthermia in combined treatment of cancer." The Lancet Oncology **3**(8): 487-497.

Xie H, Gill-Sharp KL and O'Neal DP (2007). "Quantitative estimation of gold nanoshell concentrations in whole blood using dynamic light scattering." Nanomedicine **3**(1): 89-94.

Xie J, Lee S and Chen X (2010). "Nanoparticle-based theranostic agents." Advanced Drug Delivery Reviews **62**(11): 1064-1079.

Xu Y, Mahmood MW, Fejleh A, et al. (2010). "Carbon-covered magnetic nanomaterials and their application for the thermolysis of cancer cells." Int J Nanomedicine **5**(167-176).

Yang T, Choi M-K, Cui F-D, et al. (2007). "Antitumor Effect of Paclitaxel-Loaded PEGylated Immunoliposomes Against Human Breast Cancer Cells." Pharmaceutical Research **24**(12): 2402-2411.

Yang X, Grailer JJ, Rowland IJ, et al. (2010). "Multifunctional Stable and pH-Responsive Polymer Vesicles Formed by Heterofunctional Triblock Copolymer for Targeted Anticancer Drug Delivery and Ultrasensitive MR Imaging." ACS Nano: null-null.

Yatvin MB, Weinstein JT, Dennis WH, et al. (1978). "Design of Liposomes for Enhanced Local Release of Drugs by Hyperthermia." Science **202**(4374): 1290-1293.

Yi D, Hua T, Lin H, et al. (2010). "Antitumor treatment efficacy by targeting epidermal growth factor receptor and vascular endothelial growth factor receptor-2 in an orthotopic human glioblastoma model." Journal of Neuro-Oncology: 1-9.

You J, Zhang G and Li C (2010). "Exceptionally High Payload of Doxorubicin in Hollow Gold Nanospheres for Near-Infrared Light-Triggered Drug Release." ACS Nano **4**(2): 1033-1041.

Yu D, Wolf JK, Scanlon M, et al. (1993). "Enhanced c-erbB-2/neu Expression in Human Ovarian Cancer Cells Correlates with More Severe Malignancy That Can Be Suppressed by E1A." Cancer Research **53**(4): 891-898.

Yuan Z and Jiang H (2010). Photoacoustic Tomography for Imaging Nanoparticles. Cancer Nanotechnology: Methods and Protocols. SR Grobmyer and BM Moudgil. New York, Humana Press**:** 309-324.

Zavaleta CL, Smith BR, Walton I, et al. "Multiplexed imaging of surface enhanced Raman scattering nanotags in living mice using noninvasive Raman spectroscopy." Proceedings of the National Academy of Sciences.

Zhang GD, Yang Z, Lu W, et al. (2009). "Influence of anchoring ligands and particle size on the colloidal stability and in vivo biodistribution of polyethylene glycol-coated gold nanoparticles in tumor-xenografted mice." Biomaterials **30**(10): 1928-1936.

Zhang J, Sun H and Ma PX (2010). "Host-Guest Interaction Mediated Polymeric Assemblies: Multifunctional Nanoparticles for Drug and Gene Delivery." ACS Nano **4**(2): 1049-1059.

Zhang JZ, Schwartzberg AM, Norman T, et al. (2005). "Comment on "Gold Nanoshells Improve Single Nanoparticle Molecular Sensors"." Nano Letters **5**(4): 809-810.

Zhou G and Roizman B (2006). "Construction and properties of a herpes simplex virus 1 designed to enter cells solely via the IL-13alpha2 receptor." Proc Natl Acad Sci U S A **103**: 5508-5513.

Zhou HS, Honma I, Komiyama H, et al. (1994). "Controlled Synthesis and Quantum-Size Effect in Gold-Coated Nanoparticles." Physical Review B **50**(16): 12052-12056.

Zhu X, Wu S, Dahut WL, et al. (2007). "Risks of Proteinuria and Hypertension With Bevacizumab, an Antibody Against Vascular Endothelial Growth Factor: Systematic Review and Meta-Analysis." American Journal of Kidney Diseases **49**(2): 186-193.

Zipfel WR, Williams RM and Webb WW (2003). "Nonlinear magic: multiphoton microscopy in the biosciences." Nature Biotechnology **21**(11): 1369-1377.